Design and simulation of a short, 10 MV, variable energy linear accelerator for use in linac-MR systems

by

Devin Micheal James Baillie

A thesis submitted in partial fulfillment of the requirements for the degree of

Doctor of Philosophy

in

Medical Physics

Department of Oncology
University of Alberta

Abstract

Hybrid linac-MR devices are currently being designed and constructed by several groups around the world which combine a linear accelerator with an MRI in order to enable real-time 3D imaging to visualize tumor movement during external beam radiotherapy treatments. Each of the current systems is limited to a single x-ray energy (6 MV or 8 MV) for treatments which can result in suboptimal treatments for many patients. In conventional radiotherapy, a variety of energies are used to achieve optimal treatments. Larger patients with deeper tumors can be better treated with higher energy x-rays, while superficial tumors or those located near an air cavity can benefit from lower energy x-rays. Current multi-energy medical linacs are too long to be incorporated into linac-MR systems. In order to enable linac-MR systems to treat every patient optimally, this research aimed to design a new linear accelerator capable of producing a variety of energies from 4 to 10 MV that short enough to be compatible with the Alberta linac-MR system, which currently uses a 27.5 cm long Varian 600C (6 MV) linear accelerator.

A previously designed finite element model (FEM) of the Varian 600C linear accelerator was used to investigate the feasibility of designing a linear accelerator the same length as the current 6 MV accelerator, but capable of producing 10 MV. The input power to the FEM model was increased, and the resulting electron and photon beams were simulated using particle-in-cell (PIC) and Monte Carlo (MC) methods, respectively. It was shown that, with some modification to the waveguide, a 10 MV x-ray beam can be produced without risk of electric breakdown within the waveguide.

A new, short linear accelerator was then designed capable of producing a 10 MV x-ray beam. This was accomplished by first designing a single accelerator cavity based on published electric breakdown experiments, and using this as a basis for a full accelerator structure. The cavity dimensions were matched to the breakdown study using a stochastic approach and FEM simulations. FEM simulations were also used to tune the full waveguide structure and calculate the RF fields within. PIC and MC simulations were again used to simulate the electron beam through the waveguide and the x-ray beam produced. The results of the MC simulations were then used to optimize the waveguide geometry until an x-ray beam matching the energy of currently used 10 MV linear accelerators was produced. Percent depth dose curves from the new linac's x-ray beam closely matched that produced by a Varian 10 MV linac, while the fields within the waveguide remained below the cavity-specific breakdown threshold.

The newly designed 10 MV accelerator was then modified to allow the x-ray energy to be reduced, in order to produce a variety of x-ray energies from a single accelerator. This was accomplished by the addition of a tuning cylinder to the first coupling cavity of the waveguide, allowing the power in the first cavity to be varied independently from the power in the remaining cavities. By reducing the input power, the electron energies were reduced, and by adjusting the position of the tuning cylinder the first cavity fields were optimized for electron capture. The input power and cylinder position were optimized to so that the new 10 MV linac would produce x-ray beams with energies of 4, 6, 8, and 10 MV, with the 4, 6, and 10 MV energies all beam-matched to Varian accelerators of the same energy. Final depth dose curves from the new variable-energy linac showed excellent agreement compared to Varian accelerators over all optimized energies (4, 6, and 10 MV).

Preface

Some of the research presented in this thesis was the result of a collaboration between myself and Dr. Joel St. Aubin. Dr. St. Aubin created the waveguide model used in Chapter 3, the electron gun model used in Chapters 3 and 4, and the script which converts the PARMELA output phase space into a BEAMnrc input phase space which was used in Chapters 3, 4, and 5. The remainder of the work in Chapters 3, 4, and 5 was completed by myself, including modifying the waveguide model produced by Dr. St. Aubin to increase the input power. The dose distributions presented in Figure 1.2 were produced by Dr. Steciw.

Chapters 3 and 4 have been published, and chapter 5 has been submitted for publication. I was responsible for the composition of the manuscripts with supervision and input from Dr. Steciw. Dr. St. Aubin contributed edits to the published versions of Chapters 3 and 4, and Dr. Fallone contributed edits to the published versions of Chapters 3, 4, and 5.

Acknowledgments

First and foremost, I would like to thank my supervisors, Dr. Gino Fallone and Dr. Stephen Steciw for their support throughout this project. In particular, I would like to express my sincere thanks to Dr. Steciw for the countless hours spent helping me figure out the issues with my code, making sure I had covered every possible issue, reviewing manuscripts and scholarship applications, and just talking when I was having a particularly rough day, week, or year. Dr. Steciw went above and beyond what was required, running around filling out paperwork if I was away and taking extra time on the weekends to respond to questions and review manuscripts. I couldn't have finished without his continued support and mentorship, and couldn't have asked for a better supervisor. I would like to thank Dr. Fallone for the support (both practical and financial) throughout the project, he often reviewed documents or filled out paperwork on short notice (for which I apologize, I often got so focused on working on my research that I forgot about paperwork and deadlines until the last minute).

There are many of my colleagues who deserve acknowledgment for contributions, both direct and indirect. Dr. Joël St. Aubin helped in setting up the initial simulations, and provided advice in the early stages of this project. Dan Doran helped by providing physical measurements and descriptions of many linac components. I'd like to thank Andrei Ghila, Jean-David Justras, and Amr Heikal for working out with me; it helped keep me sane through some rough times. Thanks to Eugene Yip, who provided countless hours of interesting discussion, which probably delayed both of our graduation by at least a few months. More recently, Hali Morrison, Brie Cawston-Grant, and Simon Ferguson encouraged me to take up climbing, which was good for both my physical and mental health. I'd also like to thank everyone else at the Cross Cancer Institute for providing a supportive and interesting work environment.

Finally, I'd like to thank my family for their support throughout this work. My wife, Beth, has been amazingly supportive. She went above and beyond anything I could have asked by providing me the time to write by taking on extra chores around the house and managing the children, all while eight and a half months pregnant. She did all of this, and helped with wordsmithing whenever I got stuck. My oldest son Cale, nine years old at the time of printing, keeps life interesting and entertaining as he always wants to tell me about the latest thing he's discovered. My middle son, Zachary, five years old at the time of printing, is always looking for me to play Lego or superheroes (or, more often, super-villains) with him. Their love and affection made everything else bearable, and were my motivation to continue. My newest son, Sebastian, born just after I sent this thesis out to my examining committee, I'd like to thank for waiting to be born until after I had finished writing. Last but not least, I'd like to thank my mother, Lorrie, for always believing in me and supporting me in everything I do, throughout my childhood and into adulthood as well.

Table of Contents

List of Tables

List of Figures

List of Abbreviations

3DCRT	3 Dimensional Conformal Radiation Therapy
CBCT	Cone-Beam Computed Tomography
CDF	Cumulative Distribution Function
CSDA	Continuously Slowing Down Approximation
CT	Computed Tomography
CTV	Clinical Target Volume
DC	Direct Current
DCS	Differential Cross Section
EM	Electromagnetic
EPID	Electronic Portal Imaging Device
FEM	Finite Element Method
FWHM	Full Width at Half Maximum
GTV	Gross Tumor Volume
IGRT	Image-Guided Radiation Therapy
IM	Internal Margin
IMRT	Intensity-Modulated Radiation Therapy
MLC	Multi-Leaf Collimator
MR(I)	Magnetic Resonance (Image/Imaging/Imager)
MVCT	Megavoltage Computed Tomography
PDD	Percent Depth Dose curve
PDF	Probability Density Function
PET	Positron Emission Tomography

PIC	Particle in Cell
PTV	Planning Target Volume
RF	Radiofrequency
RLC	Resistor Inductor Capacitor (L is the traditional symbol for an inductance)
RMS	Root Mean Square
SM	Setup Margin
SPECT	Single Photon Emission Computed Tomography
US	Ultrasound
VMAT	Volumetric Modulated Arc Therapy

1. Introduction

1.1 Current Methods in External Beam Radiotherapy

External beam radiotherapy involves treating cancer patients with beams of radiation in order to kill the cancer cells. Because the radiation affects healthy tissue as well as tumor, one of the main goals of radiotherapy is to irradiate as little normal tissue as possible with the lowest possible dose, while delivering the prescribed radiation dose to the target volume within the patient. There are several techniques used to accomplish this: selection of photon energy, accurate target definition, shaping and modulating the radiation beam, and using imaging techniques to guide radiotherapy treatments.

1.1.1 Photon Energies

Much of the history of radiation therapy has been a pursuit of higher photon energies for treatment. Initially, in the early 1900s, x-rays used for treatment were produced by Crookes tubes (Fig. 1.1a) and photon energies were restricted to a few hundreds of kilovolts. The x-rays produced by these devices were limited to treating superficial tumors like skin cancers or tumors just below the skin as they deposit most of their dose near the surface of the patient. In order to get sufficient dose to treat deeper tumors, massive doses must be deposited near the patient surface, causing radiation burns. In the 1930s, megavoltage accelerators like the betatron (Fig. 1.1b) and the linac (Fig. 1.1c) among others were developed for particle physics. Throughout the 1930s to the 1950s these technologies began to see use in medical applications. The 1950s also saw the production of cobalt-60, which emits megavoltage x-rays, from nuclear reactors developed during the second world war. Cobalt therapy machines (Fig. 1.1d) soon made up the majority of medical megavoltage x-ray devices, until the development of the modern medical linac in the 1970s. These devices produced megavoltage x-rays, which are much more penetrating and produced considerably lower skin doses than the earlier kilovoltage x-rays, allowing the treatment of tumors that were deeper within the patient. Currently, for megavoltage external-beam radiation therapy, a variety of energies are used, from about 2 to 22 MV, depending on the specific treatment case.

The optimal energy for treatment varies depending on the location of a patient's tumor. Therefore, a range of x-ray energies is required to optimally treat all patients. Photon energies above 6 MV are commonly used to treat deeper tumors, and tumors that require increased x-ray penetration. Deep tumors in larger patients, or breast tumors in large breasted patients, are frequently treated with 10 MV or higher (Fig. 1.2). Photon energies of 10 MV produce lower surface dose and a larger buildup region and a deeper depth of maximum dose compared to 6 MV, which can result in lower doses to healthy tissue near and at the surface of the patient for the same dose to a deeper tumor. Photon energies of 10 MV or higher have been shown to produce better dose distributions in many cases, and are currently used in 50% of cancer treatments at the Cross Cancer Institute. The use of modulated therapies (see section 1.1.3), such as IMRT and VMAT, are commonly thought to eliminate the benefits of using higher energies, however recent studies have concluded that there are still cases which benefit from the use of energies up to 10 MV (5). It has been suggested (6) that the use of energies beyond 10 MV should be avoided for modulated therapies, due to the presence of neutron contamination which contributes to whole body patient dose. In contrast, some tumors can benefit from

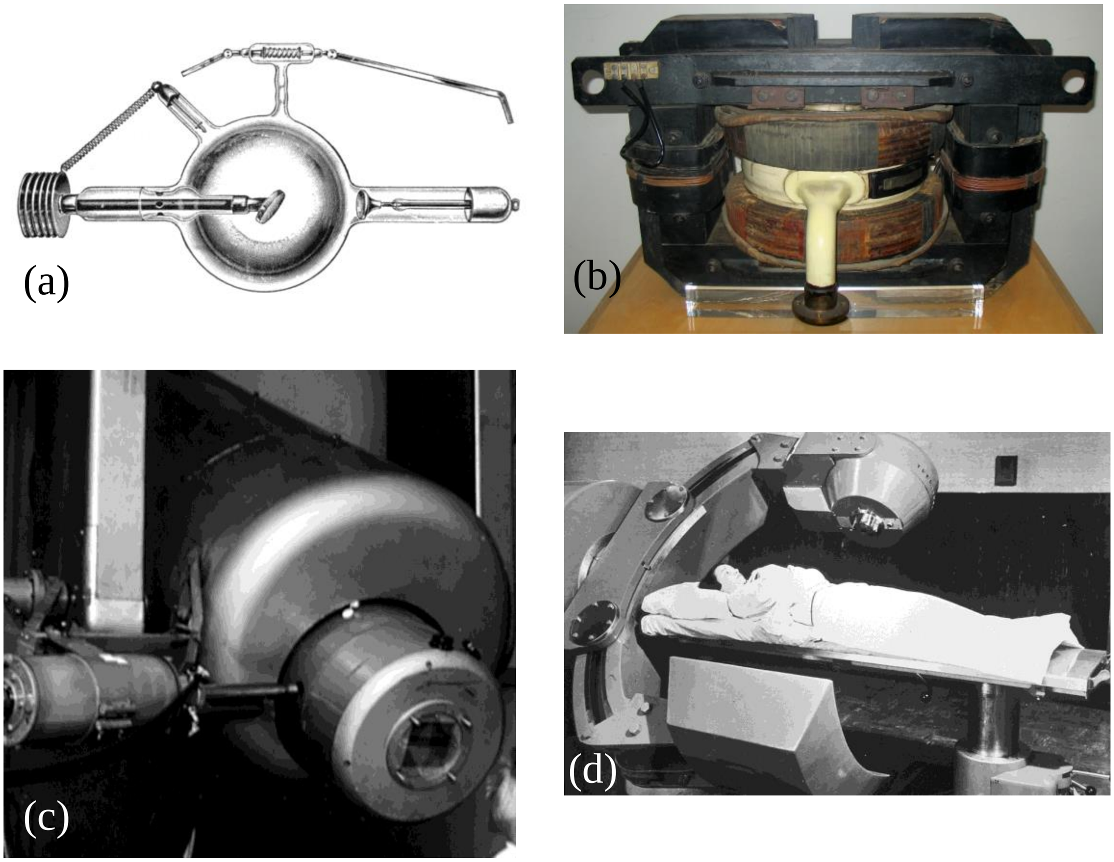

Figure 1.1: Some examples of early radiation devices: (a) Crookes tubes were first developed in the 1870s (1). They operate by applying a voltage (typically up to 100 kV) to a weak vacuum which, through a multi-step process) results in electrons being emitted from the cathode and accelerated to the anode. Crookes tubes were used by Röntgen in his 1895 discovery of x-rays (2) and soon after used for medical treatments (3). (b) The betatron was developed in 1935 by Max Steenbeck in Germany, and development continues in the United States under Donald Kerst. (4) These operate by accelerating electrons around a circular path using a changing magnetic field. (c) One of the earliest medical linear accelerators was used in the first linac-based retinoblastoma treatment. (d) A cobalt therapy machine from the 1950s. This device can rotate around the patient to treat from multiple angles, and has a lead shield to absorb the radiation which passes through the patient.

energies below 6 MV. Superficial tumors can benefit from lower energies, as they do not deposit as much dose beyond the distal end of the tumor. Additionally, photon energies of 10 or 6 MV produce a broader beam penumbra, and therefore tumors near a lower density region, such as lungs, sinuses, or esophagus can benefit from lower energies as

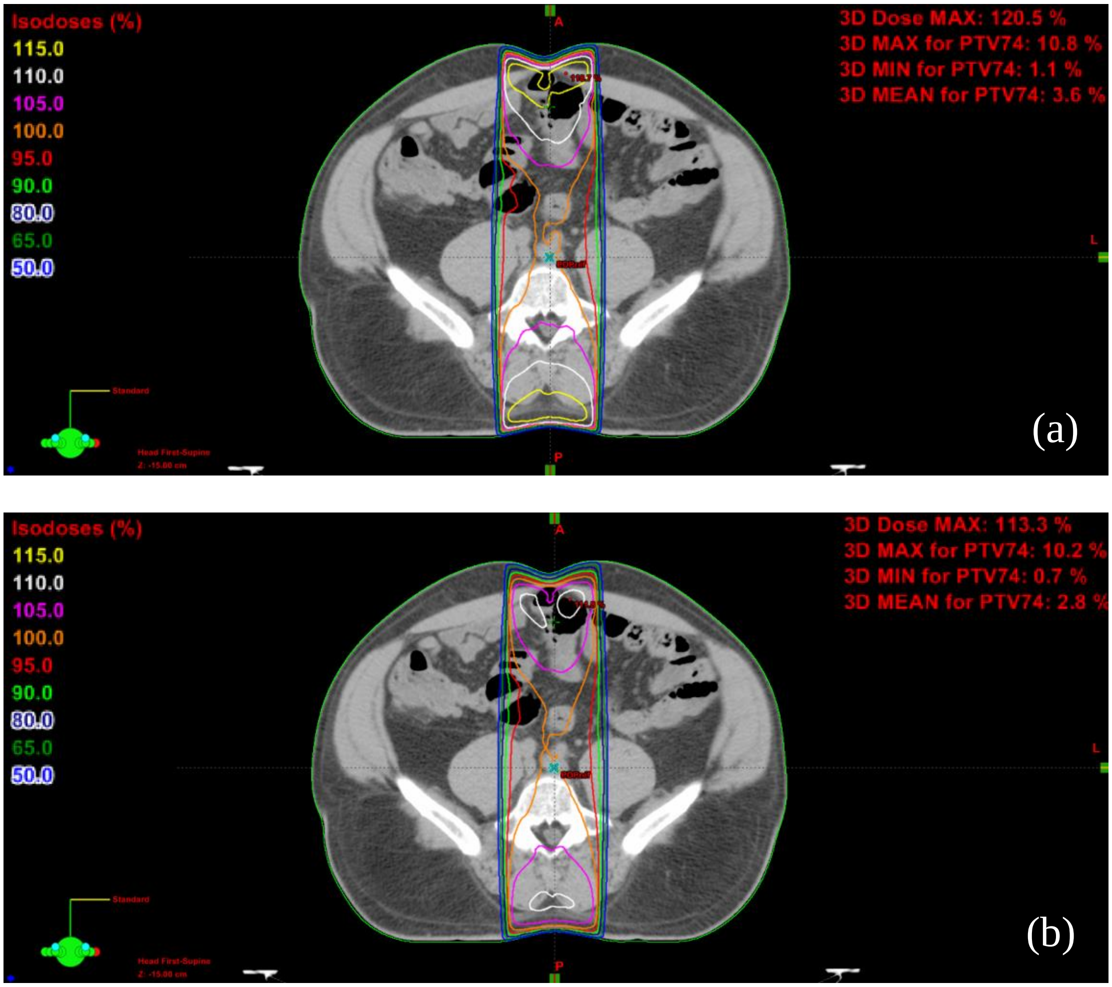

Figure 1.2: The 6 MV x-ray plan (a) produces hot spots of 120.5% of the prescription dose in healthy tissue in order to ensure coverage of the PTV, while the 10 MV x-ray plan (b) produces hot spots of only 113.3% in the same regions. Using 6 MV x-rays can result in having to balance underdosing the tumor and overdosing the healthy tissue. Because of the increased penetration, with 10 MV x-rays, this is less of an issue.

well (7), due to the decreased lateral range of secondary electrons produced by lower energy beams when compared to higher energy beams.

There are two main types of medical linear accelerators (linacs) in use today. Single energy accelerators typically produce a single, relatively low energy (2 – 8 MV), and are usually short, in length, less than 50 cm. Modern high-energy linacs are much longer, 1.5 m or more, and more complicated. The linac is oriented perpendicularly to the treatment direction, and the electron beam is redirected through a 270° bend before striking the x-ray target. The increased length of the linacs requires additional components as well, such as focusing and buncher coils, which are coils around the accelerator structure which produce a magnetic field to guide and shape the electron beam before and while it is accelerated through the linac. These high-energy linacs are capable of producing a variety of photon beam energies, typically a selection of energies between 4 and 22 MV. These multi-energy linacs allow both high and low energies to be used when necessary, allowing more optimum dose delivery and less dose to the healthy tissue in the path of the beam.

1.1.2 Margins

The aim of external beam radiotherapy is to deliver radiation to the tumor in order to kill the cancerous cells using beams of radiation that pass through the patient, focused on the tumor. This results in a large amount of healthy tissue being irradiated as well, partly because the radiation affects all the cells in its path, but also because a larger volume than just the tumor mass must be irradiated in order to ensure that all cancerous cells receive sufficient radiation dose (Fig. 1.3).

Frequently there is more to the tumor than is visible on any images or combination of images. Subclinical, microscopic extensions of the cancer may invade the healthy tissue surrounding the GTV, and this disease may be indistinguishable from non-cancerous tissue on any imaging modality. The oncologist uses their knowledge and clinical experience of cancer progression to determine into which tissues a tumor is likely to have spread, and adds a margin around the GTV to form the clinical target volume (CTV) (8,9). This margin varies depending on the patient and cancer, and is often

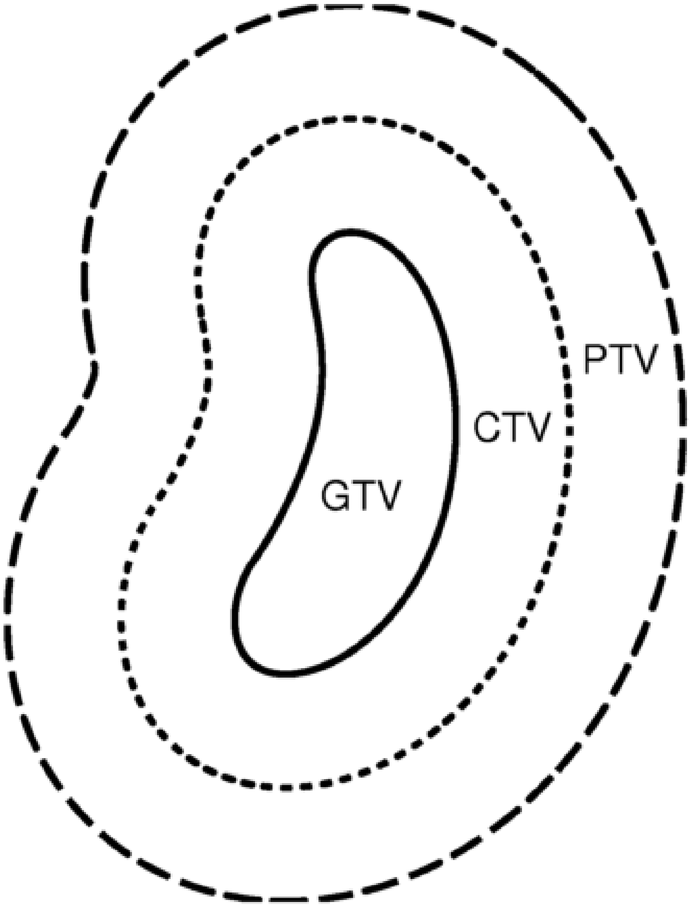

Figure 1.3: The margins added to the gross tumor volume to account for microscopic disease, motion, and setup error. The GTV contains the entire known volume of the tumor observable in patient images. The CTV contains the GTV, as well as any suspected subclinical disease. The PTV represents the region to be treated in order to ensure coverage of the CTV and accounts for patient, tumor, and organ movement as well as variations in the patient setup.

different in different directions within one patient. The CTV may also contain tissues distant from the GTV, such as lymph nodes, if the disease is suspected to have migrated. The CTV includes the entire known and suspected extent of the tumor.

In order to ensure radiation coverage of the CTV, a larger region must be irradiated. This is because the treatment is planned and the dose calculated on a single, static image, while in reality they patient and tumor are rarely static during treatment delivery. Tumors frequently move within a patient, both during each treatment fraction (intrafractional movement) as a result of breathing, patient movement, or intestinal gas; as well as in between treatment fractions (interfractional movement) due to bowel and bladder filling, or patient weight gain or loss (8,9). They can also change size or shape throughout the course of radiotherapy treatments. An internal margin (IM), which varies in size depending on the patient and the anatomical location of the tumor, is added to the CTV in order to account for any known or expected motion of the tumor within the patient (9). A setup margin (SM) is added to the CTV as well, to account for any uncertainties in the patient position during treatment (9). This could be the result of small variations in the patient's setup position between treatment fractions, differences resulting from the transfer from simulator to the treatment machine, or mechanical errors in the treatment equipment. The IM and SM are combined based on a number of factors related to the geometry and biology of the treatment site (not necessarily simply added), and added to the CTV to form the planning target volume (PTV). The PTV represents the area that must be irradiated to ensure the coverage of the CTV.

1.1.3 Dose Sculpting

Once the PTV has been determined, the next step is to deliver sufficient radiation dose to the PTV to kill all of the cancer cells. One of the simplest methods is to use one or more open fields that cover the PTV (Fig. 1.4). This is done by taking a projection of the PTV in the treatment direction, and collimating a rectangular field such that it covers the entire PTV and as little additional area as possible. While an open field ensures complete coverage of the PTV, open fields also result in large regions of healthy tissue being irradiated.

With the advent of 3D imaging techniques, such as CT in 1972, more radiation beam sculpting was possible, giving rise to 3D conformal radiation therapy (3DCRT). In 3DCRT treatments, multiple beams are used from different treatment angles, with each beam collimated using a multi-leaf collimator (MLC) to the projection of the PTV in the beam's-eye-view (Fig. 1.4b). The use of multiple treatment angles and beams collimated to only cover the PTV greatly reduces the amount of healthy tissue irradiated, while still completely covering the PTV.

One limitation of 3DCRT treatments is that the radiation beam may be attenuated by different amounts at each treatment angle, or even from a single treatment angle by the tissues in front of different areas of the PTV. Because of this, 3DCRT can sometimes produce highly non-uniform dose distributions over the PTV. In order to ensure that the entire PTV receives the minimum required dose for tumor control, some regions of the PTV end up receiving much more dose than required. To address this issue, each radiation beam is divided into many small beamlets, where the intensity of each beamlet is individually modulated so that each region receives, as near as possible, only the minimum required dose (Fig. 1.4c). This is known as intensity-modulated radiation therapy (IMRT), and is capable of producing very uniform dose distributions covering the PTV.

Radiation therapy has seen a steady increase in the number of fields used to treat patients. Early radiation treatments consisted of one or very few fields delivered to the patient. In palliative treatments, where long term healthy tissue complications are not a concern, few fields are used. Additionally, fewer fields may be used in cases such as breast tumors, where a small number of fields can provide excellent tumor coverage

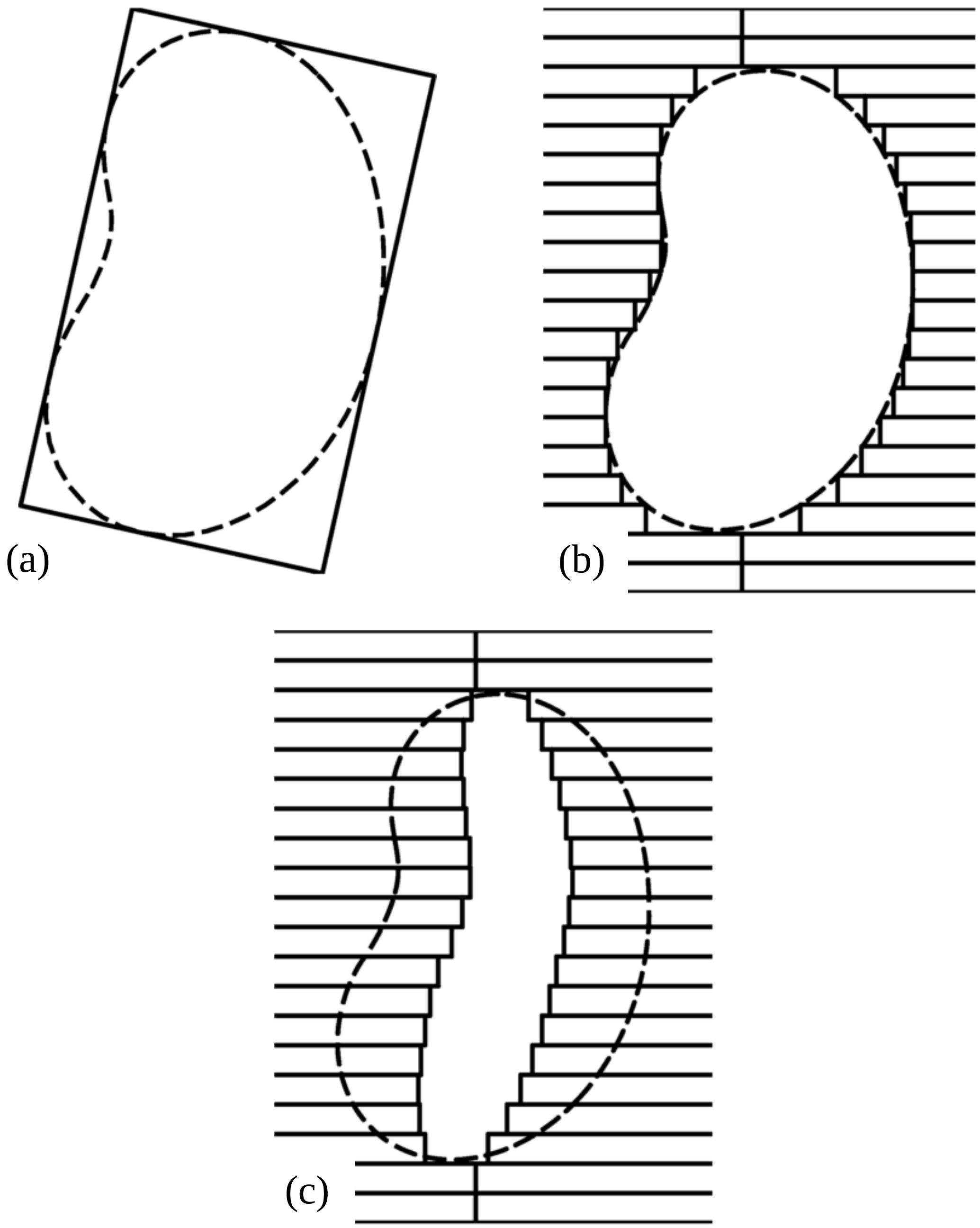

Figure 1.4: Different methods for sculpting dose to the tumor: (a) Open field: the field is collimated to the minimum bounding rectangle (solid line) covering the PTV (dashed line). There is considerable healthy tissue irradiated outside of the PTV. (b) Conformal radiation therapy: the radiation field is collimated using an MLC (solid lines) to conform to the PTV (dashed line). Much less radiation is delivered to areas outside of the PTV. The treatment will be repeated from multiple angles, with the MLC position adjusted to conform to the projection of the PTV in each treatment direction. (c) Intensity-modulated radiation therapy: The leaves of the MLC (solid lines) are moved continuously during treatment to account for the tissues in between radiation source and the PTV (dashed line) as well as to account for the dose delivered from other treatment directions. This results in a more uniform dose over the PTV.

without large doses to healthy tissues. The development of 3DCRT and IMRT increased the number of fields. While IMRT can produce very uniform dose distributions, radiation dose is delivered to healthy tissues along the treatment beams. If the patient is treated from more angles, the dose to the healthy tissue at each angle is lowered. To minimize the dose to any region of healthy tissue, and achieve even more uniform dose distributions, the treatment angle can be continuously changed during treatment, such that the patient is treated from every angle, in an arc, rather than from a few discrete angles. In the early 1990s Tomotherapy, a continuous arc treatment machine, was developed (10). Tomotherapy systems use binary leaves (either open or closed), and work by rotating around the patient during treatment, delivering a radiation strip to the tumor in a helical fashion, while an MLC inserts or retracts leaves from the beam, allowing portions of the radiation beam to be blocked. In 1995, volumetric modulated arc therapy (VMAT) was first proposed (11), where the beam is modulated independently (via the MLCs) at each treatment angle, allowing for extremely uniform dose distributions and low dose to healthy tissues. It took until 2008 before linac control systems were developed that were capable of delivering VMAT treatments (12).

1.1.4 IGRT

While developments in radiation delivery such as IMRT and VMAT have allowed dose distributions to better conform to the PTV, simultaneously efforts have been made to reduce the margins added to the CTV, to reduce the size of the PTV itself. The use of imaging throughout the course of radiation therapy to adjust the treatment is called image-guided radiation therapy (IGRT). There are many forms of IGRT, the simplest being to take the pre-treatment CBCT (13), MVCT (14,15), or EPID (16) images throughout the course of patient treatment to verify PTV location and patient positioning.

Imaging immediately prior to each fraction, although ensuring accurate patient positioning and PTV location, cannot account for patient motion *during* treatment. In order to account for motion, some form of PTV tracking (via imaging or by other means) is required during the treatment itself, so the treatment can be adjusted in real-time in response to tumor or patient motion. The beam may follow the tumor in real time, or simply be disabled or 'gated' when the tumor moves out of a specific region or a critical structure moves into the region. There are many different techniques for intra-fractional IGRT, and many different commercial technologies implementing those techniques, each with their own benefits and limitations (17,18).

One method to provide real-time IGRT is 2D fluoroscopic imaging. Fluoroscopy uses x-rays to obtain real-time images of the patient anatomy, in a single image plane. This allows in-plane motion of the tumor to be tracked directly and in real time. One limitation of using fluoroscopy is its inability to image out-of-plane motion. If the tumor moves a small amount, this may not be an issue, however if there is significant out-of-plane motion the dose received by the tumor may vary significantly from the planned dose. Out of plane motion can be accounted for using two or more orthogonal fluoroscopy images (19), which greatly increases the imaging radiation dose to the patient. The use of x-rays has limited soft-tissue contrast and results in increased dose to the patient. BrainLab Novalis (BrainLab, Feldkirchen, Germany), and Varian Truebeam (Varian Medical Systems, Palo Alto, CA) systems both use fluoroscopy to monitor patient treatment.

Fiducial markers are another common technology used to track the motion of a tumor during treatment. These are markers that can be tracked by the system, and the positions of the markers are then used to determine the position of the tumor. Fiducials can be internal or external, and can be tracked by a few different technologies. External fiducials are placed on the surface of the patient, and can be an IR emitting diode or IR reflector that can be tracked by an IR camera (20). Internal fiducials are markers that are surgically implanted into the patient, and may be radiopaque (21), for viewing on x-ray or fluoroscopic images; or RF emitting (22), to be tracked by RF receivers in the treatment room. This is an invasive procedure that is not without risk of infection (23) or perforation of organs such as the rectum (23), bladder (24), gall bladder (24) or lung (25) resulting in pneumothorax, or 'collapsed lung'. In at least one case, a fiducial marker was observed to have migrated through the hepatic vein to the right atrium of the heart (26). While the positions of fiducial markers themselves can be tracked extremely accurately, their location is used as a surrogate for tumor motion, and the accuracy of the correlation between the tumor position and the positions of the fiducials may be poor (as much as 0.9 cm error) (27). An additional limitation is that fiducials provide very limited information about tumor deformation (28). Accuray Cyberknife (Accuray Incorporated, Sunnyvale, California, USA) uses a combination of continuously tracked external-IR and frequently imaged internal-radiopaque fiducials, while Varian Calypso (Variean Medical Systems, Palo Alto, CA) uses internal-RF emitting fiducial markers.

No current IGRT systems are capable of providing real-time 3D imaging of the tumor during treatment. Some come close, offering real-time 2D imaging or fiducial monitoring, with occasional 3D updates to verify the correlation, but they suffer the same limitations mentioned above. Others offer fully 3D images before or between fractions, but not during each treatment fraction, which means tumor motion during treatment cannot be accounted for. Additionally, because many IGRT systems are fluoroscopy or x-ray based, they suffer from the poor soft tissue contrast and whole body radiation dose of x-ray imaging.

1.2 Linac-MR

1.2.1 What is Linac-MR?

Linac-MR systems are hybrid systems combining a linac, which produces the x-rays for radiation therapy treatments, with a magnetic resonance (MR) imager, which allows the tumor to be tracked during treatments. They are being built to address the shortcomings of current IGRT systems.

Using MR for IGRT offers several advantages over fiducial markers, fluoroscopy and x-ray imaging. MRI allows the tumor to be directly imaged, instead of inferred from the positions of the fiducial markers, and without the surgical implantation of any markers. It allows real-time imaging in 3D, with excellent soft tissue contrast (29,30), a large improvement over low contrast images produced by fluoroscopy, CBCT and other x-ray based systems, and without the need for ionizing radiation. The improved soft tissue imaging capabilities of MR also allows for treatments in areas that are difficult to treat using current IGRT technologies. Presently, cancers of the pancreas, kidneys, liver, oesophagus and rectum cannot be imaged accurately enough or seen with sufficient contrast for IGRT treatments.

Linac-MR systems will allow the CTV-PTV margin to be reduced significantly, or perhaps eliminated altogether. Because the patient is imaged during treatment, any setup variation or error can theoretically instantly and automatically be accounted for, reducing the need for an SM. Similarly, any motion could be imaged and automatically accounted for (31–33), reducing the need for an IM. With real-time 3D imaging of the GTV, the CTV could be treated directly, rather than treating a larger area, the PTV, to ensure coverage. This will allow increased dose to be delivered to the tumor, with the same healthy tissue toxicity, which is expected to improve patient outcomes. Presently, linac-MR systems use the MR images for patient setup, in a similar manner to current CBCT based IGRT, and use gating techniques (34,35) rather than automatically tracking the tumor with the radiation, where the radiation beam is disabled if the tumor leaves (or an organ at risk enters) the treatment field.

1.2.2 Linac-MR: technical challenges

There are two major shielding challenges when combining a linac with an MRI: shielding the magnet from the RF interference produced by the waveguide and related components, and shielding the linac waveguide from the fringe magnetic fields of the imaging magnet. The first problem can be solved (36,37) simply by placing an RF cage separating the magnet from the linac. The second depends on the orientation and strength of the magnetic field (38–40). Fields parallel to the waveguide have little effect on the waveguide, and only the gun must be shielded (40). When the fields are perpendicular to the waveguide, electrons are deflected by the Lorentz force from the magnetic field (38,39). In this orientation, much more shielding is required, along the entire length of the waveguide. The shielding could be active, using magnetic coils or permanent magnets placed around the waveguide such that the field produced is opposite to the fringe fields, reducing them sufficiently; or passive, placing metals with high magnetic permeability around the waveguide to draw the magnetic field lines away from the waveguide (39). It is expected that longer waveguides will require more shielding, as a smaller deflection is required before the beam exits the central beam tube of the waveguide.

1.2.3 Current Linac-MR Systems

Globally, there are a small number of groups working to design hybrid linac-MR systems. Each group is using different magnet designs and field strengths, different linacs, and different methods to integrate the linac and MR.

The Alberta Linac-MR project (Fig. 1.5a), is being developed at the Cross Cancer Institute in Edmonton, Alberta, Canada. The first prototype was installed in 2008, with a 0.2 T permanent magnet and a Varian 600C linac, and was the first system in the world to produce MR images during linac irradiation (41). The second (and current) prototype was installed in 2013 and uses a 0.56 T biplanar, high-temperature conduction-cooled (cryogen free) superconducting magnet with a yoke, which reduces the fringe magnetic fields (42). This system uses a Varian 600C linac, which can be positioned parallel to the main magnetic field, treating through a hole in the proximal pole plate, or perpendicular to the main magnetic field, treating between the pole plates. Passive magnetic shielding is used around the electron gun (in the parallel configuration) and the electron gun and linac waveguide (in the perpendicular configuration) to allow it to operate within the magnetic field (39,40). The linac and magnet assembly are rotated together around the patient to allow different treatment angles (42). The work in this thesis is part of the Alberta Linac-MR Project.

The Australia MRI-linac Program (Fig. 1.5b) at Liverpool Hospital in Sydney, Australia is a collaborative effort to produce a linac-MR between seven different research centers, including Stanford University, University of Sydney, and Liverpool Hospital, where the device is being built. This system uses a 1 T open-bore Helmholtz style magnet produced by Agilent Technologies Inc. (Santa Clara, California, USA). Radiation is produced by a Varian Linatron industrial linac, which produces a 6 MV photon beam, and can be positioned parallel or perpendicular to the magnetic field. The open design of the magnet produces large fringe magnetic fields at the linac position, which are reduced using active magnetic shielding (43). Different treatment angles are achieved by rotating the patient within the linac-MR, while the linac and MRI remain stationary.

The Elekta Atlantic linac-MR (Fig. 1.5c) located at the University Medical Center in Utrecht (UMC Utrecht) is being developed as a collaboration between UMC Utrecht, Elekta (Crawley, United Kingdom), and Philips (Amsterdam, Netherlands). The imaging is provided by a 1.5 T Achieva Philips MRI, a cylindrical helium-cooled superconducting magnet. An Elekta Agility linac capable of producing 8 MV x-rays is positioned perpendicular to the magnetic field such that it irradiates the patient through the MRI (44,45). The system uses active shielding to produce a zero field toroidal region through which the linac rotates while the magnet remains stationary, allowing treatment from any angle (44).

Siemens (Munich, Germany) has built a linac-MR (Fig. 1.5d) system using a "commercial 6 MeV linac" combined with a Siemens Magnetom Espree 1.5 T MRI, powered to 0.5 T (46). The MRI is a helium-cooled, cylindrical, superconducting

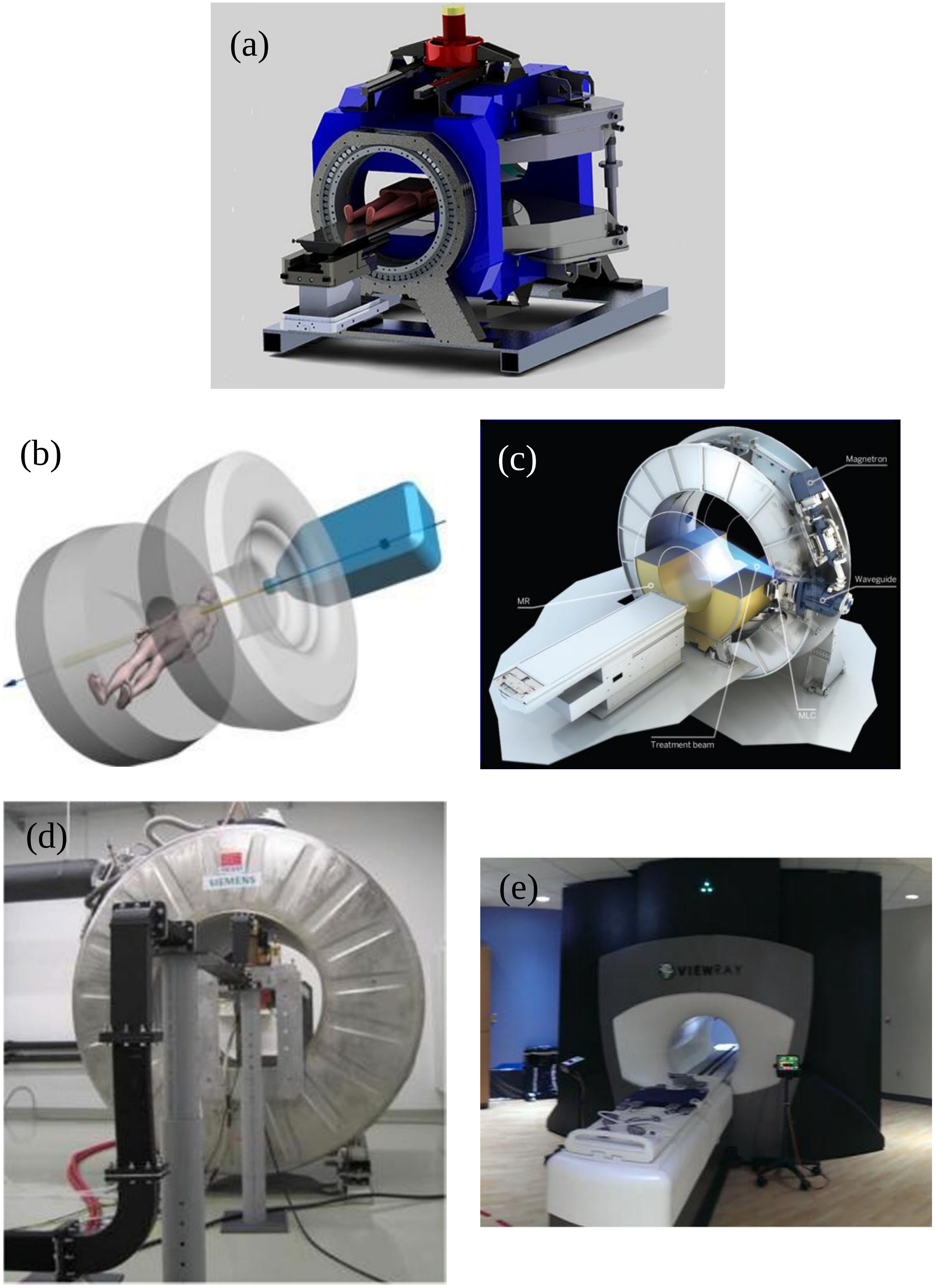

Figure 1.5: (a) Alberta Linac-MR, (b) Australia MRI-Linac Program. Image from (43), (c) Elekta Atlantic linac-MR. Image from https://www.elekta.com/investors/downloads/Elekta-ASTRO-2015-Webcast.pdf, (d) Seimens linac-MR. Image from (46), (e) ViewRay MRIdian cobalt-MR. Image from (47)

magnet (46). The linac is positioned inside the magnet bore, parallel to the imaging magnetic field, and the electron beam is magnetically deflected to the treatment direction using the main magnetic field and a series of dipole and quadrupole bend magnets (46). The homogeneous parallel magnetic fields inside the bore of the MRI do not interfere with the linac operation, so no shielding is required. The linac and bend magnets are rotated together within the bore of the stationary MRI to allow treatment from any direction (46).

The ViewRay MRIdian (Fig. 1.5e) system (Viewray Inc. Cleveland, Ohio) is not a linac-MR, because it uses cobalt-60 instead of a linac to produce the radiation for treatment (47). For comparison, the x-ray beam produced by cobalt-60 is roughly equivalent to a 4 MV photon beam (48). The imaging is provided by a split-bore 0.35 T split ring superconducting MRI. The split-ring design of the magnet allows three cobalt-60 sources to be positioned to treat perpendicular to the magnetic field without the beam passing through the magnet. The sources can rotate around the stationary magnet to treat from any direction. ViewRay has announced that they are developing a linac-MR system, called MRIdian Linac (49), but no details are available at this time.

1.2.4 Limitations of Current Systems

While linac-MR systems address nearly all of the shortcomings of current IGRT systems, there are limitations to the current generation of linac-MR systems: they are all restricted to a single energy of 6 or 8 MV (or Co-60), and are incapable of treating with higher energies. While this is suitable for many treatment cases, it results in sub-optimal dose distributions for some patients (presently approximately 50% of treatments performed at the Cross Cancer Institute are with energies greater than 6 MV). The use of

IMRT and VMAT reduce the difference between 6 MV and higher energy treatments, but there are still benefits to using higher energies (5).

To enable higher energy x-rays, given current technology, would require the use of a 1.5 m waveguide capable of producing 15 or 22 MV x-rays, because there are no 10 MV clinical linacs currently available. The physical size and orientation of the waveguide would necessitate considerable modification of the gantry design. The waveguide would be positioned perpendicular to the MRI fringe magnetic fields (in either treatment orientation). In this orientation, and with the longer waveguide, the shielding requirements are greatly increased. Additionally, the bend magnets, focusing coils, and buncher coils will interact with the imaging magnet, affecting field homogeneity and reducing image quality. Shielding a 1.5 m waveguide in this orientation and with these magnetic components is impractical.

An obvious approach to simplify the integration of a high-energy linac with the linac-MR is to position it inline, as in the case of our group’s parallel configuration with the current single-energy linac. This greatly simplifies the shielding requirements by removing the bend magnets, and in the parallel treatment orientation at least, reduces the effects of the fringe magnetic fields on the waveguide. The issue with this solution is that the system is now much too large to rotate around a patient inside a normally sized radiation therapy treatment vault. The total diameter of the rotating machine would be nearly 6 m, requiring purpose-built larger vaults, greatly increasing the installation cost of the machine.

1.3 Objective

The aim of this research is to design a new linac for use with the Alberta Linac-MR system. In order to treat a wide range of patients and cancer types, the new linac is designed to be a variable energy linac, capable of producing any energy required between 4 and 10 MV. To simplify the integration with the current linac-MR system as much as possible the new linac is designed to be an exact drop-in replacement for the 6 MV Varian 600C linac currently used. With no modification to the yoke, gantry, or shielding of the current linac-MR design required, the only modification needed is to the linac waveguide, x-ray target, electron gun (the yellow and red structures in Fig. 1.5a), and RF power source. Presently, no linac is capable of producing 10 MV x-rays using a short (27.5 cm) waveguide.

This research addresses one of the limitations of current linac-MR systems, by designing a high-energy linac to be compatible with linac-MR systems. While linac-MR systems are already a revolutionary advancement over conventional radiotherapy and IGRT techniques, the purpose of this research is to further improve treatments with linac-MR systems. A linac capable of producing energies from 4 to 10 MV, will ensure that linac-MR systems can deliver optimal dose distributions to nearly all patients currently treated with conventional external-beam radiation therapy, something not possible without this work. The improved treatment enabled by the use of the optimal energy for each patient is expected to further improve tumor control or reduce healthy tissue complications.

The impact of the newly designed linac is not limited to linac-MR, and may have widespread application in conventional radiotherapy as well. By greatly simplifying the design and construction of 10 MV, multi-energy linacs, such devices could be made nearly as cheap as current 6 MV linacs. For much of the developing world, where current high energy linacs are not affordable, a cheaper high energy linac would allow more optimal treatments for more tumor locations.

The design of the new linac was undertaken in three distinct phases. The objective of phase 1 (Chapter 3) was to demonstrate the feasibility of the project. The major concern when attempting to use a short linac to produce higher energy x-rays is electric breakdown (see Chapter 2). This phase of the research used an existing computer model emulating the Varian 600C linac waveguide and modeled the effect of replacing the 2.5 MW magnetron with a 7.5 MW klystron, and the resulting field strengths were compared to published breakdown thresholds. The RF fields within the waveguide were also rescaled to evaluate the effects of potential modifications to the waveguide to improve the output electron beam characteristics. Phase 2 (Chapter 4) was to design a 10 MV accelerator the same length (27.5 cm) as the Varian 600C linac. For this phase, a single accelerating cavity was produced to match cavity parameters from a published breakdown study (50). This cavity was used as the basis to design a full waveguide, which was then tuned to produce an electron beam which closely matches on produced by a currently used Varian 10 MV linac. Phase 3 entailed modifying the newly designed 10 MV waveguide such that the energy could be lowered as needed. This involved adjusting the input RF power and then adding an adjustable tuning cylinder to the first coupling cavity, so that the electron beam energy distribution could be optimized independently for each RF power level. For each energy desired, both the RF input power and the tuning cylinder position required optimization. Following these optimizations, Monte Carlo simulations were conducted to compare the dose distributions produced by the new linac with equivalent energy clinically used Varian linacs.

1.4 References

1. Crookes W. The Bakerian Lecture: On the Illumination of Lines of Molecular Pressure, and the Trajectory of Molecules. Philos Trans R Soc Lond. 1879 Jan 1;170:135–64.

2. On a New Kind of Rays. Nature. 1896 Jan 23;53(1369):274–6.

3. Grubbé EH. Priority in the Therapeutic Use of X-rays. Radiology. 1933 Aug 1;21(2):156–62.

4. Kerst DW. Acceleration of Electrons by Magnetic Induction. Phys Rev. 1940 Nov 1;58(9):841–841.

5. Pasler M, Georg D, Wirtz H, Lutterbach J. Effect of Photon-Beam Energy on VMAT and IMRT Treatment Plan Quality and Dosimetric Accuracy for Advanced Prostate Cancer. Strahlenther Onkol. 2011 Nov 29;187(12):792–8.

6. Followill DS, Nüsslin F, Orton CG. IMRT should not be administered at photon energies greater than 10 MV. Med Phys. 2007;34(6):1877.

7. Ekstrand KE, Barnes WH. Pitfalls in the use of high energy X rays to treat tumors in the lung. Int J Radiat Oncol Biol Phys. 1990 Jan;18(1):249–52.

8. Jones D. ICRU report 50: prescribing, recording and reporting photon beam therapy. ICRU Bethesda USA. 1994;

9. Wambersie A, Landgerg T. ICRU report 62: prescribing, recording and reporting photon beam therapy (supplement to ICRU Report 50). ICRU Bethesday USA. 1999;

10. Mackie TR, Holmes T, Swerdloff S, Reckwerdt P, Deasy JO, Yang J, et al. Tomotherapy: a new concept for the delivery of dynamic conformal radiotherapy. Med Phys. 1993;20(6):1709–1719.

11. Yu CX. Intensity-modulated arc therapy with dynamic multileaf collimation: an alternative to tomotherapy. Phys Med Biol. 1995;40(9):1435.

12. Otto K. Volumetric modulated arc therapy: IMRT in a single gantry arc. Med Phys. 2008 Jan 1;35(1):310–7.

13. Walter C, Boda-Heggemann J, Wertz H, Loeb I, Rahn A, Lohr F, et al. Phantom and in-vivo measurements of dose exposure by image-guided radiotherapy (IGRT): MV

portal images vs. kV portal images vs. cone-beam CT. Radiother Oncol. 2007 Dec;85(3):418–23.

14. Morin O, Gillis A, Chen J, Aubin M, Bucci MK, Roach III M, et al. Megavoltage cone-beam CT: System description and clinical applications. Med Dosim. 2006;31(1):51–61.

15. Ruchala KJ, Olivera GH, Schloesser EA, Mackie TR. Megavoltage CT on a tomotherapy system. Phys Med Biol. 1999;44(10):2597.

16. Herman MG. Clinical Use of Electronic Portal Imaging. Semin Radiat Oncol. 2005 Jul;15(3):157–67.

17. Balter JM, Cao Y. Advanced Technologies in Image-Guided Radiation Therapy. Semin Radiat Oncol. 2007 Oct;17(4):293–7.

18. Kataria T, Sharma K, Pareek P, Abhishek A, Bisht S, Govardhan H, et al. Frame-based radiosurgery: Is it relevant in the era of IGRT? Neurol India. 2013;61(3):277.

19. Shirato H, Shimizu S, Kitamura K, Nishioka T, Kagei K, Hashimoto S, et al. Four-dimensional treatment planning and fluoroscopic real-time tumor tracking radiotherapy for moving tumor. Int J Radiat Oncol. 2000 Sep;48(2):435–42.

20. Ford EC, Mageras GS, Yorke E, Rosenzweig KE, Wagman R, Ling CC. Evaluation of respiratory movement during gated radiotherapy using film and electronic portal imaging. Int J Radiat Oncol. 2002 Feb 1;52(2):522–31.

21. Litzenberg D, Dawson LA, Sandler H, Sanda MG, McShan DL, Ten Haken RK, et al. Daily prostate targeting using implanted radiopaque markers. Int J Radiat Oncol. 2002 Mar 1;52(3):699–703.

22. Willoughby TR, Kupelian PA, Pouliot J, Shinohara K, Aubin M, Roach M, et al. Target localization and real-time tracking using the Calypso 4D localization system in patients with localized prostate cancer. Int J Radiat Oncol Biol Phys. 2006;65(2):528–534.

23. Langenhuijsen JF, van Lin ENJT, Kiemeney LA, van der Vight LP, McColl GM, Visser AG, et al. Ultrasound-guided transrectal implantation of gold markers for prostate localization during external beam radiotherapy: complication rate and risk factors. Int J Radiat Oncol Biol Phys. 2007 Nov 1;69(3):671–6.

24. Kim JH, Hong SS, Kim JH, Park HJ, Chang Y-W, Chang AR, et al. Safety and Efficacy of Ultrasound-Guided Fiducial Marker Implantation for CyberKnife Radiation Therapy. Korean J Radiol. 2012;13(3):307–13.

25. Bhagat N, Fidelman N, Durack JC, Collins J, Gordon RL, LaBerge JM, et al. Complications Associated with the Percutaneous Insertion of Fiducial Markers in the Thorax. Cardiovasc Intervent Radiol. 2010 Dec;33(6):1186–91.

26. Hennessey H, Valenti D, Cabrera T, Panet-Raymond V, Roberge D. Cardiac embolization of an implanted fiducial marker for hepatic stereotactic body radiotherapy: a case report. J Med Case Reports. 2009;3:140.

27. Gierga DP, Brewer J, Sharp GC, Betke M, Willett CG, Chen GTY. The correlation between internal and external markers for abdominal tumors: Implications for respiratory gating. Int J Radiat Oncol. 2005 Apr 1;61(5):1551–8.

28. Poggi MM, Gant DA, Sewchand W, Warlick WB. Marker seed migration in prostate localization. Int J Radiat Oncol. 2003 Aug 1;56(5):1248–51.

29. Aisen A, Martel W, Braunstein E, McMillin K, Phillips W, Kling T. MRI and CT evaluation of primary bone and soft-tissue tumors. Am J Roentgenol. 1986 Apr 1;146(4):749–56.

30. Totty WG, Murphy WA, Lee JK. Soft-tissue tumors: MR imaging. Radiology. 1986 Jul 1;160(1):135–41.

31. Yun J, Mackenzie M, Rathee S, Robinson D, Fallone BG. An artificial neural network (ANN)-based lung-tumor motion predictor for intrafractional MR tumor tracking. Med Phys. 2012 Jul 1;39(7):4423–33.

32. Yun J, Wachowicz K, Mackenzie M, Rathee S, Robinson D, Fallone BG. First demonstration of intrafractional tumor-tracked irradiation using 2D phantom MR images on a prototype linac-MR. Med Phys. 2013;40(5):51718.

33. Brix L, Ringgaard S, Sørensen TS, Poulsen PR. Three-dimensional liver motion tracking using real-time two-dimensional MRI. Med Phys. 2014 Apr 1;41(4):42302.

34. Crijns SPM, Kok JGM, Lagendijk JJW, Raaymakers BW. Towards MRI-guided linear accelerator control: gating on an MRI accelerator. Phys Med Biol. 2011;56(15):4815.

35. Santanam L, Noel C, Wan H, Kashani R, Rankine LJ, Mazur TR, et al. Adequacy of Gating Margins for Abdominal Tumors of Patients Treated With Real-Time MR Guided Radiation Therapy. Int J Radiat Oncol • Biol • Phys. 2015 Nov 1;93(3):S216–7.

36. Lamey M, Burke B, Blosser E, Rathee S, De Zanche N, Fallone BG. Radio frequency shielding for a linac-MRI system. Phys Med Biol. 2010;55(4):995.

37. Lamey M, Yun J, Burke B, Rathee S, Fallone BG. Radio frequency noise from an MLC: a feasibility study of the use of an MLC for linac-MR systems. Phys Med Biol. 2010;55(4):981.

38. Constantin DE, Fahrig R, Keall PJ. A study of the effect of in-line and perpendicular magnetic fields on beam characteristics of electron guns in medical linear accelerators. Med Phys. 2011 Jul 1;38(7):4174–85.

39. St. Aubin J, Steciw S, Fallone BG. Effect of transverse magnetic fields on a simulated in-line 6 MV linac. Phys Med Biol. 2010;55:4861–9.

40. Santos DM, Aubin JS, Fallone BG, Steciw S. Magnetic shielding investigation for a 6 MV in-line linac within the parallel configuration of a linac-MR system. Med Phys. 2012;39(2):788–797.

41. Fallone BG, Murray B, Rathee S, Stanescu T, Steciw S, Vidakovic S, et al. First MR images obtained during megavoltage photon irradiation from a prototype integrated linac-MR system. Med Phys. 2009;36(6):2084–8.

42. Fallone BG. The Rotating Biplanar Linac–Magnetic Resonance Imaging System. Semin Radiat Oncol. 2014 Jul;24(3):200–2.

43. Keall PJ, Barton M, Crozier S. The Australian Magnetic Resonance Imaging–Linac Program. Semin Radiat Oncol. 2014 Jul;24(3):203–6.

44. Lagendijk JJW, van Vulpen M, Raaymakers BW. The development of the MRI linac system for online MRI-guided radiotherapy: a clinical update. J Intern Med. 2016 May 1;

45. Crijns S, Raaymakers B. From static to dynamic 1.5 T MRI-linac prototype: impact of gantry position related magnetic field variation on image fidelity. Phys Med Biol. 2014;59(13):3241.

46. Heid O, Kleemann M, Heller J. Integrated MRI-LINAC Radiotherapy Machine. Proc Int Soc Mag Reson Med. 2015;23:3068.

47. Mutic S, Dempsey JF. The ViewRay System: Magnetic Resonance–Guided and Controlled Radiotherapy. Semin Radiat Oncol. 2014 Jul;24(3):196–9.

48. Page BR, Hudson AD, Brown DW, Shulman AC, Abdel-Wahab M, Fisher BJ, et al. Cobalt, Linac, or Other: What Is the Best Solution for Radiation Therapy in Developing Countries? Int J Radiat Oncol. 2014 Jul 1;89(3):476–80.

49. ViewRay unveils plans for MRIdian Linac - MedicalPhysicsWeb. Available from: http://medicalphysicsweb.org/cws/article/research/64322

50. Tanabe E. Voltage Breakdown in S-Band Linear Accelerator Cavities. IEEE Trans Nucl Sci. 1983 Aug;30(4):3551–3.

2. Theory

2.1 Electromagnetism

In order to produce megavoltage x-rays for medical purposes, a beam of electrons is accelerated through a radiofrequency (RF) electromagnetic field. The beam is then stopped by a target, and the kinetic energy of the electrons is converted into x-rays through a process known as bremsstrahlung radiation. A linear accelerator waveguide is used to produce the standing wave RF fields used to accelerate the electron beam. An understanding of the behavior of electromagnetic fields, both in the interior (Section 2.1.2) and at the boundaries (Section 2.1.4) of the waveguide is important to model the functioning of the waveguide. Electromagnetic theory provides the equations necessary to model the waveguide and calculate the fields within.

2.1.1 Maxwell's Equations

A few equations of electromagnetism will not be derived here, and must be taken as essential postulates of electromagnetic theory (1). From a few such equations, most of what is required for the work presented in this thesis can be derived. The first thing that is required is the differential form of Maxwell's Equations:

$$\nabla \cdot \mathbf{E} = \frac{1}{\epsilon_0}\rho \tag{2.1}$$

$$\nabla \times \mathbf{E} = \frac{\partial \mathbf{B}}{\partial t} \tag{2.2}$$

$$\nabla \cdot \mathbf{B} = 0 \tag{2.3}$$

$$\nabla \times \mathbf{B} = \mu_0 \mathbf{J} + \mu_0 \epsilon_0 \frac{\partial \mathbf{E}}{\partial t} \tag{2.4}$$

where **E** is the electric field vector, ϵ_0 is the permittivity of free space, ρ is the volume charge density, **B** is the magnetic field vector, μ_0 is the permeability of free space, and **J** is the volume current density. In a medium, the electric and magnetic fields can cause a polarization,

$$\mathbf{P} = \chi\epsilon_0\mathbf{E}, \tag{2.5}$$

and magnetization,

$$\mathbf{M} = \frac{\chi_m}{\mu_0(1+\chi_m)}\mathbf{B}, \tag{2.6}$$

due to bound charges

$$\rho_b = -\nabla \cdot \mathbf{P} \tag{2.7}$$

and currents

$$\mathbf{J}_b = \nabla \times \mathbf{M} + \frac{\partial \mathbf{P}}{\partial t} \tag{2.8}$$

in the material. The total current and charge densities can be separated into bound and free components:

$$\rho = \rho_b + \rho_f \tag{2.9}$$

$$\mathbf{J} = \mathbf{J}_b + \mathbf{J}_f. \tag{2.10}$$

The auxiliary fields, **D**, and **H**, can now be defined as

$$\mathbf{D} = \epsilon_0\mathbf{E} + \mathbf{P} = \epsilon\mathbf{E} \tag{2.11}$$

$$\mathbf{H} = \frac{1}{\mu_0}\mathbf{B} - \mathbf{M} = \frac{1}{\mu}\mathbf{B}, \tag{2.12}$$

where the permittivity is $\epsilon = \epsilon_0(1+\chi)$ and the permeability is $\mu = \mu_0(1+\chi_m)$. Taking the divergence of equation 2.11 gives

$$\nabla \cdot \mathbf{D} = \epsilon_0 \nabla \cdot \mathbf{E} + \nabla \cdot \mathbf{P} = \rho - \rho_b. \tag{2.13}$$

This is the equivalent of equation 2.1 for the **D** field:

$$\nabla \cdot \mathbf{D} = \rho_f. \tag{2.14}$$

Similarly, taking the curl of equation 2.12 gives

$$\begin{aligned} \nabla \times \mathbf{H} = \frac{1}{\mu_0} \nabla \times \mathbf{B} - \nabla \times \mathbf{M} = \mathbf{J} + \epsilon_0 \frac{\partial \mathbf{E}}{\partial t} - \mathbf{J}_b + \chi \epsilon_0 \frac{\partial \mathbf{E}}{\partial t} \\ = (\mathbf{J} - \mathbf{J}_b) + \epsilon_0 (1 + \chi) \frac{\partial \mathbf{E}}{\partial t}, \end{aligned} \tag{2.15}$$

which is simply the equivalent of equation 2.4 for the **H** field:

$$\nabla \times \mathbf{H} = \mathbf{J}_f + \frac{\partial \mathbf{D}}{\partial t}. \tag{2.16}$$

The next thing that is required to model the waveguide is the behaviour of EM fields at an interface between two media (say medium 1 is a vacuum, and medium 2 is the conducting boundary of the waveguide). Across the interface between media 1 and 2, the electromagnetic fields must satisfy field continuity conditions. Considering the component of equation 2.1 parallel to the interface

$$\hat{\mathbf{n}} \times (\mathbf{E}_1 - \mathbf{E}_2) = 0 \tag{2.17}$$

$$\hat{\mathbf{n}} \cdot (\mathbf{B}_1 - \mathbf{B}_2) = 0 \tag{2.18}$$

$$\hat{\mathbf{n}} \cdot (\mathbf{D}_1 - \mathbf{D}_2) = 0 \tag{2.19}$$

$$\hat{\mathbf{n}} \times (\mathbf{H}_1 - \mathbf{H}_2) = 0 \tag{2.20}$$

where $\hat{\mathbf{n}}$ is the unit normal vector pointing from medium 2 into medium 1. A formal derivation of these is available in (1), and will not be included here. The continuity equations can be understood intuitively, however, from Maxwell's equations. In the absence of free (external) surface charges or currents, any discontinuities in the fields are due only to bound charges or currents, and therefore from equations 2.14 and 2.16, it is clear that the D and H fields must be continuous across the interface, giving rise to equations 2.19 and 2.20. Equation 2.1 implies that a surface charge density cannot result in a discontinuity of the electric field component parallel to the surface; while equation 2.4 implies that a surface current cannot result in a discontinuity of the magnetic field component perpendicular to the surface. This results in equations 2.17 and 2.18. From these equations, everything necessary to model the waveguide itself, and compute the fields within can be derived.

2.1.2 Helmholtz Equation

One of the first things that must be modeled in order to study waveguides is the behavior of electromagnetic fields in a vacuum. In theory, Maxwell's equations are sufficient to model this in its entirety, but in practice this is cumbersome and inefficient. It turns out that, in the absence of sources ($\rho, \mathbf{J} = 0$), and with the assumption that all fields are a single frequency (monochromatic), the equations that need to be solved can be greatly simplified. First apply the curl operator to both sides of equation 2.2. For the left-hand side, the well-known expression for the curl-of-a-curl is used, followed by equation 2.1 (remembering that $\rho = 0$) to get

$$\nabla \times (\nabla \times \mathbf{E}) = \nabla(\nabla \cdot \mathbf{E}) - \nabla^2 \mathbf{E} = -\nabla^2 \mathbf{E}\,. \tag{2.21}$$

The right hand side, using equation 2.4 (remembering now that $\mathbf{J} = 0$), gives

$$\nabla \times \left(-\frac{\partial \mathbf{B}}{\partial t}\right) = -\frac{\partial}{\partial t}(\nabla \times \mathbf{B}) = -\mu_0 \epsilon_0 \frac{\partial^2 \mathbf{E}}{\partial t^2}. \tag{2.22}$$

Setting the left hand side equal to the right hand side gives the wave equation for $\mathbf{E}$:

$$\nabla^2 \mathbf{E} = \frac{1}{c^2}\frac{\partial^2 \mathbf{E}}{\partial t^2}. \tag{2.23}$$

Identical manipulations and substitutions on equation 2.4 instead of 2.2 gives the wave equation for **B**:

$$\nabla^2\mathbf{B} = \frac{1}{c^2}\frac{\partial^2\mathbf{B}}{\partial t^2} \tag{2.24}$$

where $c^2 = 1/\mu_0\epsilon_0$. With a further assumption that the fields under consideration are monochromatic (with frequency ω), then **E** and **B** take on the form:

$$\mathbf{E}(\mathbf{r},t) = \mathrm{Re}\left[\tilde{\mathbf{E}}(\mathbf{r})e^{i\omega t}\right] \tag{2.25}$$

$$\mathbf{B}(\mathbf{r},t) = \mathrm{Re}\left[\tilde{\mathbf{B}}(\mathbf{r})e^{i\omega t}\right] \tag{2.26}$$

where $\tilde{\mathbf{E}}$ and $\tilde{\mathbf{B}}$ are the complex electric and magnetic amplitudes, respectively. Equation 2.25 and 2.26 are substituted into 2.23 and 2.24, respectively, the time derivatives are evaluated and then the sinusoidal terms (now on both sides of the equations) are cancelled to get the Helmholtz equations for **E** and **B**

$$\nabla^2\mathbf{E}(\mathbf{r}) + k^2\mathbf{E}(\mathbf{r}) = 0 \tag{2.27}$$

$$\nabla^2\mathbf{B}(r) + k^2\mathbf{B}(\mathbf{r}) = 0 \tag{2.28}$$

where the '~'s have been dropped for simplicity, and $k = \omega/c$ is known as the propagation constant. This is an extremely important result, as the time dependence has been completely removed from these equations. They can now be solved for the amplitude and phase as a function of position alone, and the sinusoidal time factor simply added at the end. These are the differential equations that will actually be solved using commercially available finite element solvers. Additionally, for a given geometry and boundary conditions, they can be solved for the eigenfrequencies, to determine at which frequency a given cavity will resonate.

2.1.3 Boundary Conditions (Perfect Electric Conductor)

In order to exactly model the effect of the conductive surface of a waveguide, some depth of the conductor itself must be modeled. However, because in a good conductor the electromagnetic fields drop off over an extremely small distance, to model this numerically in FEM (see section 2.5) requires a huge number of very small elements making it impractical to solve. Without sufficient computer memory to model the conducting surface of the waveguide exactly, the first choice is to approximate it as a perfect conductor. Since fields cannot be sustained within a perfect conductor, $\mathbf{E}_2, \mathbf{B}_2 = 0$, and boundary conditions 2.17 and 2.18 simplify to

$$\hat{\mathbf{n}} \times \mathbf{E}_1 = 0 \tag{2.29}$$

$$\hat{\mathbf{n}} \cdot \mathbf{B}_1 = 0, \tag{2.30}$$

while conditions 2.19 and 2.20 become

$$\hat{\mathbf{n}} \cdot \mathbf{D}_1 = \delta \tag{2.31}$$

$$\hat{\mathbf{n}} \times \mathbf{H}_1 = \mathbf{K} \tag{2.32}$$

where δ and $\mathbf{K}$ are a surface charge and current, respectively. It actually happens that condition 2.29 or 2.30 alone is sufficient to specify the behaviour at the surface of the conductor, and the remaining three conditions can be derived from either of these.

2.1.4 Boundary Conditions (Impedance)

Unfortunately, the finite conductivity of the boundary has an effect on the resonant frequency and the bandwidth of the waveguide (see section 2.3). Boundary conditions are therefore required which can include this effect, without requiring that the behaviour of the EM fields within the conductor itself be modeled. The standard index of refraction is given by(1)

$$N = \sqrt{\epsilon_r \mu_r}. \tag{2.33}$$

In a conductor, ϵ_r is complex

$$\epsilon_r = \left(\epsilon_r' + i\frac{\sigma}{\omega\epsilon_0}\right), \tag{2.34}$$

where ϵ_r' is the normal relative permittivity. The complex refractive index is therefore

$$N = \sqrt{\frac{\mu}{\mu_0}\left(\frac{\epsilon}{\epsilon_0} + i\frac{\sigma}{\omega\epsilon_0}\right)}, \tag{2.35}$$

where μ and ϵ are the permeability and permittivity, respectively and σ is the conductivity of the material. If the magnitude of the refractive index of the metal is large, as is the case for a good conductor, terms of $\mathrm{O}(1/N^2)$ can be neglected and approximate boundary conditions can be derived, similar to 2.29 and 2.30 to avoid the need to calculate fields within the metal itself. Expanding the divergence in equation 2.1 gives

$$\frac{\partial E_x}{\partial x} + \frac{\partial E_y}{\partial y} + \frac{\partial E_z}{\partial z} = 0 \tag{2.36}$$

which applies in either medium, but not at the boundary. Equation 2.17 requires that the components of the electric field parallel to the interface must be continuous. If the interface is defined to be parallel to the xy plane at $z = 0$, this implies that

$$E_{x1} = E_{x2} \tag{2.37}$$

$$E_{y1} = E_{y2} \tag{2.38}$$

and by differentiation that

$$\frac{\partial E_{x1}}{\partial x} = \frac{\partial E_{x2}}{\partial x} \tag{2.39}$$

$$\frac{\partial E_{y1}}{\partial y} = \frac{\partial E_{y2}}{\partial y}. \tag{2.40}$$

Applying this to equation 2.36 in each medium at the boundary gives

$$\frac{\partial E_{z1}}{\partial z} = \frac{\partial E_{z2}}{\partial z} \tag{2.41}$$

in the metal. The z component of equation 2.27 can be written as

$$\frac{\partial^2 E_{z2}}{\partial x^2} + \frac{\partial^2 E_{z2}}{\partial y^2} + \frac{\partial^2 E_{z2}}{\partial z^2} + k^2 N^2 E_{z2} = 0, \tag{2.42}$$

where k is the propagation constant in free space (medium 1). If $|N| \gg 1$, as in a good conductor, any incident wave is strongly deflected toward the normal (as can be seen by an application of Snell's law), which leads to $\partial^2 E_{z2}/\partial z^2$ being large when compared with $\partial^2 E_{z2}/\partial x^2$ and $\partial^2 E_{z2}/\partial y^2$, because of the rapid, exponential drop off in the fields in a good conductor. This means equation 2.42 can be approximated as

$$\frac{\partial^2 E_{z2}}{\partial z^2} + k^2 N^2 E_{z2} = 0. \tag{2.43}$$

This has a simple solution of the form

$$E_{z2} = Ae^{ikNz} + Be^{-ikNz}, \tag{2.44}$$

or a plane wave in the z direction, as expected. If the thickness of the metal is large compared to the penetration depth, and N is defined to have positive imaginary component, then the fields decay completely as $z \to \infty$. A must therefore be identically 0. Equation 2.19 requires that the z component of the displacement field be continuous across the boundary, or

$$E_{z2} = \frac{\epsilon_0}{\epsilon_r} E_{z1}. \tag{2.45}$$

Taking the derivative of equation 2.44 gives

$$\frac{\partial E_{z2}}{\partial z} = -ikNE_{z2} \tag{2.46}$$

which can be combined with equations 2.41 and 2.45 to get

$$\frac{\partial E_{z1}}{\partial z} = -ik\zeta E_{z1} \tag{2.47}$$

which is the impedance boundary condition on **E**, accurate to $O(\zeta)$, where ζ is defined for convenience as

$$\zeta = \frac{\mu}{\mu_0 N} = \frac{1}{\sqrt{\frac{\mu_0}{\mu}\left(\frac{\epsilon}{\epsilon_0} + i\frac{\sigma}{\omega\epsilon_0}\right)}}. \tag{2.48}$$

An identical analysis can be performed for **B**, with the key difference that at the boundary, instead of equation 2.45 the requirement is

$$H_{z2} = \frac{\mu_0}{\mu} H_{z1}. \tag{2.49}$$

This results in a slightly different final form for the second boundary condition

$$\frac{\partial H_{z1}}{\partial z} = -\frac{ik}{\zeta} H_{z1}. \tag{2.50}$$

As the orientation of the surface is completely arbitrary in this analysis, the unit vector, $\hat{\mathbf{z}}$, can be replaced with a unit vector pointing from medium 2 into medium 1, $\hat{\mathbf{n}}$, and these boundary conditions can be written in a more general form

$$\hat{\mathbf{n}} \cdot (\nabla E_n) = -ik\zeta E_n \tag{2.51}$$

$$\hat{\mathbf{n}} \cdot (\nabla H_n) = -\frac{ik}{\zeta} H_n \tag{2.52}$$

where E_n and H_n are the components of the fields parallel to $\hat{\mathbf{n}}$.

It is worth remembering now that the assumption of $|N| \gg 1$ was used to ensure that the fields within the medium were slowly varying along the surface. In order for this approximation to hold in a more general case for curved surfaces, the assumption must be generalized to $|N|kr \gg 1$ (2), where r is the radius of curvature of the surface. As long as appropriate care is taken not to violate the assumptions, equations 2.51 and 2.52

accurately capture the effect of the finite conductivity of the metal without requiring modelling of the metal itself.

2.2 RF Standing-Wave Waveguides

For a standing wave in an RF cavity, the axial electric field is given by (3)

$$E_z(z,t) = E_z(z,0)\cos(\omega t + \ \phi). \tag{2.53}$$

However, because an electron only ‘sees’ the field at the particular time it traverses a given location in the cavity, this expression can be rewritten as

$$E_z(z) = E_z(z,0)\cos(\omega t(z) + \phi) \tag{2.54}$$

where $t(z) = \int_0^z \mathrm{d}z/v(z)$ is the time that the electron is at position z. If the fields are restricted to a finite length accelerating gap from $-\ell/2$ to $\ell/2$, then the energy gained by an electron (or the work done on it by the fields) as it traverses the cavity is given by

$$W = q\int_{-\frac{\ell}{2}}^{\frac{\ell}{2}} E_z(z)\mathrm{d}z = q\int_{-\frac{\ell}{2}}^{\frac{\ell}{2}} E_z(z,0)\cos(\omega t(z) + \phi)\,\mathrm{d}z \tag{2.55}$$

where q is the charge of an electron and ϕ is the phase at which the electron enters the cavity. Rewriting the cosine by expanding the sum gives

$$W = q\int_{-\frac{\ell}{2}}^{\frac{\ell}{2}} E_z(0,z)[\cos\omega t(z)\cos\phi - \sin\omega t(z)\sin\phi]\mathrm{d}z. \tag{2.56}$$

This expression can be simplified if the axial RF voltage (at the time of maximum magnitude, when $\omega t = -\phi$) is defined as

$$V_0 \equiv \int_{-\frac{\ell}{2}}^{\frac{\ell}{2}} E_z(z,0)\mathrm{d}z \tag{2.57}$$

and the transit time factor, a unitless scaling factor which accounts for the finite time required for an electron to traverse the cavity, as

$$T \equiv \frac{1}{V_0}\left(\int_{-\frac{\ell}{2}}^{\frac{\ell}{2}} E_z(z,0)\cos\omega t(z)\,\mathrm{d}z - \tan\phi\int_{-\frac{\ell}{2}}^{\frac{\ell}{2}} E_z(z,0)\sin\omega t(z)\,\mathrm{d}z\right). \tag{2.58}$$

This allows equation 2.56 to be rewritten in a much simpler form

$$W = qV_0T\cos\phi. \tag{2.59}$$

In the cases of interest in this work, the RF fields are symmetric (or very nearly so) about the center of the RF cavity (that is, $E_z(z,0)$ is an even function), and so the second integral in equation 2.58 is identically 0, and the transit time factor simplifies to

$$T = \frac{\int_{-\frac{\ell}{2}}^{\frac{\ell}{2}} E_z(z,0)\cos\omega t(z)\,\mathrm{d}z}{\int_{-\frac{\ell}{2}}^{\frac{\ell}{2}} E_z(z,0)\mathrm{d}z}, \tag{2.60}$$

which is simply the field weighted average of the cosine as the electron passes through the cavity, and works as a weighting factor to account for the finite time taken by the electron to traverse the fields. The less time the electron takes to traverse the fields (ie. higher velocity or fields more concentrated near $z = 0$), the higher the transit time factor. Using this information, several figures of merit can be defined that will be useful to characterize the performance of the waveguide.

2.2.1 Quality Factor

The quality factor (or Q factor) of a resonator is defined very generally as the ratio of the energy stored in the resonator at steady state divided by the energy supplied by the power source (or equivalently, the power dissipated by the resonator), per cycle (time 2π) (3).

$$Q = \omega \frac{U}{P} \tag{2.61}$$

where U is the energy stored in the resonator and P is the power dissipated. Once the fields within an RF cavity have been calculated (using equations 2.27 and 2.28 along with boundary conditions 2.51 and 2.52) it is simple to determine both the energy stored, and the power dissipated. The energy density of an RF field is simply given by (1)

$$\eta = \frac{1}{2}\left(\epsilon_0 |\mathbf{E}|^2 + \frac{1}{\mu_0}|\mathbf{B}|^2\right), \tag{2.62}$$

which can be integrated over the volume of the cavity to get the total energy stored in the fields. The power is dissipated due to the finite conductivity of the surface (this is the primary source of power loss for non-superconducting cavities), and the power loss per unit area is simply the Poynting vector (1)

$$\mathbf{S} = \mathbf{E} \times \mathbf{H} \tag{2.63}$$

which, if integrated over the surface of the cavity will give the total power loss of the cavity. Because both equations 2.62 and 2.63 are proportional to the field strengths squared, the Q factor is independent of the field strength within the cavity. Typical values of the Q factor are 10^4 to 10^5 for normal conducting cavities, and 10^8 to 10^{10} for superconducting cavities.

2.2.2 Shunt Impedance

The next commonly used figure of merit is the shunt impedance. The shunt impedance measures how efficiently a cavity produces an axial voltage, and is defined as (3)

$$r_s = \frac{V_0^2}{P} \tag{2.64}$$

where V_0 is as defined in equation 2.57 and P is found by integrating equation 2.63. As with the Q factor, both numerator and denominator are proportional to the square of the field, and so the shunt impedance is also independent of the excitation level. For a particle accelerator, however, it is of more interest to consider the energy gained by an electron, rather than the axial voltage. The effective shunt impedance is defined to be (3)

$$r = \left(\frac{W}{q}\right)^2 \frac{1}{P} = \frac{(V_0 T)^2}{P} = r_s T^2. \tag{2.65}$$

This is just the shunt impedance scaled to account for the time required for an electron to traverse the cavity. Both the shunt impedance and effective shunt impedance are typically expressed in megaohms (MΩ). It is also often convenient to consider parameters which are independent of the length of the cavity, and so the shunt impedance per unit length is defined to be (3)

$$Z \equiv \frac{r_s}{\ell} = \frac{E_0^2}{P/\ell} \tag{2.66}$$

and the effective shunt impedance per unit length

$$ZT^2 = \frac{r}{\ell} = \frac{(E_0 T)^2}{P/\ell} \tag{2.67}$$

where E_0, the mean axial field, is defined to be V_0/ℓ and ℓ is the cavity length. For S-band linear accelerators, typical values for the shunt impedance per unit length are around 100 MΩ/m. When designing accelerator cavities, one of the objectives is to choose a geometry such that the shunt impedance per unit length is maximized, to maximize the efficiency of electron acceleration.

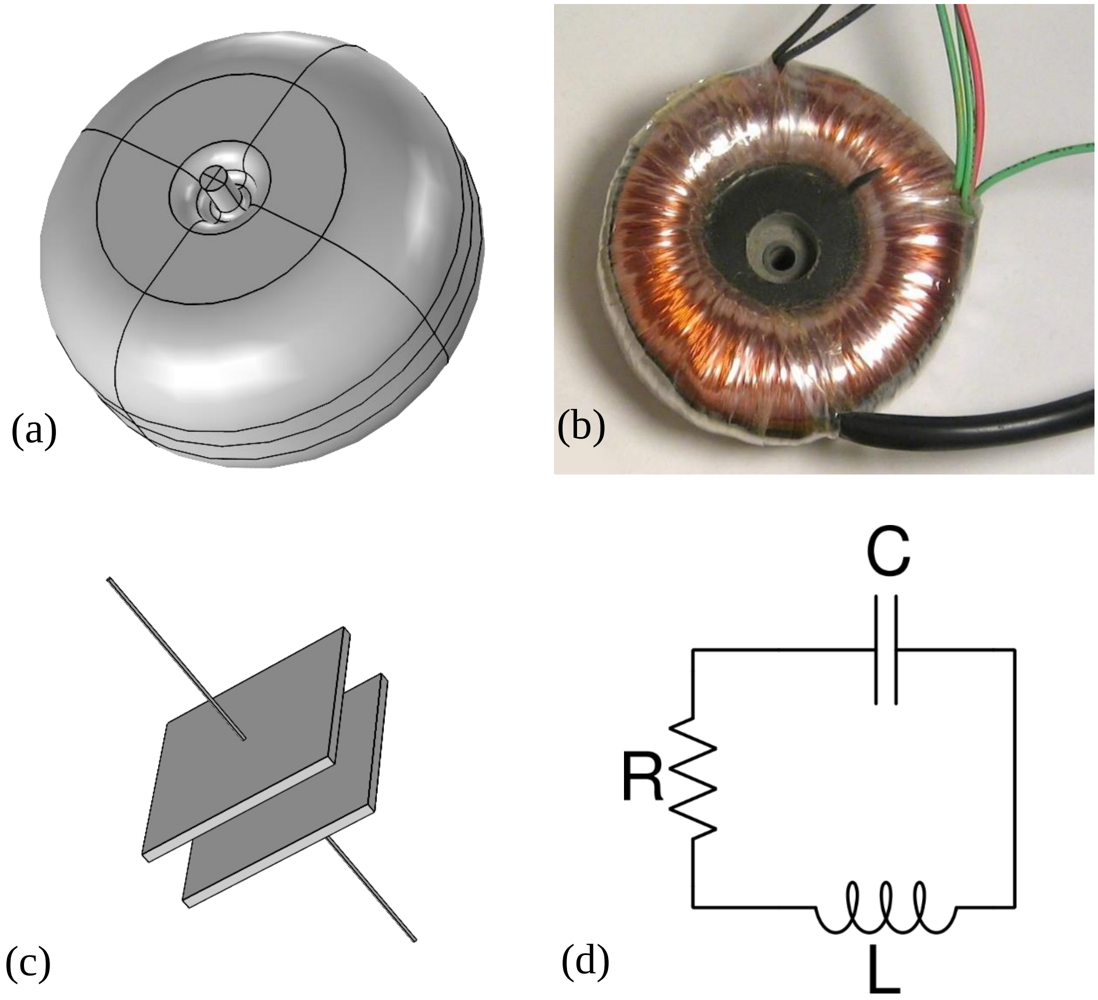

Figure 2.1: An RF cavity (a), has clear similarities to a toroidal solenoid inductor (b) and a parallel plate capacitor (c). This allows the cavity to be modelled as an RLC circuit (d). (Toroidal inductor image from https://en.wikipedia.org/wiki/Toroidal_inductors_and_transformers)

2.3 RF Resonators

2.3.1 Lumped-Circuit Model

In many cases in circuit analysis, it is convenient to treat properties of the circuit that are actually distributed over the entire circuit (such as the resistance of a wire) as a discrete component connected to the rest of the system by perfectly conducting wires. This is known as a lumped-circuit model of system, because the circuit components are "lumped" into discrete elements. A similar analysis is possible for an RF resonant cavity

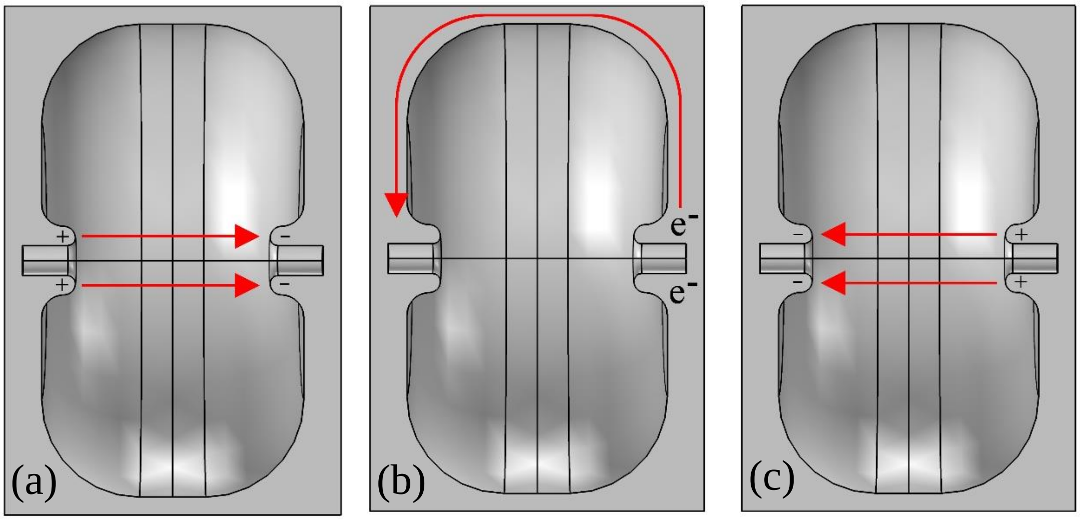

Figure 2.2: An RF cavity behaves as both a capacitor and an inductor. (a) The electric field points from left to right. A positive charge must have accumulated on the left nose cone and a negative on the right, as in a capacitor. (b) Electric current flows around the outside of the cavity, producing a toroidal magnetic field (field not shown). (c) The electric field now points from right to left, with opposite charge accumulation as in (a).

as well (4). Consider a toroidal coil inductor with the central portion of wire removed, or a parallel plate capacitor connected by the outer rim, the resemblance to an RF cavity (Fig. 2.1) can immediately be seen. Observing the fields in the cavity as they oscillate (Fig. 2.2), surface currents flow around the walls of the RF cavity in a similar manner to the current flowing through the coils of an inductor, and charge builds up at the ends of the cavity in a way analogous to the charge buildup in a capacitor. An RF cavity can therefore be modeled as a discrete capacitor connected to a discrete inductor, along with a resistor to account for the non-zero resistivity of the copper cavity walls (Fig. 2.1d).

It immediately becomes clear that an RF cavity is simply a specific example of the well-studied series RLC (resistor, inductor, capacitor where each of the components is in series) circuit, for which many properties are known. Other topologies of RLC circuits are possible, but for the remainder of this discussion only series RLC (and LC) circuits will be considered. An LC circuit behaves as a harmonic oscillator, with a resonant angular frequency given by (5)

$$\omega_0{}^{-2} = LC \tag{2.68}$$

where L is the inductance and C is the capacitance. Adding a resistor creates a damped harmonic oscillator, but does not affect the resonant frequency (in other topologies the addition of a resistor may affect the resonant frequency, and in fact may result in three different resonant frequencies: undamped, damped, and driven). The current (or voltage, which is proportional to the current) response of the circuit is a maximum if driven at the resonant frequency, and drops off as the drive frequency deviates from the resonant frequency. The width of the range of frequencies at which power passes through the circuit (as measured by the 3 dB points, or the frequencies at which the power drops to half of its maximum value) is known as the bandwidth, $\Delta\omega$, and equals R/L (R is the resistance) for an RLC circuit (5). The quality factor, Q, for an RLC circuit is given by

$$Q = \frac{\omega_0}{\Delta\omega} = \frac{1}{R}\sqrt{\frac{L}{C}}. \tag{2.69}$$

From these relations, it becomes apparent how the resonant frequency and Q factor can be adjusted by adjusting the cavity shape. Since capacitance for a parallel plate capacitor is given by (1)

$$C = \frac{A\epsilon_0}{d} \tag{2.70}$$

where A is the area of the capacitor plate and d is the gap between the plates, extending the nose cones reduces the gap and increases the capacitance. Similarly, inductance of a toroidal solenoid is given by (1)

$$L = \frac{\mu_0 N^2 H}{2\pi} \ln \frac{b}{a} \tag{2.71}$$

where H is the height of the inductor, a is the inner radius, b is the outer radius, and N is the number of turns. In a toroidal solenoid the current flows through the turns of wire. In contrast, in an RF cavity it is the surface area of the cavity over which the current flows. The introduction of the coupling iris between the accelerating and coupling cavity decreases the surface area over which current can flow and is analogous to decreasing the number of turns in an inductor, which decreases the inductance. Similarly, increasing the length of the nose cones increases the surface area over which current flows, and is analogous to increasing the number of turns, which increases the inductance. Similarly, increasing the outer radius of the cavity increases the inductance. The resonant frequency can therefore be increased by decreasing the nose cone length (which decreases both capacitance and inductance) or by reducing the outer radius of the cavity (which decreases the inductance only). The Q factor can be controlled by adjusting the outer radius of the cavity in order to control the inductance. While this lumped-circuit model of an RF cavity cannot be used to determine exactly how much to adjust the nose cones or cavity radius, it can at least predict what effect a given change is likely to have.

2.3.2 Coupled Resonators

Many properties of a linear accelerator can be investigated by modelling the cavities as coupled circuits (4), as in figure 2.3. This allows much about the operation of the waveguide to be determined from a few simple linear equations. The relevant parameters are straightforward to calculate, and this approximation allows the design of a waveguide that is more stable and more efficient than would otherwise be possible.

Beginning from a chain of $N+1$ identical cavities, terminated in half-cavities, the following circuit equations must be satisfied (4):

$$E_n = i_n\left(j\omega L + R + \frac{1}{j\omega C}\right) + j\omega k\frac{L}{2}(i_{n-1} + i_{n+1}) \tag{2.72}$$

for $n = 1, 2, \ldots, N-1$, and

$$E_0 = i_0\left(j\omega\frac{L}{2} + \frac{R}{2} + \frac{1}{2j\omega C}\right) + j\omega k i_1\frac{L}{2} \tag{2.73}$$

$$E_N = i_N\left(j\omega\frac{L}{2} + \frac{R}{2} + \frac{1}{2j\omega C}\right) + j\omega k_N\frac{L}{2} \tag{2.74}$$

for the beginning and final half circuits, where the circuit parameters are defined as in figure 2.3, i_n is the current and E_n is the drive voltage of the nth circuit. Dividing equation 2.72 by $j\omega\sqrt{L}$, and equations 2.73 and 2.74 by $j\omega\sqrt{L/4}$, and then making some substitutions results in a form that is more convenient to work with

$$\frac{E_n}{j\omega\sqrt{2L}} \equiv I_n = X_n\left(1 + \frac{\omega_0}{jQ\omega} - \frac{\omega_0^2}{\omega^2}\right) + \frac{k}{2}(X_{n-1} + X_{n+1}) \tag{2.75}$$

for $n = 1, 2, \ldots, N-1$, and

$$\frac{E_0\sqrt{2}}{j\omega\sqrt{L}} \equiv I_0 = X_0\left(1 + \frac{\omega_0}{jQ\omega} - \frac{{\omega_0}^2}{\omega^2}\right) + kX_1 \tag{2.76}$$

$$\frac{E_N\sqrt{2}}{j\omega\sqrt{L}} \equiv I_N = X_N\left(1 + \frac{\omega_0}{jQ\omega} - \frac{{\omega_0}^2}{\omega^2}\right) + kX_{N-1} \tag{2.77}$$

for $n = 0, N$, where ${\omega_0}^{-2} \equiv LC$, $X_n \equiv \sqrt{L}i_n$ and $Q = \omega_0 L/R$. This form of the equations is convenient because, despite being derived from the circuit analogy, they no longer depend explicitly on the circuit properties, and are more generally applicable to any chain of coupled resonators (4). Note the I_n correspond to a drive term for a resonator, and $\frac{1}{2}{X_n}^2 W(n)$ is the energy stored in each resonator ($W(n)$ is a weighting

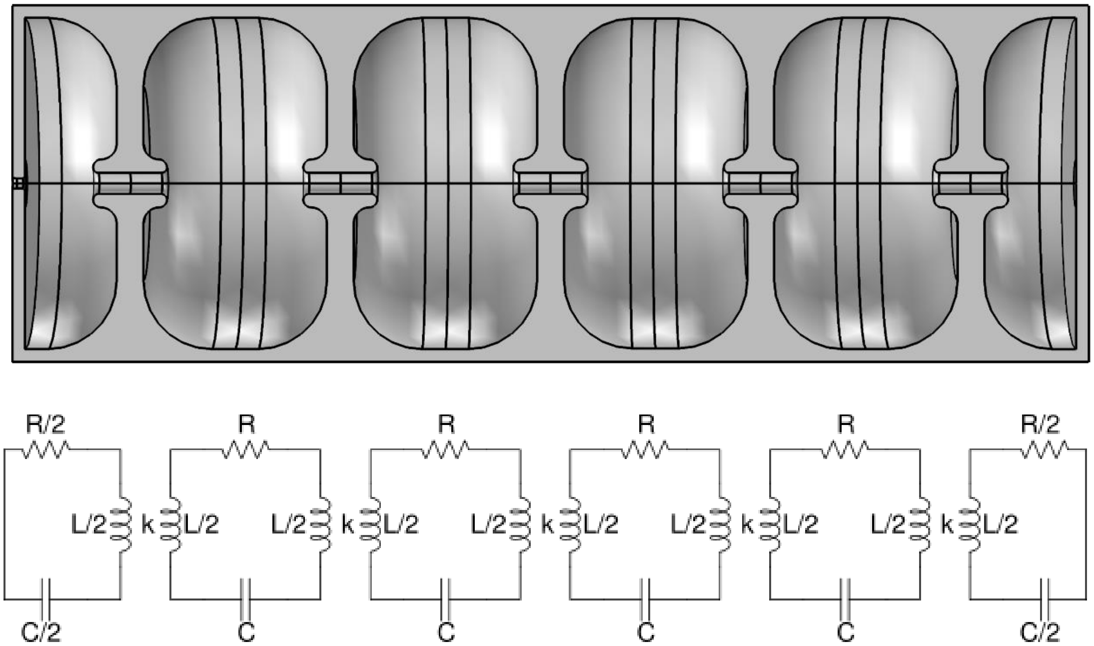

Figure 2.3: A diagram showing the correspondence between a chain of coupled RF cavities and a series of coupled RLC circuits. R is the resistance, L is an inductance (which has been divided over two discrete inductors, to more easily illustrate inductive coupling between cavities), k is the coupling constant between cavities, and C is the circuit capacitance.

term equal to 1/2 for $n = 0, N$, and 1 otherwise), and Q and ω_0 are the standard oscillator quality factor and resonant frequency, respectively (as defined in section 2.2.1). When Q is large, there are $N + 1$ solutions to the homogeneous ($I_n = 0$) equations

$$ {X_n}^{(q)} = A \cos\frac{\pi q n}{N} e^{j\omega_q t} \tag{2.78} $$

where q is the mode number, A is an arbitrary constant and

$$ {\omega_q}^2 = \frac{{\omega_0}^2}{1 + \cos\frac{\pi q}{N}} \tag{2.79} $$

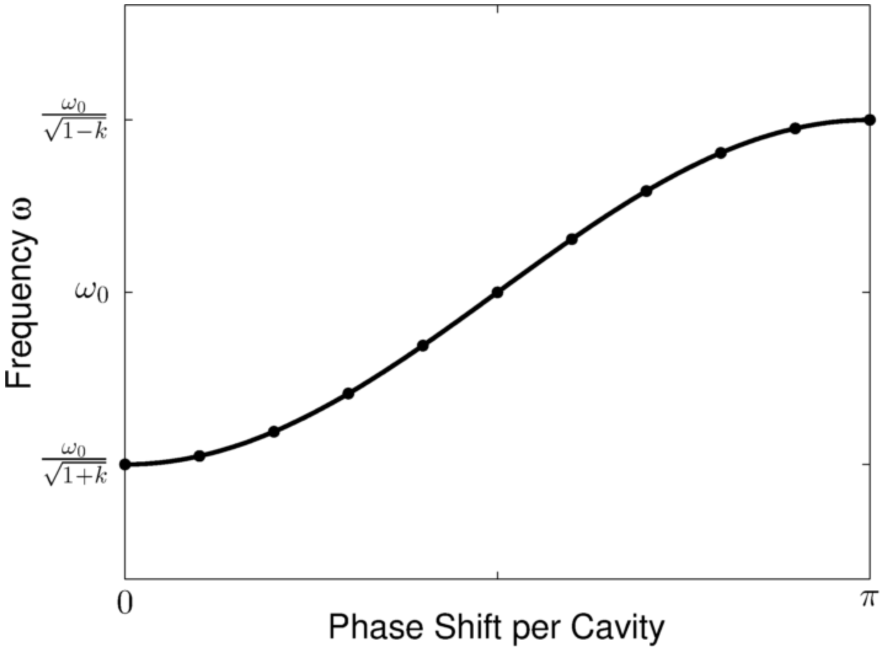

Figure 2.4: Dispersion curve for a chain of coupled resonators. The solid line represents the dispersion relation for an infinite, periodic chain of coupled resonators, while the points are modes of a chain of nine coupled resonators.

is the dispersion relation (4). As $N \rightarrow \infty$, this becomes a continuous function and can be written as (4)

$$\omega_q{}^2 = \frac{\omega_0{}^2}{1 + k\cos\phi} \tag{2.80}$$

where ϕ is the phase shift per cavity. From the plot in figure 2.4 (or from differentiating equation 2.80 when k is small) it is clear that the slope is maximum at a phase shift of $\pi/2$, which means for finite chains, that the separation between modes is largest for the $\pi/2$ mode. Because of the finite bandwidth, as well as mode shifts due to imperfections in the manufacturing of a waveguide, the larger separation between modes results in more stable operation by preventing mode mixing. Additionally, in the $\pi/2$ mode, cavities alternate between node and anti-node, and (almost) no energy is stored in the coupling cavities (4). This maximizes the energy available to accelerate electrons in the accelerating cavities.

2.4 Electric Breakdown

Production of a 10 MV photon beam from a short waveguide requires increasing the RF input power (supplied by a magnetron or klystron power source), which is limited by electric breakdown in the waveguide. This occurs when the RF field strengths within the waveguide get too high, and arcing occurs across the cavity (6). This arc absorbs the RF power, which prevents the waveguide from functioning as an accelerator, and can actually damage the waveguide itself over time. The arcing can be caused by microscopic protrusions of metal cause an enhancement of the electric field, by factors of 100 or more, on a microscopic scale (6). This results in current densities up to 10^{13} $\mathrm{A/m^2}$ from a tiny region (6). An alternative source of arcing is microscopic metal oxides, which generally have a lower work function than pure metals, and therefore emit much larger currents. The metal protrusion or imperfection is heated through resistive heating, eventually forming a plasma which spreads in the waveguide (6). The plasma can then liquefy small amounts of metal, which creates additional imperfections from which future arcs can occur, and gradually deforms the cavity until it no longer resonates at the correct frequency (6).

Because of the random nature of electric breakdown and the complex interaction between surface finishing, cavity geometry, and any additional deformation from other sources, it is impossible to theoretically predict the threshold for electric breakdown for any given cavity (7). Surface finishing and polishing can reduce the number and size of imperfections in the surface, which results in less enhancement of the electric field, so higher power levels can be used before breakdown occurs (6). After construction, the cavity undergoes RF processing, where the RF field strength is gradually increased to "burn off" imperfections in a controlled manner without damaging the waveguide (6). Improvements to surface finishing and RF processing can greatly increase the threshold for breakdown in a cavity (7). Additionally, improved vacuum and metal purity can decrease the number of metal-oxide deposits, removing potential sources for arcing. Thresholds are also extremely dependent on the geometry, as the geometry determines how easily the plasma can arc across the cavity. The RF frequency is another factor which affects the breakdown threshold. Higher frequencies mean a shorter heating duration and a shorter time over which the plasma must traverse the cavity, and therefore have much higher breakdown thresholds (8). The process is not completely understood, and cannot currently be predicted for a specific cavity geometry. Phenomenological models fit to experimental measurements must be relied upon to assess whether a specific cavity will break down.

In 1957, W.D. Kilpatrick published the first generally applicable threshold for electric breakdown (9). Working from RF and DC results, Kilpatrick fit experiments and extrapolated to produce an expression for the field strength below which breakdown does not occur

$$f = 1.64\ \mathrm{MHz} \cdot \left(\frac{E_{\mathrm{th}}}{1\ \mathrm{MV/m}}\right)^2 e^{-\frac{8.5\ \mathrm{MV/m}}{E_{\mathrm{th}}}} \tag{2.81}$$

where f is the operating frequency, and E_{th} is the threshold electric field within the waveguide. If the fields do not exceed E_{th} anywhere in the waveguide, breakdown is not expected. At the operating frequency of the Varian 600C and our proposed linac of 2997 MHz, this results in a threshold electric field of only 46.8 MV/m beyond which breakdown occurs. This is exceeded by the Varian 600C, which has peak fields around 125 MV/m and operates without electric breakdown (10). This is possible in part because Kilpatrick’s criterion was extrapolated from low frequency results, limiting the applicability, but also because of improved vacuum technology (10^{-1} to 10^{-5} Pa, compared to 10^{-8} Pa used for modern linacs) and the lack of surface finishing or RF processing in Kilpatrick’s experiments.

A more recent expression, which addresses many of the issues with Kilpatrick’s work, was published by Wang and Leow in 1989 (11). They fit multiple experiments at different frequencies (from 2.8 to 11.4 GHz) and used modern vacuum systems and finishing techniques to create the expression

$$E_{\mathrm{th}} = 220\ \mathrm{MV/m} \cdot \left(\frac{f}{1\ \mathrm{GHz}}\right)^{\frac{1}{3}} \tag{2.82}$$

which is much more relevant to this work. This is the expression used to assess the feasibility of producing a short, high-energy linac (chapter 3). However, because it is a fit to multiple experiments, and neglects the dependence of breakdown thresholds on cavity geometry that is present even for cavities operating at the same frequency, either a geometry specific measurement, or a geometry independent measurement would be more ideal.

Recent experiments done by Dolgashev et al. suggest that using magnetic field strength instead of electric field strength may yield such a geometry-independent threshold (12). These experiments were performed in the x-band, at 11.4 GHz, so the result is not necessarily applicable to this work.

For this work, the most relevant publication of a breakdown experiment was by Tanabe in 1983 (13). He designed and built three cavities which resonate at the same frequency as intended for this work, and measured the electric fields when breakdown occurred. For each cavity, the shunt impedance, Q factor, and the ratio between the peak

Cavity	1	2	3
Q	18520	18411	16835
ZT^2	104	117.1	130.2
E_p/E_0	3.61	6.04	8.08
E_{th}	239.4	263.1	246.4
$E_{0\mathrm{th}}$	66.3	43.6	30.5

Table 2.1: The cavity parameters published by Tanabe. Q is the quality factor, ZT^2 the shunt impedance, E_p/E_0 is the ratio between the peak fields within the waveguide and the average axial field, as defined in section 2.3.2, E_{th} is the peak fields within the waveguide when breakdown occurred and $E_{0\mathrm{th}}$ is the average axial field at breakdown.

surface fields and the average axial fields were also published (Table 2.1), providing sufficient information to match the nose cone geometry used in the experiment. The experiments done by Tanabe used a vacuum pressure of 10^{-5} Pa, and 1 hour of RF processing time with a single, low RF power level. For comparison, modern linear accelerators operate at a vacuum pressure of 10^{-8} Pa, and 3 to 14 hours RF processing with gradually increasing RF power is required to maximize the breakdown threshold (7). Because of these improvements in vacuum pressure and RF processing, the actual thresholds using modern technologies are expected to be considerably higher than those published by Tanabe. The cavity design and field acceptance in chapters 3 and 4 are based on the numbers published by Tanabe, and do not depend on additional improvements. The improvements are noted here to clarify that there is a larger margin of safety than indicated by numbers published by Tanabe.

2.5 Finite Element Method

In order to calculate the RF fields within a waveguide, equations 2.27 and 2.28 must be solved, subject to the boundary conditions in equations 2.51 and 2.52. While these equations are simple to derive and write down, for most geometries more complex than a simple cylinder or sphere, there exist no closed-form solutions. Numerical methods must be deployed to solve the problem. One such method, often used in electromagnetic applications, is the finite element method (FEM). In very general terms, FEM involves four steps (14): creating a mesh to discretize the domain of the problem into a set of sub-domains (called mesh elements), choosing a set of basis functions, assemble a matrix equation representing the system of equations on the mesh elements, and solving the system of equations.

2.5.1 Discretization

2.5.1.1 Element Shape

The first step when using FEM to solve a differential equation is to divide the domain of the problem into subdomains (14). In one dimensional problems, the mesh elements consist of line segments that cover the domain. For two dimensional problems, triangles or quadrilaterals (or a combination of the two) can be used as mesh elements, depending on the particular domain. Three dimensional problems can be discretized using tetrahedrons (Fig. 2.5), triangular prisms, or bricks. Other shape elements are possible in two or three dimensions, but are rarely used; most finite element software packages include these options. Triangular (in two dimensions) and tetrahedral (in three dimensions) elements are the best suited to model arbitrary volumes, as they can closely approximate any surface or edge; they should be used unless the specific geometry being modelled is especially suited to another element shape (14).

2.5.1.2 Delaunay Triangulation

Once a mesh element shape and order has been chosen, an incremental Delaunay Triangulation is used to generate the mesh. Delaunay triangulation is actually a process by which a mesh can be optimized, rather than produced (15). It examines each mesh element to ensure that no other vertices lie within its circumcircle (or circumsphere, in

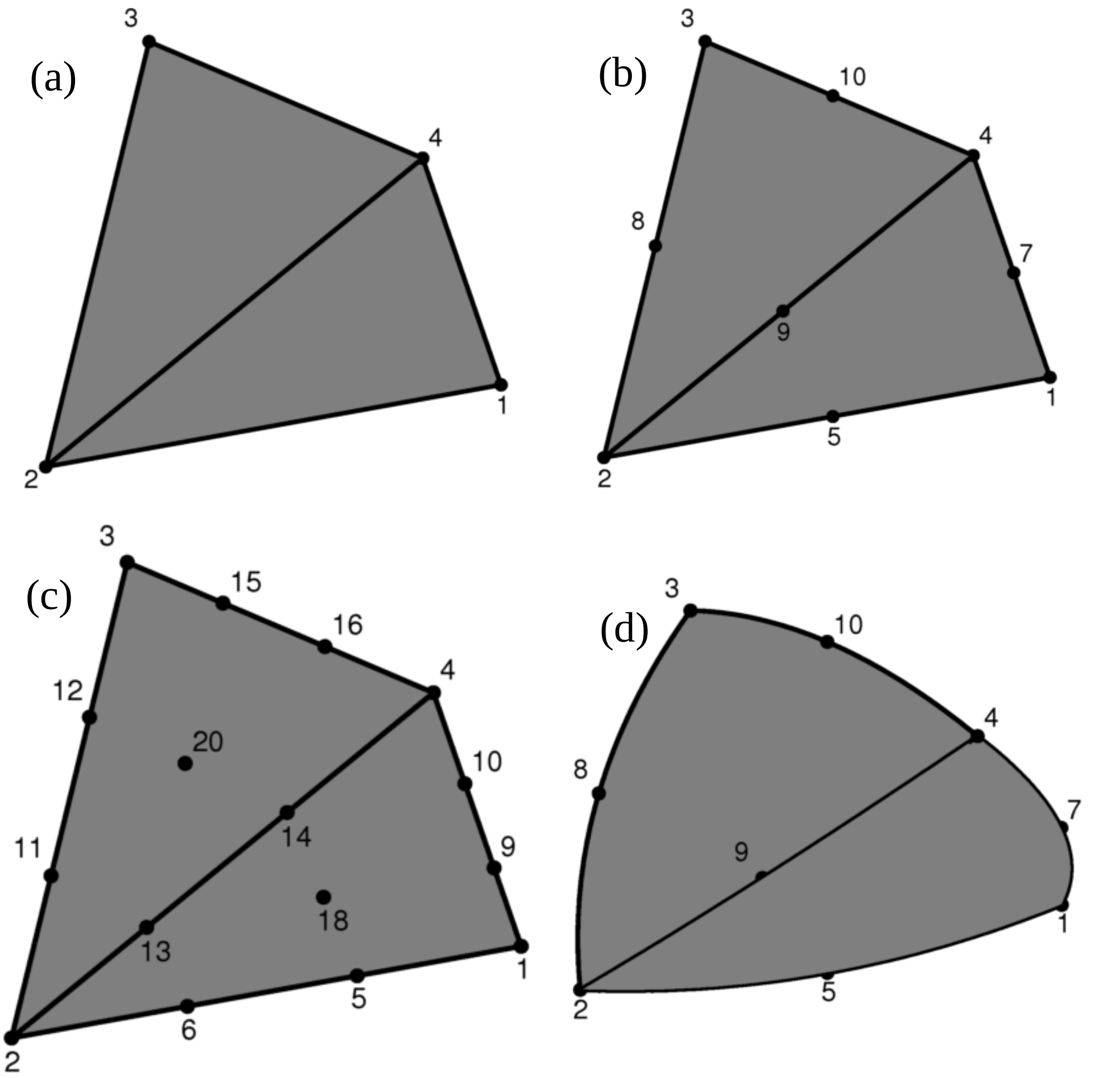

Figure 2.5: First (a), second (b), and third (c) order tetrahedral elements, with node numbering. Isoparametric tetrahedral elements (d) can have curved sides to better fit geometric boundaries.

three dimensions). If a vertex is found within the circumcircle, one edge can be flipped (Fig. 2.6) such that it this is no longer the case. In order to actually generate the mesh, an incremental approach is used (Fig. 2.7). In this approach, a coarse mesh is examined, and a new vertex is inserted at: 1. the center of any encroached segments (a segment is "encroached" if its diametral circle contains any other points) or 2. the circumcenter (center of the triangle's circumcircle) of a triangle that does not meet constraints. Constraints can be on the element size or the minimum element quality, which is based on the ratio of the radii of inscribed to circumscribed circles or spheres (long, thin elements have a low quality). All elements whose circumcircles contain the new point are deleted, and reconnected using the new point to generate a new mesh. The process is repeated on the new mesh, until all elements meet the constraints. Edges are meshed first to the desired size (usually determined by a combination of the desired solution accuracy, the radius of curvature of the edge, and the specific differential equations to be solved). Following this, a few vertices are added to the boundaries and connected to the edge mesh points, and optimized using Delaunay triangulation. The boundary mesh is then refined using incremental Delaunay triangulation until it meets the minimum criteria. Similarly, a few vertices are then added to the 3D domain under consideration, optimized using Delaunay triangulation and then refined using incremental Delaunay triangulation.

2.5.1.3 Element Nodes

Each mesh element has a set of nodes associated with it. The simplest elements in three dimensions are linear tetrahedral elements, which require 4 nodes, one at each vertex (14). For each node, the xyz coordinate values, local number, and global numbers must be stored. The local number (Fig. 2.5) references each node within an element and is between 1 and the number of nodes in each element, n_e. The global number references the node in the entire system and is between 1 and the number of nodes in the entire mesh, N_n. Nodes on the boundary between mesh elements will have the same global number, but a different local number in each element that it is a part of.

If an N_D dimensional problem with N_e elements, N_n nodes, and n_e nodes per element is being solved, two matrices are created to store the node details (14). The first is called the $\mathbb{P}$-matrix (or position-matrix) as it stores the xyz coordinates of each node,

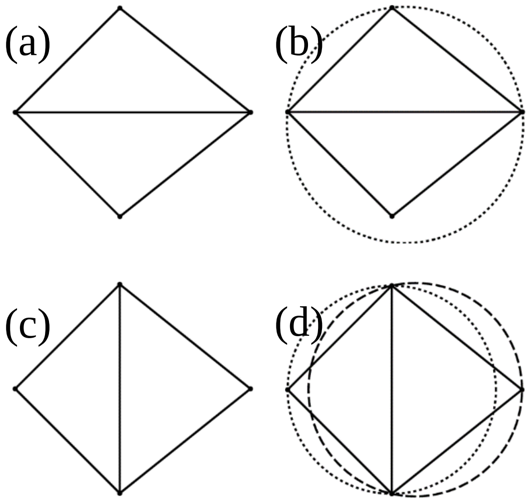

Figure 2.6: Fixing suboptimal triangulation by flipping one edge. (a) Beginning triangulation. (b) Check to see if any vertices outside a triangle are contained within its circumcircle. (c) Switch the shared edge, creating two new triangles. (d) The circumcircle of each triangle now only contains the vertices of that triangle.

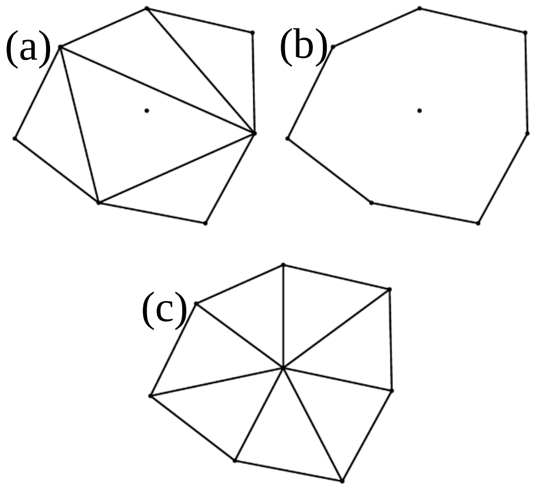

Figure 2.7: Incremental Delaunay triangulation: (a) Add a point in an existing mesh. (b) Remove all triangles whose circumcircle contain the added point. In this case, that is all the triangles. This leaves a "star shaped" polygonal hole in the mesh, in which all exposed vertices can be directly connected to the new point. (c) Retriangulate the hole using the new point.

referenced by the global number. The $\mathbb{P}$-matrix is an $N_n \times N_D$ matrix where $P_{i,j}$ is the jth coordinate of the ith node. The second is called the $\mathbb{T}$-matrix, and stores the reference between the local node numbers and the global node numbers. The $\mathbb{T}$-matrix is an $N_e \times n_e$ matrix, where $T_{i,j}$ is the global number of the jth (local number) node of the ith element. The xyz coordinates of the 3rd node of the 10th element, for example, can be found as column $T_{10,3}$ of the $\mathbb{P}$-matrix. When assembling the matrix equation, FEM usually results in a sparse, banded matrix (a matrix with of mostly zeroes, with all entries outside of a central diagonal band being zero), with the bandwidth (largest distance of non-zero entries from the diagonal) determined by the maximum difference between global numbers of nodes in each element (14). The memory and computational cost of

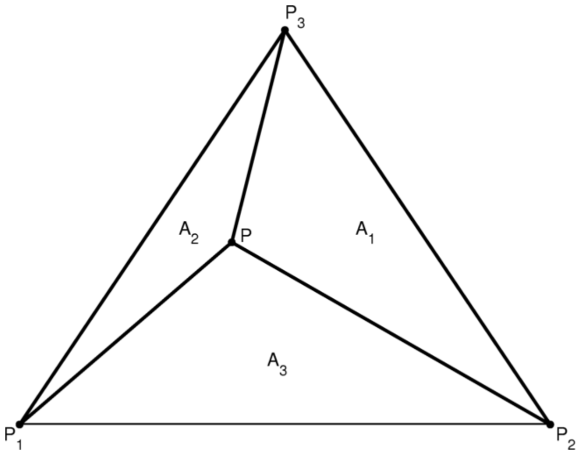

Figure 2.8: The ith barycentric coordinate, λ_i is found by taking A_i/A, wher A is the area of the entire triangle $P_1P_2P_3$.

banded matrix solvers is greatly reduced for low band-width matrices, making careful numbering of the nodes important.

2.5.1.4 Barycentric Coordinates

It is convenient to define a set of barycentric coordinates (also known as volume or area coordinates) internal to each element. Given a triangle with vertices at P_1, P_2, and P_3 and a point P within the triangle (Fig. 2.8), the ith coordinate, λ_i, is defined as the ratio of the area of the triangle made by replacing the ith vertex of the triangle with point P to the area of the triangle $P_1P_2P_3$. For example, the first area coordinate would be the area of triangle PP_2P_3, divided by the area of triangle $P_1P_2P_3$. It is immediately clear that λ_i is 1 at the ith vertex, and 0 along the opposite edge. The generalization to three dimensional tetrahedrons simply involves one additional coordinate and the use of volumes instead of areas. Conversion from the barycentric coordinates, λ_i to Cartesian coordinates, xyz is simply a weighted average of the coordinates of the vertices of the triangle.

$$x = \sum_i \lambda_i x_i$$
$$y = \sum_i \lambda_i y_i \, . \tag{2.83}$$
$$z = \sum_i \lambda_i z_i$$

2.5.1.5 Higher Order and Isoparametric Elements

Once a mesh-element shape has been selected (or shapes), the element order must be chosen. A linear tetrahedral element (Fig. 2.5a), for example, has four nodes, one at each vertex. Higher order, quadratic or cubic, elements are also possible, and allow the use of higher order basis functions to more accurately approximate the solution to the differential equation. Quadratic, or second order, tetrahedral elements (Fig. 2.5b) require 10 nodes, while cubic, or third order, tetrahedral elements (Fig. 2.5c) require 20 nodes each. In general, nth order tetrahedral elements have nodes positioned where $\Lambda_i = n\lambda_i$, the four barycentric coordinates multiplied by the element order, are all integer. Thus Λ_1 can take on the values 0 to n, Λ_2 can take on values from 0 to $n - \Lambda_1$, and Λ_3 the values from 0 to $n - \Lambda_1 - \Lambda_2$. The choice of Λ_1, Λ_2, and Λ_3 fixes the value of Λ_4, so the total number of nodes is given by

$$\sum_{\Lambda_1=0}^{n} \sum_{\Lambda_2=0}^{n-\Lambda_1} n + 1 - \Lambda_1 - \Lambda_2 . \tag{2.84}$$

These are simply finite arithmetic series, which are simple to compute and it turns out that there are $\frac{1}{6}(n+1)(n+2)(n+3)$ nodes required per element (14). The use of higher order elements generally produces a more accurate solution with larger elements and fewer nodes than decreasing the mesh size for the same memory requirement, at the cost of increased computational time due to the increased bandwidth of the matrix (14).

One drawback of the larger elements that can be used with higher order elements is that they cannot model curved surfaces as accurately as smaller elements. In order to address this shortcoming, isoparametric elements (Fig. 2.5d) with curved sides are used (14). An element with curved faces in xyz-space can be transformed into an element with straight faces in another coordinate system. The order of the transformation, and therefore the conformity to the curved edges of the geometry, is limited by the element order. A second order element may have straight edges or edges with a quadratic curve, while a third order element may have straight, quadratic, or cubic edges.

2.5.2 Basis Functions

The second step of the finite element method is to choose a set of basis functions which will be used to approximate the solution to the differential equation within each element. To confuse matters, the basis functions are also referred to as "elements". Each basis function is required to have a value of 1 at the node with which it is associated, and zero at all other nodes. The most commonly used basis functions are the nth order Lagrange polynomials on the barycentric coordinates (14)

$$l_j^n(\lambda_i) \equiv \prod_{m=0}^{j-1} \frac{n\lambda_i - m}{j - m} \tag{2.85}$$

within the mesh element, and 0 outside. This has the advantage of being 1 when $n\lambda_i = j$ and 0 for any other integer values of $n\lambda_i$ (all other nodes), as well as being polynomial, and therefore differentiable. Products of the Lagrange polynomials can then be combined to create the basis functions. For example, on a triangular element the basis function for the kth node is given by

$$N_k^n(\lambda_1, \lambda_2, \lambda_3) = l_{\Lambda_1}^n(\lambda_1) l_{\Lambda_2}^n(\lambda_2) l_{\Lambda_3}^n(\lambda_3) \tag{2.86}$$

where Λ_i is n times the ith area coordinate of the kth node. It's immediately clear from the definitions of the l_j^n that N_k^n equals 1 when $n\lambda_i = \Lambda_i$, which only occurs at the kth node, and 0 for any other integer $n\lambda_i$. The second order basis function for a node with $\Lambda_1 = 1$, $\Lambda_2 = 1$, and $\Lambda_3 = 0$ is therefore given by

$$N_k^2(\lambda_1, \lambda_2, \lambda_3) = l_1^2(\lambda_1) l_1^2(\lambda_2) l_0^2(\lambda_3). \tag{2.87}$$

If there are no terms in the product in equation 2.85, it is defined to be 1, therefore this expression simplifies to

$$N_k^2(\lambda_1, \lambda_2, \lambda_3) = (2\lambda_1)(2\lambda_2) = 4\lambda_1\lambda_2. \tag{2.88}$$

Since at the node, $\lambda_1, \lambda_2 = 0.5$, this clearly satisfies the requirement to equal 1 at the node, and since at least one of λ_1 or λ_2 must be 0 at all other nodes, this function satisfies that requirement as well. The basis functions for the remaining nodes can be computed similarly, using the appropriate values of Λ_i. Unfortunately for many electromagnetic applications, this formulation does not guarantee the continuity of the derivatives of the potential at the edges, which can result in the violation of the divergence conditions (Eq. 2.1 and 2.3) at the boundaries between elements which can result in non-physical solutions (14).

To address the shortcomings of elements defined in terms of node points (as above), vector elements can be used instead (14). Each basis function is defined to have a tangential component only along one edge, and none along all other edges of the mesh element. They can be zeroth order, where the tangential component of the field is

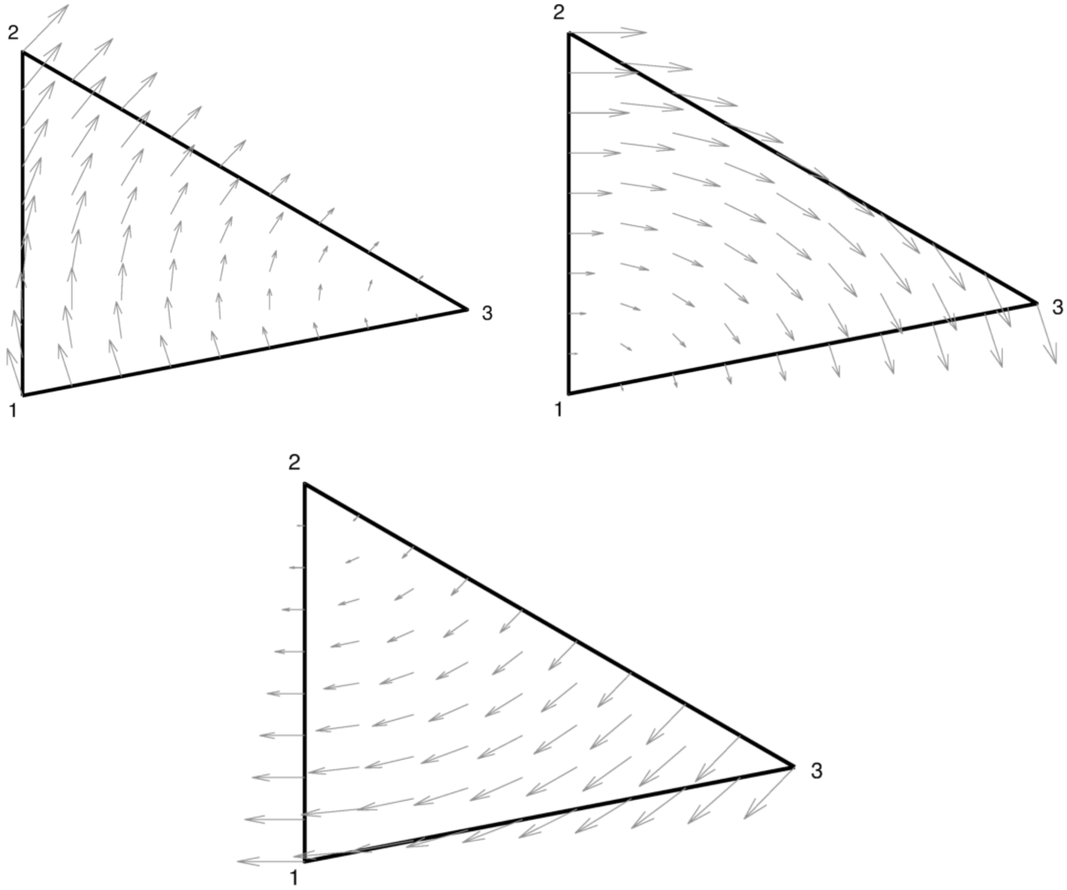

Figure 2.9: The vector element associated with edge 1,2 (a) on a triangle is given by $W_{12} = \lambda_1 \nabla\lambda_2 - \lambda_2 \nabla\lambda_1$. The divergence criterion (equations 2.1 and 2.3 in the absence of sources) is automatically satisfied since $\nabla \cdot W_{12} = \nabla \cdot (\lambda_1 \nabla\lambda_2) - \nabla \cdot (\lambda_2 \nabla\lambda_1) = 0$. Furthermore, since $\lambda_1 = 0$ along edge 2,3, the first term of W_{12} vanishes, and the second term must be perpendicular to the edge, meaning W_{12} must be perpendicular to the edge. Similarly, $\lambda_2 = 0$ along edge 3,1 means that W_{12} is perpendicular to that edge as well. Therefore, the tangential component of W_{12} is 0 along each of the other edges. Finally, because λ_1 and λ_2 vary linearly from 0 to 1 (or 1 to 0) along edge 1,2, the tangential components of their gradients must be constant, opposite, and equal in magnitude along edge 1,2. Thus, defining e to be a vector parallel to edge 1,2 gives $e \cdot W_{12} = \lambda_1 c + \lambda_2 c = (\lambda_1 + \lambda_2)c$, and since $\lambda_1 + \lambda_2 = 1$ along edge 1,2, the tangential component along edge 1,2 must be constant, $e \cdot W_{12} = c$. Because the magnitude varies linearly in the direction perpendicular to edge 1,2, this is known as a first-order vector basis function for this edge. Similar constructions yield the basis functions for the remaining edges: $W_{23} = \lambda_2 \nabla\lambda_3 - \lambda_3 \nabla\lambda_2$ for edge 2,3 (b) and $W_{31} = \lambda_3 \nabla\lambda_1 - \lambda_1 \nabla\lambda_3$ for edge 3,1 (c). Note that these are un-normalized, and require a normalization factor equal to the length of the associated edge to create unitless basis functions with value 1 along the edge.

constant along the edge, or higher order, where the tangential field can vary across the edge. Because the tangential component of the field is defined along the edge, continuity is maintained across edges element edges, which prevents the non-physical solutions that can arise with node based elements. A comprehensive treatment of vector elements can be found in chapter 8 of Jin (14).

2.5.3 Equation Assembly

2.5.3.1 Elemental Equations

After appropriate basis functions have been chosen, the solution to the differential equation (equation 2.27 or 2.28, in this case) must be approximated over each mesh element. This is done by creating an elemental equation, which will then be combined with the other elemental equations to form the global matrix equation (14). This is done using Galerkin's method. Given an arbitrary linear differential equation

$$\mathcal{L}[\phi] - f = 0, \tag{2.89}$$

assume that $\tilde{\phi} = \sum u_i \phi_i$ is an approximate solution to ϕ made up of a set of orthonormal basis functions ϕ_i. The best solution is one that minimizes the residual

$$r = \mathcal{L}[\tilde{\phi}] - f. \tag{2.90}$$

Galerkin's method is a special case of a group of methods known as weighted residual methods (14). They seek to minimize the residual through the use of weighting functions, w_i and setting the inner product of the weighting function and the residual to zero

$$\langle w_i, r \rangle = \int w_i r \, \mathrm{d}\Omega = 0. \tag{2.91}$$

In Galerkin's method, the weighting functions are taken to be the basis functions themselves, that is: $w_i = \phi_i$ (14). This results in the equation

$$\langle \phi_i, r\rangle = \langle \phi_i, \mathcal{L}[\tilde{\phi}] - f\rangle = \langle \phi_i, \mathcal{L}[\tilde{\phi}]\rangle - \langle \phi_i, f\rangle = 0. \tag{2.92}$$

But since $\tilde{\phi} = \sum u_i \phi_i$, the $\langle \phi_i, \mathcal{L}[\tilde{\phi}]\rangle$ term can be rewritten, exploiting the linearity of the operator $\mathcal{L}$, to get

$$\langle \phi_i, \mathcal{L}[\tilde{\phi}]\rangle = \langle \phi_i, \sum_j \mathcal{L}[u_j \phi_j]\rangle = \sum_j u_j \langle \phi_i, \mathcal{L}[\phi_j]\rangle. \tag{2.93}$$

A definition of $L_{i,j} \equiv \langle \phi_i, \mathcal{L}[\phi_j]\rangle$ and $f_i \equiv \langle \phi_i, f\rangle$, allows equation 2.92 to be reduced to the simple set of linear equations

$$\sum_j L_{i,j} u_j - f_i = 0 \tag{2.94}$$

or in matrix form

$$\mathbb{L}\mathbf{u} - \mathbf{f} = 0. \tag{2.95}$$

2.5.3.2 Matrix Assembly

Once equation 2.95 has been determined for each element, the elemental matrices must be assembled into a global matrix representing the entire problem. This is a relatively straightforward process. Beginning with an $N_n \times N_n$, zero filled matrix $\mathbb{K}$, where N_n is the number of nodes in the problem, iterate through all of the matrix entries for each element, $L^e_{i,j}$. Accumulate each value from each $\mathbb{L}$ at the corresponding location in $\mathbb{K}$ using the $\mathbb{T}$-matrix

$$K_{T_{e,i},T_{e,j}} = \overline{K_{T_{e,i},T_{e,j}}} + L^e_{i,j} \tag{2.96}$$

where $\overline{K_{T_{e,i},T_{e,j}}}$ represents the previous value of $K_{T_{e,i},T_{e,j}}$. The source vector, **f** can similarly be accumulated to a global source vector, **F**

$$F_{T_{e,i}} = \overline{F_{T_{e,i}}} + f^e_i. \tag{2.97}$$

This results in a global matrix equation for the entire domain

$$\mathbb{K}\mathbf{u} - \mathbf{F} = 0. \qquad (2.98)$$

In the homogeneous case, $\mathbf{F} = 0$, and $\mathbb{K}$ can be written as $\mathbb{A} - \boldsymbol{\lambda}\mathbb{B}$. Equation 2.98 then reduces to the eigenvalue problem

$$\mathbb{A}\mathbf{u} = \boldsymbol{\lambda}\mathbb{B}\mathbf{u}. \qquad (2.99)$$

2.5.4 Solution

Equations 2.98 and 2.99 are large, sparse matrices. There are many algorithms for solving such matrix equations which have been developed since the 1940s and 50s. In particular, this work uses a solver called PARDISO (Parallel Sparse Direct Solver) (16) as implemented in COMSOL Multiphysics (Burlington, Massachusetts, USA). This is a fast, memory efficient, and robust solver that is parallelized to speed computation, and can be run iteratively to greatly increase memory efficiency, at some speed cost.

2.6 Particle-in-Cell Model

Modelling the acceleration of the electron beam accurately requires combining two effects. First, the effect of the RF fields within the waveguide as they accelerate the electrons (external fields), and second, the effect of the fields generated by the electron beam itself (space-charge). While this is theoretically straightforward, in practice it is very difficult. While the external fields are pre-calculated in the simulations presented in this work, and therefore computationally inexpensive, the space-charge fields depend on and affect all the particles in the beam, and are therefore computationally very expensive. Because the external RF fields are quickly varying, in order for their effects to be accurate small time steps are required, which would result in extremely long computation times if calculation of the space-charge fields is required at each time step. The model most commonly used in particle accelerator simulations is known as the particle-in-cell

(PIC) model. PIC is popular for this application because it allows the separation of the external fields and space-charge effects.

2.6.1 Hamiltonian Mechanics

The Hamiltonian of a system is defined simply to be the total energy (sum of potential and kinetic energy) of the system, written as a function of the momentum and position of the particles within the system. It is a convenient formalism for many problems, as it allows (time derivatives of) the moment and position variables to be written as the derivative of the Hamiltonian with respect to the position and moment variables, respectively. If $\mathbf{p}$ is the momentum vector and $\mathbf{q}$ is the position vector for all the objects in the system (high dimensional vectors, containing all the components of momentum/position for all the objects in the system) and $H(\mathbf{p},\mathbf{q},t)$ is the Hamiltonian (total energy), then Hamilton's equations are (17)

$$\frac{\mathrm{d}\mathbf{p}}{\mathrm{d}t} = -\frac{\partial H(\mathbf{p},\mathbf{q},t)}{\partial \mathbf{q}} \tag{2.100}$$

$$\frac{\mathrm{d}\mathbf{q}}{\mathrm{d}t} = \frac{\partial H(\mathbf{p},\mathbf{q},t)}{\partial \mathbf{p}}. \tag{2.101}$$

While it is usually more convenient to work directly from Newton's law, $\frac{\mathrm{dp}}{\mathrm{d}t} = \mathbf{F}$, in some special cases it is more convenient to work from Hamilton's equations. This is sometimes the case in the derivation of a computational model, which means that conditions on the applicability of such a model are often conditions on the form of the Hamiltonian of the system, as is the case for the PIC model.

2.6.2 External Fields

The force on electrons due to the external fields is the relativistic Lorentz force (1)

$$\frac{\mathrm{d}P^{\mu}}{\mathrm{d}t_0} = qF^{\mu\nu}U_{\nu} \tag{2.102}$$

where **P** is the relativistic 4-momentum, t_0 is the proper time of the electron, and **F** is the Faraday tensor, and **U** is the covariant form of the 4-velocity. In a given coordinate frame, these can be written as

$$U_{\mu} \rightarrow \begin{bmatrix} \gamma c \\ -\gamma v_x \\ -\gamma v_y \\ -\gamma v_z \end{bmatrix} \tag{2.103}$$

$$P^{\mu} \rightarrow \begin{bmatrix} \gamma mc \\ \gamma m v_x \\ \gamma m v_y \\ \gamma m v_z \end{bmatrix} \tag{2.104}$$

$$F^{\mu\nu} \rightarrow \begin{bmatrix} 0 & -\frac{E_x}{c} & -\frac{E_y}{c} & -\frac{E_z}{c} \\ \frac{E_x}{c} & 0 & -B_z & B_y \\ \frac{E_y}{c} & B_z & 0 & -B_x \\ \frac{E_z}{c} & -B_y & B_x & 0 \end{bmatrix}. \tag{2.105}$$

The Hamiltonian of this system is given by (18)

$$H = \sqrt{(c\mathbf{P} - e\mathbf{A})^2 + m^2c^4} + e\Phi \tag{2.106}$$

where **A** is the magnetic vector potential and Φ is the scalar electric potential. As the external fields have been precomputed, the derivatives of equations 2.100 and 2.101 are simple to compute to update the position and momentum at each time step.

2.6.3 Space-Charge Fields

The space-charge fields are significantly more difficult to compute. Because it is not feasible to model a realistic number of electrons (10^{12} to 10^{14} per bunch), each simulated (macro)particle represents many thousands or millions of real particles. The particles are therefore deposited onto a grid by approximating each particle as a constant density cube that can contribute mass to several points on the grid (known as a cloud-in-cell method) to get a charge density, and Green's function is used to determine the potential Φ (19)

$$\Phi_{p,q,r} = \sum G_{p-p',q-q',r-r'} \rho_{p',q',r'} \tag{2.107}$$

where G is the Green's function on the grid with open boundary conditions, and ρ is the charge density on the grid. The cloud-in-cell method is again used to interpolate the fields back onto the position of the particles. The grid is moving with, and centered on a reference particle that is chosen at the beginning of the computation. If the reference particle leaves the region of interest, another particle is selected to be the reference particle, and the computation continues. The cloud-in-cell approximation assumes that the particles are stationary with respect to the reference particle, and the effect of the motion of the electrons is captured by the motion of the space-charge grid with the reference particle. It is therefore very important to position the reference particle carefully so that it remains near the center of an electron bunch, and the motion of the remaining electrons with respect to the reference particle is minimized. The Hamiltonian of a stationary electron in an electric field is simply given by $H = e\Phi$, which can be used with Hamilton's equation 2.100 to update the electron's momentum (the kinetic energy term, which depends on the momentum and would therefore be used to update the position in equation 2.101, is already included in the external-field Hamiltonian, equation 2.106).

2.6.4 Split Operator Method

For a given Hamiltonian, H, a mapping, M, can be defined that converts the initial phase space coordinates, x_i, onto the final phase space coordinates, x_f.

$$x_f = M[x_i]. \tag{2.108}$$

The mapping can be written as a function of the time step, τ, such that it maps the phase space coordinates at time t, $x(t)$, onto the phase space coordinates at a time τ later, $x(t+\tau)$

$$x(t+\tau) = M(\tau)[x(t)]. \tag{2.109}$$

If the Hamiltonian can be written as the sum of two parts

$$H = H_1 + H_2 \tag{2.110}$$

each of which can be calculated to the desired accuracy, then split operator methods can be used to apply the mapping corresponding to each Hamiltonian separately (19). In other words, if M_1 is the mapping corresponding to H_1, and M_2 is the mapping corresponding to H_2, then instead of computing equation 3.2 directly for M, M_1 can be computed for half of a time step, followed by M_2 for a whole time step, and then M_1 for another half time step:

$$M(\tau) \approx M_1(\tau/2)M_2(\tau)M_1(\tau/2) \tag{2.111}$$

which is accurate to order τ^2 (19). Furthermore, if one of the maps varies significantly faster than the other (say M_1), then it can be further broken up into smaller time steps, allowing for more accurate modelling of one force, while allowing the more slowly changing force to be computed less frequently:

$$M(\tau) \approx M_1(\tau/4)M_1(\tau/4)M_2(\tau)M_1(\tau/4)M_1(\tau/4). \tag{2.112}$$

This allows huge gains in computation cost if M_2 is computationally expensive, but changes more slowly.

2.6.5 Application

If M_1 is the change in momentum due to the external fields, and M_2 the change in momentum due to the space-charge effects, then each can be propagated through the time step τ using equation 2.112. First, the distribution of particles is propagated through a time step $\tau/2$ (or multiple smaller time steps totaling $\tau/2$) under the influence solely of the external fields. Next, Poisson's equation (2.1) is solved using the position of the electrons after the half time step, and provide a 'kick' to the momentum of the electrons. Following the space-charge 'kick', the electron beam is propagated through the remaining $\tau/2$ under the influence of the external fields, beginning with the adjusted momenta.

Doing this allows τ to be chosen sufficiently large that the space-charge effects are computed as little as possible (as this is the most computationally expensive step), while the effects of the external fields are computed on a much smaller time step to accurately model the effects of the rapidly varying RF fields. Since space charge fields depend only on the position of the particles, from Hamilton's equations, (2.100 and 2.101), they can only affect the momentum. The change in momentum due to the space-charge fields can therefore be calculated over the entire time step τ and apply it as an instantaneous change, while updating the position during the two half steps under the influence of the external fields, which depends on both momentum (explicitly) and position (implicitly, in the RF fields). This is similar to the condensed history methods (Section 2.7.1.3) used in Monte Carlo simulations. In condensed history methods, computationally expensive scattering events are computed once or a few times per step (as in the momentum change due to space-charge), while the computationally inexpensive energy deposition along the track is computed multiple times, or continuously (as in the electron acceleration due to the external fields). In both condensed history and PIC simulations, the aim is to reduce the frequency of computationally expensive interactions without losing accuracy.

2.6.6 Beam Loading

As the electron beam traverses the waveguide, some energy is absorbed from the RF fields, meaning less is available for trailing electrons. This is realized through the electric and magnetic fields generated by the leading electrons (which can in turn reflect off of the cavity walls), and their effect on trailing electrons, and is known as beam loading. In order to calculate the external field effects on the electrons, the external fields are interpolated onto a grid encompassing the central beam tube of the waveguide, and imported into PARMELA in this form. Because the fields and cavity geometry outside the central region of the waveguide are not available, a complete modelling of beam loading is impossible. Instead, PARMELA takes into account only first order effects (the direct interactions between particles) and neglects higher order effects (interactions between particles that are first mediated by the cavity walls). A comprehensive treatment of beam loading can be found in Wanger (3).

2.7 Monte Carlo

Monte Carlo simulations refer very generally to a class of simulation algorithms that depend on random numbers. They are capable of accurately modelling both deterministic (non-random) problems for which there are no other methods of solution, as well as problems which inherently involve randomness or probabilistic outcomes. In this work, the Monte Carlo code EGSnrc (National Science and Research Council of Canada, Ottawa) (20) is used to model the radiation transport, beginning with the electron beam exiting the waveguide striking the x-ray target (produced by PARMELA), and ending when all of the particle energy is deposited as dose in the simulated water phantom. A simulation begins with one or more particles, along with positions and momenta for each particle, on the “stack”, and three steps are repeated until no particles remain:

1. A particle is taken from the stack and propagated through space.
2. The particle undergoes an interaction.
3. New particles (if any) are added to the stack.

Data, such as energy deposition or particle fluence, may be recorded during each of these steps as required.

2.7.1 Basics

2.7.1.1 Random Sampling

A discussion of Monte Carlo radiation transport simulation must begin with an understanding of the random sampling technique used. A particular particle interaction, such as Compton scattering, will occur according to a differential cross section (DCS), which forms a probability density function (PDF) (Fig. 2.11). EGSnrc uses a combination of direct and rejection sampling method to choose a value from the PDF (21), $f(x)$. Direct sampling is more efficient when the PDF can be integrated and inverted analytically (Fig. 2.10).

In some cases it is impossible to integrate or invert the PDF analytically, and doing this numerically can add error to the distribution. In these cases, EGSnrc uses rejection

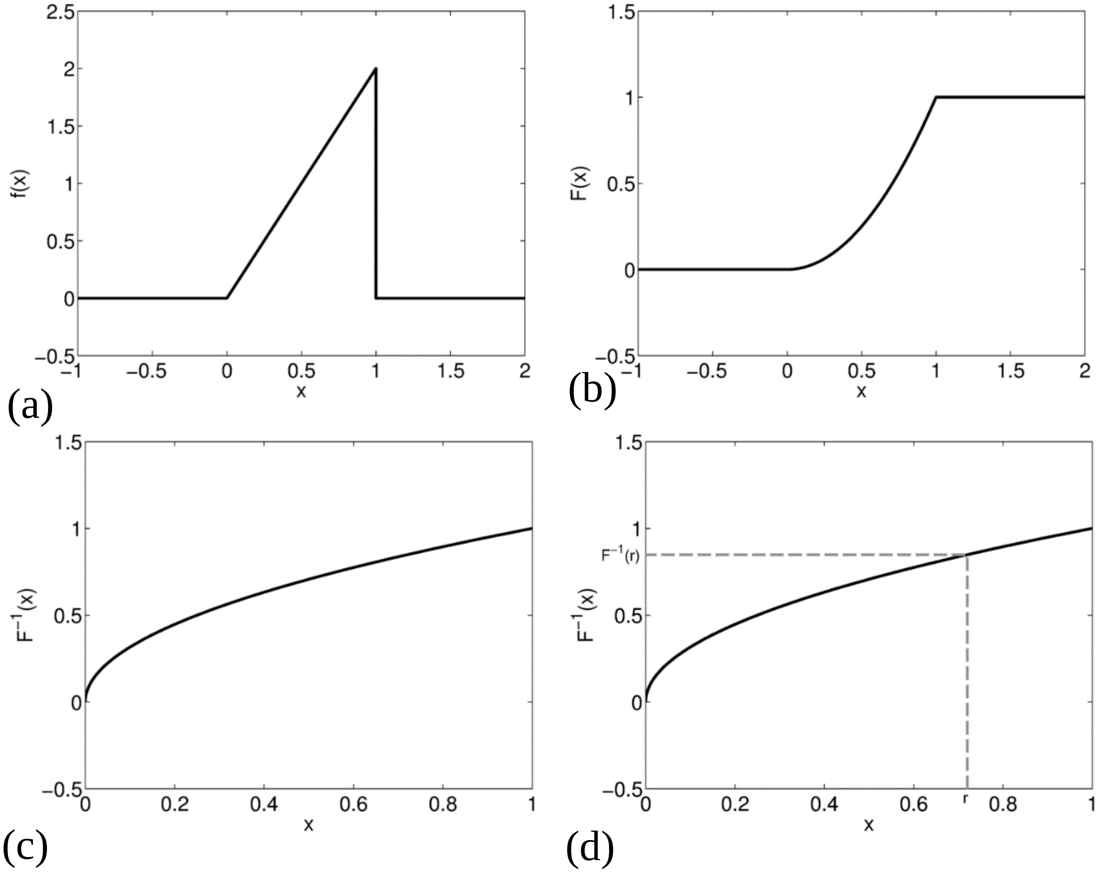

Figure 2.10: Direct sampling from a PDF: (a) A normalized, simple PDF, $f(x) = 2x$ for $x \in [0,1)$ and $f(x) = 0$ otherwise, is integrated to form (b) the cumulative distribution function (CDF), $F(x) = \int_{-x_{\mathrm{min}}}^{x} f(x')\mathrm{d}x' / \int_{-x_{\mathrm{min}}}^{x_{\mathrm{max}}} f(x')\mathrm{d}x'$. If the PDF is normalized, $F(x)$ will increase monotonically from 0 to 1. This can then be inverted to get (c), $F^{-1}(x)$, which has a domain of the unit interval. A random number r is generated from the uniform distribution between 0 and 1, and the number $F^{-1}(r)$ is the random number from the PDF.

sampling. In general, rejection sampling also involves 4 main steps, though 3 steps may need to be repeated several times:

1. A sampling PDF, $g(x)$, is created. This PDF is simpler than $f(x)$, and can be sampled directly. The only requirement on selection of $g(x)$ is that the ratio $f(x)/g(x)$ be bounded by some constant M ($f(x)/g(x) \leq M \ \forall x$).
2. A random number, r_1, is generated from $g(x)$.

3. A second random number, r_2, is generated from the uniform distribution between 0 and 1.
4. If $r_2 < f(r_1)/Mg(r_1)$, then r_1 is kept, otherwise return to step 2.

If $f(x)$ and its range are both already bounded (as is the case for all radiation interactions to be simulated), then $g(x)$ can simply be taken to be a uniform distribution over the same range. However, if $g(x)$ is chosen to more closely approximate $f(x)$ (ie. $f(x)/Mg(x) \approx 1$), fewer iterations are required before a random number is accepted.

2.7.1.2 Photon Transport

The distance travelled by a photon before an interaction in EGSnrc is determined by the well-known Beer-Lambert-Bouguer law (often referred to as simply Beer's law, or the Beer-Lambert law, but originally discovered by Pierre Bouguer)

$$f(x) = e^{-\mu x} \text{ (for } x \geq 0) \tag{2.113}$$

where μ is the linear attenuation coefficient of the material. As this PDF is trivial to integrate and invert analytically, it is sampled directly using

$$F^{-1}(x) = -\frac{1}{\mu}\ln(1 - \mu x). \tag{2.114}$$

A random number, r, is generated between 0 and 1, and the photon travels a straight line a distance $F^{-1}(r)$.

An interaction type is selected based on the total interaction cross-sections out of: Rayleigh scattering, photoelectric absorption, Compton scattering, pair production and triplet production (Fig. 2.12). The total interaction cross-section for each interaction type represents the overall probability of that interaction occurring. It is found by integrating the PDF over all possible outcomes (deflection angles, energy losses, and/or secondary

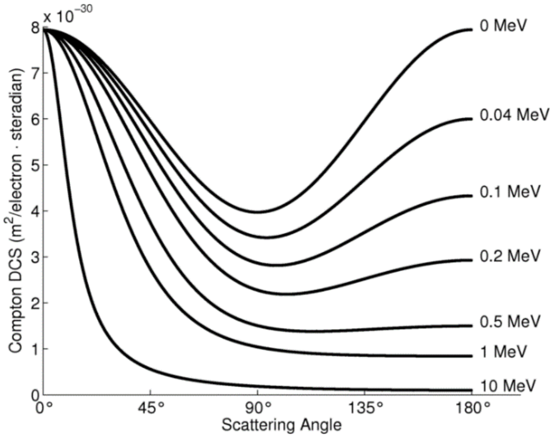

Figure 2.11: The angular differential cross-section for Compton scattering for a selection of photon energies. Higher energy photons are more likely to be forward scattered (low scattering angle).

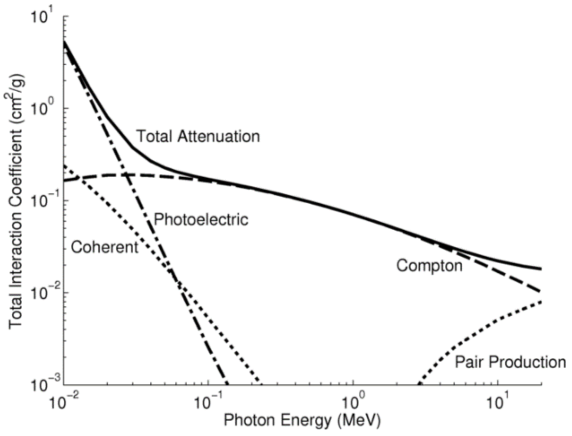

Figure 2.12: The total scattering cross section as a function of energy. Each component is added linearly to get the linear attenuation coefficient (μ in Eq. 2.113) which is used to determine the path length. The magnitudes of the cross sections for each interaction relative to the linear attenuation coefficient type represent the probability of that interaction type being selected.

particles produced). After the interaction, if the photon energy is below the cutoff energy, it is discarded. Otherwise it's position and momentum are updated based on the differential cross-section of the interaction selected, and it is added to the stack, along with any secondary particles produced by the interaction.

2.7.1.3 Electron Transport

Charged particles undergo interactions far more frequently than photons, making it impractical to simulate each interaction individually. However, most interactions result in relatively small changes in direction or energy. As such, most Monte Carlo simulations of electrons use a condensed-history approach to electron transport, where multiple small interactions are accumulated until a larger, catastrophic interaction occurs. User set thresholds for inelastic collisions producing secondary electrons (T_c) and for bremsstrahlung photons (k_c) are used to determine whether an interaction is considered catastrophic. Sub-threshold interactions are approximated using the continuously slowing down approximation (CSDA) and the energy lost is considered to be deposited locally in a small region about the electron track. At the site of the catastrophic interaction, the effects of the sub-threshold interactions can be accounted for using multiple scattering theory (22).

In EGSnrc, the condensed history technique used is known as PRESTA-II. In this technique, the energy of the electron at the next catastrophic collision is determined by sampling a PDF representing multiple scattering types. The scattering angle is sampled using multiple scattering theory twice for each catastrophic interaction (23). The two scattering angles are added vectorially assuming each represents half of the total step, and the electron position and angle are updated before the catastrophic interaction (23). This results in an electron transport algorithm that is largely step-size independent, as long as the electron is travelling through a uniform medium. However, the requirement of two angular samplings for each step can be computationally expensive, particularly if the cutoff thresholds are low.

Multiple scattering theory requires that all the sub-threshold scattering events occur in a single medium. Because of this, condensed history methods cannot be used at boundaries between different media. When an electron approaches a boundary, EGSnrc switches to model single elastic scattering events, instead of a condensed history approach.

2.7.2 Variance Reduction

For Monte Carlo simulations, the goal is to get as accurate an answer as possible. One method of increasing the accuracy of a solution is to simulate more particles. This results in a linear increase in computation time with the number of particles, N. Since statistical uncertainty is proportional to $1/\sqrt{N}$, this results in diminishing returns for large numbers of particles. A class of techniques known as variance-reduction techniques are employed to improve the accuracy of the solution without requiring more particles to be fully simulated. Generally, variance reduction involves one (or more) of three techniques: 1. discarding particles which are not relevant to the desired solution (so computational resources are not wasted on irrelevant simulations), 2. adding extra particles in the regions of interest (to improve statistical accuracy without simulating additional initial particles), or 3. biasing the DCS of the interactions in order that the particles are preferentially directed towards the region of interest (to accomplish both of the above objectives) (24).

In this work, the EGSnrc directional bremsstrahlung splitting is used for variance reduction, which uses a combination of techniques 1 and 2 above. First, for every bremsstrahlung photon that would be generated, 100 photons are generated instead (this number is user configurable) and each photon is given a weighting of 1/100. A region of interest is defined, and all photons directed outside the region are subject to elimination through a Russian Roulette process, of which 1/100 survive. The Russian roulette process involves selecting a random number between 0 and 1, and then discarding the particle if the random number is less than 0.99. Those that survive are given a weighting of 1 (fat photons). This allows 100 times as many bremsstrahlung photons to be created in the region of interest (each with weight 1/100), while only 1 times as many photons are created outside the region of interest (each with weight 1), saving computational resources on photons that likely won’t contribute much to the final result.

If a “light” photon (weight 1/100 or lower) undergoes a Compton interaction (except in air) Russian roulette is played on the photon, and if it survives, it becomes a “fat” photon (weight ×100). A fat electron is generated, and if the photon is scattered outside the field of interest, Russian roulette is again played. The fat electron is split into 100 light electrons, and Russian roulette is played on any electrons directed out of the region of interest (23).

2.8 References

1. Griffiths DJ. Introduction to Electrodynamics. Prentice Hall; 1999.
2. Hoppe DJ. Impedance Boundary Conditions In Electromagnetics. 1st ed. CRC Press; 1995. 262 p.
3. Wangler TP. Rf Linear Accelerators. Wiley-VCH; 2008. 476 p.
4. Nagle DE, Knapp EA, Knapp BC. Coupled Resonator Model for Standing Wave Accelerator Tanks. Rev Sci Instrum. 2004 Dec 29;38(11):1583–7.
5. Agarwal A, Lang J. Foundations of Analog and Digital Electronic Circuits. 1 edition. Amsterdam ; Boston: Morgan Kaufmann; 2005. 1008 p.
6. Wang JW. RF properties of periodic accelerating structures for linear colliders. SLAC-Report-339; 1989.
7. Wang J, Loew G. Field emission and rf breakdown in high-gradient room-temperature linac structures. SLAC-PUB-7684; 1997.
8. Tanabe E, Wang J, Loew G. Voltage Breakdown at X-band and C-band Frequencies. In: Linear Accelerator Conference Proceedings. 1986. p. 458–460.
9. Kilpatrick WD. Criterion for Vacuum Sparking Designed to Include Both rf and dc. Rev Sci Instrum. 1957 Oct;28(10):824–6.
10. Baillie D, Aubin JS, Fallone BG, Steciw S. Feasibility of producing a short, high energy s-band linear accelerator using a klystron power source. Med Phys. 2013;40(4):41713.
11. Loew GA, Wang JW. Field emission and rf breakdown in copper linac structures. Part Accel. 1989;30(SLAC-PUB-5059):225–230.

12. Dolgashev V, Tantawi S, Higashi Y, Spataro B. Geometric dependence of radio-frequency breakdown in normal conducting accelerating structures. Appl Phys Lett. 2010;97:171501.

13. Tanabe E. Voltage Breakdown in S-Band Linear Accelerator Cavities. IEEE Trans Nucl Sci. 1983 Aug;30(4):3551–3.

14. Jin J. The Finite Element Method in Electromagnetics. Wiley; 1993.

15. Boris N. Delaunay,(1934)"Sur la Sphere" Vide. Izv Akad Nauk SSSR. :793–800.

16. Schenk O, Gärtner K. Solving unsymmetric sparse systems of linear equations with PARDISO. Future Gener Comput Syst. 2004 Apr 1;20(3):475–87.

17. Hand LN, Finch JD. Analytical Mechanics. 1 edition. Cambridge ; New York: Cambridge University Press; 1998. 592 p.

18. Jackson JD. Classical Electrodynamics. Wiley; 1999.

19. Young LM BJH. Parmela. LA-UR-96-1835, Rev; 2005.

20. Kawrakow I, Rogers DWO. The EGSnrc code system. NRC Rep PIRS-701 NRC Ott. 2000;

21. Nelson WR, Hirayama H, Rogers DW. EGS4 code system. Stanford Linear Accelerator Center, Menlo Park, CA (USA); 1985.

22. Lewis HW. Multiple scattering in an infinite medium. Phys Rev. 1950;78(5):526.

23. Kawrakow I. Accurate condensed history Monte Carlo simulation of electron transport. I. EGSnrc, the new EGS4 version. Med Phys. 2000;27(3):485–498.

24. Bielajew AF, Rogers DWO. Variance-Reduction Techniques. In: Jenkins TM, Nelson WR, Rindi A, editors. Monte Carlo Transport of Electrons and Photons. Springer US; 1988. p. 407–19. (Ettore Majorana International Science Series).

3. Feasibility

A version of this chapter has been published. Devin Baillie, J. St. Aubin, B. G. Fallone, S. Steciw, "Feasibility of producing a short, high energy s-band linear accelerator using a klystron power source," Medical Physics 40 (4) 041713 (2013)

3.1 Introduction

Prior to attempting the full design of a new 10 MV waveguide, a study was conducted to determine whether it is feasible to get 10 MV x-rays from a 27.5 cm waveguide. Maintaining a length of 27.5 cm, the length of the currently used Varian 600C s-band waveguide, is desired in order to be compatible with the existing linac-MR design being developed at the Cross Cancer Institute without any modifications. There are two possible methods for achieving a high-energy linac without increasing its length: (1) Increase the operating frequency from s-band to c-band or x-band (or higher). (2) Increase the field strength in the s-band accelerator. Although the higher frequency used for C and X band linacs allows for higher power densities within the waveguide, and therefore shorter waveguide length for the same x-ray energy, they also require tighter mechanical tolerances (for both the waveguide and RF power source), which results in unstable output (1) and costlier construction when compared with S-band linacs. Therefore the research outlined in this chapter investigates the feasibility of the second method, of increasing the field strength in the s-band accelerator.

A significant concern when increasing the input power for a waveguide is electric breakdown. As explained in more detail in section 2.4, if the RF fields in the waveguide increase beyond some threshold determined by the waveguide geometry and operating frequency, electric arcing will occur within the waveguide, absorbing the RF energy and damaging the waveguide (2). Because of the lack of facilities to experimentally test for breakdown, calculated fields are compared against published experimental results for comparable frequency ranges. Wang and Loew (3) published a "conservative fit" for existing experimental results on the peak surface field achievable before breakdown occurs, as a function of operating frequency (previously equation 2.68 in section 2.4)

$$E = 220\ \mathrm{MV/m}[f/1\ \mathrm{GHz}]^{1/3}. \tag{3.1}$$

Using the operating frequency of 2.9985 GHz gives a breakdown threshold of 317 MV/m.

This feasibility study adapts existing simulations to investigate the feasibility of producing photon energies up to 10 MV in a short waveguide without breakdown. Previously, a finite element method (FEM) simulation emulating a Varian 600C (6 MV) waveguide was developed by Dr. St. Aubin et al. (4,5). By increasing the input power in the Varian 600C simulation until 10 MV photons are produced, and comparing to equation 3.1 it can be determined whether breakdown will be an issue.3.*1*3.*1*3.*1*

3.2 Methods

In order to investigate the effects of increasing the power input into the waveguide on breakdown and beam characteristics, previously simulated and benchmarked FEM model of a single energy Varian 600C (6 MV) waveguide was used (4,5). Dr. St. Aubin et al. previously used FEM software COMSOL Multiphysics v. 3.5a (Burlington, Massachusetts, USA) to adjust the resonant frequency of the model and calculate the 3D RF fields within. The final field solution is calculated using the PARDISO solver, in a harmonic propagation analysis with the default settings. The conductive exterior of the waveguide is modeled using the impedance boundary conditions provided by COMSOL with a conductivity of 58.58 MS/m. The RF power is transmitted to the waveguide through a 6.95 cm length of 3.4 × 7.2 cm transmission waveguide terminating 4.0 cm from the central axis of the accelerating waveguide, and coupled into the waveguide through a 2.35 × 1.71 cm coupling port in the fourth accelerating cavity. The mesh consists of 391 594 isoparametric elements using cubic shape functions, a minimum element quality of 0.0817, with an element volume ratio of 6.11×10^{-6}. Refining the mesh further has no effect on the field solution.

The electron gun was simulated using the 3D FEM software Opera-3D/SCALA (Kidlington, UK) with a cathode potential of 30.8 kV and a beam current of 361 mA at the anode (6). The electron phase space from the Opera-3D/SCALA model, along with the interpolated RF fields calculated in COMSOL, were input into an electron tracking software PARMELA (Los Alamos National Laboratory, NM) (4,5,7). PARMELA calculated the electron trajectories within the 3D RF fields, including space charge and beam loading effects, and produces an electron phase space exiting the waveguide, and incident on the target. This existing model is used as the basis of the work in this chapter, where details of the geometry and the simulation settings are published in the previous studies (4,5).

The Varian 600C, against which this model was benchmarked, is powered by a 2.5 MW magnetron power source. Power can be increased by a factor of 3 by using a 7.5 MW klystron power source (a magnetron operates with electrons orbiting through resonant cavities due to a permanent magnet in order to generate RF fields, while a klystron amplifies an existing RF field, by using it to create bunching in a DC electron beam and passes the beam through a resonant cavity, converting the DC kinetic energy of the beam into RF fields), which is currently commercially available with an identical operating frequency of 2.9985 GHz (Thales TH-2157). Therefore, the input power in the FEM model was tripled, the geometry and solver settings were otherwise unmodified; and the RF fields were then recalculated using COMSOL. In previous work done by Dr. St. Aubin et al. (4) it was found that the RF fields in the first half accelerating cavity, where the electrons enter the waveguide, are critical for electron capture within the waveguide, and have a strong influence on the final energy spectrum. These fields can be reduced by repositioning the first coupling cavity, and retuning the adjacent accelerating cavities, thereby reducing the power coupled into the first half accelerating cavity. In order to approximate the effect of this modification, the fields in the first half cavity are scaled by factors from 0 to 1, with the remaining fields increased to account for conservation of energy, assuming the power distribution among the remaining cavities remains unchanged. If $E_0^{(i)}$ is the mean axial field in the ith cavity, as defined in section 2.2.2, then the scaling factor, s, for the field strengths in the remaining cavities (in terms of the scaling factor for the first cavity, s_1) is given by

$$s = \sqrt{1 + \frac{(1 - s_1)^2 {E_0^{(1)}}^2}{2 \sum_{i=2}^{6} {E_0^{(i)}}^2}}. \tag{3.2}$$

This feasibility study is based on a model with the first coupling cavity offset by 0.25 mm (5), while additional models with offsets of 0.5 mm and 1.5 mm have been described previously (4). The fields from these additional models are compared with the rescaled fields, to estimate the accuracy of the rescaling. The PARMELA simulations are run again, using the modified fields as input to determine the electron spectra which would be achievable through minor modification to the waveguide. The peak surface fields are extracted and compared to the threshold of 317 MV/m calculated from Eq. 3.1.

The output SCALA phase space contains each macro-particle current, position (x, y, z) and relativistic velocity (v_x, v_y, v_z). This phase space is used as an input into PARMELA (input type 40) which requires each macro-particle's position (x, y) its transverse fractional momentum (p_x, p_y), its energy and its phase in relation to a reference particle set in the center of the beam. The energy is easily computed from the relativistic velocities from SCALA and the macro-particles are randomly distributed over 2 full RF periods (720°). Since each macro-particle in PARMELA is considered to have equal units of charges, the differing currents with each SCALA macro-particle have to be converted to expected input. This is performed in an analogous way as PARMELA converts an ISIS input (7).

The distribution of particles over 2 RF periods creates initial and final half electron bunches which are discarded in post-processing, and only the central electron bunch is kept for analysis. This is done to approximate a steady state solution by removing simulation end effects. Additional testing was done with the particles distributed over 4 and 6 RF periods, with negligible effect on the results obtained from the central electron bunch. To improve statistics, the PARMELA simulation for each field solution is run multiple times, with injected electron distribution randomized each time in phase and azimuthal position (due to azimuthal symmetry of the electron gun) to avoid correlation. The results of the runs are aggregated until at least 45×10^6 particles exiting the waveguide and striking the target are obtained. The energy spectrum, spatial distribution, and beam current of the resulting electron beams exiting the waveguide are calculated.

One of the electron beams was chosen so the width of the electron energy spectrum was comparable to the magnetron powered waveguide. This beam was used for Monte Carlo simulation using BEAMnrc (8). The PARMELA phase space output is nearly identical to the required input for BEAMnrc with the exception of the latch and particle weight. Each electron is given a weight of 1 and its latch was set to indicate that it was an electron which had not interacted previously. The resulting PDDs were compared against measured PDDs for a Varian (Palo Alto, CA) 10 MV photon beam. The measurements were performed using an IBA dosimetry (Bartlett, TN) Blue Phantom water tank with a XX ionization chamber. For simplicity, the Monte Carlo simulations use the same Varian 6 MV linac head model from previous studies (5), with the x-ray target and flattening filter replaced with their Varian 10 MV equivalents. 4×4, 10×10, and 20×20 cm^2 fields were simulated using 100 million histories for the BEAMnrc linac head simulation, and 15 billion histories in DOSXYZnrc to compute the dose in water phantom. Scoring voxel sizes of $5\times5\times1$ mm^3 were used for depths less than 3.5 mm, and $5\times5\times5$ mm^3 for depths greater than 3.5 mm. The penumbra of the 10×10 cm^2 beam was calculated at 10 cm depth using 90 billion histories in DOSXYZnrc with scoring voxel sizes of 0.2 mm (x-direction) × 5 mm (z-direction) × 5 cm (y-direction) across the penumbra. These results were compared with an identical simulation done using the electron beam parameters for a Varian 10 MV linac published by Sheikh-Bagheri and Rogers (9).

The electron gun and waveguide are designed based on measurements and published data (4,5) and the linac head is modeled exactly to Varian specifications (10). The electron gun voltage was -30.8 kV and the electron gun current was 0.36 A. The waveguide has a shunt impedance of 115 MΩ/m ad produces a target current of 134 mA. Although errors propagate from one simulation to the next in an integrated simulation, the errors at each stage were minimized by (1) designing each simulation based on measurements or published data (as much as possible), (2) the generation of a large number of particles to reduce latent variance, and (3) using benchmarked software.

3.3 Results and Discussions

During the initial study of the Varian 600C waveguide, the peak surface fields within the waveguide were calculated to be 124.5 MV/m. As the field magnitudes increase with the square root of the input power, increasing the input power by a factor of three results in peak surface fields of 215.7 MV/m. This result is consistent with the fields calculated without rescaling. At this frequency (2.9985 GHz), these field strengths are more than 30% lower than the threshold determined by Wang and Leow (3). For all

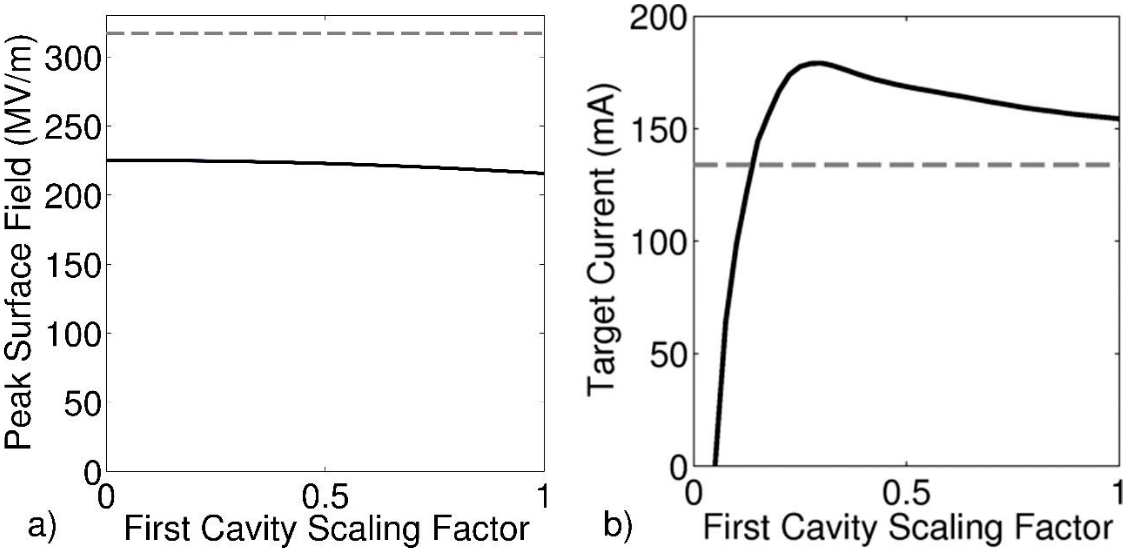

Figure 3.1: (a) The peak surface electric fields within the waveguide (solid line) compared with the threshold for breakdown (dashed line), as the first cavity fields are scaled. (b) The beam current striking the target as the first cavity fields are scaled (solid line) compared with the beam current from the magnetron powered (6 MV) waveguide (dashed line).

first cavity scaling factors, the peak surface fields (Fig. 3.1a) are well below this threshold (shown as a dotted line) and therefore electric breakdown is not expected to interfere with the operation of the accelerator. In particular, with a scaling factor of 0.475, the peak surface fields are 223.1 MV/m, still 29% below the threshold.

Field amplitudes from the field-scaling approach used in this study showed good agreement with field solutions from earlier waveguide models (4,5) (incorporating first coupling cavity offsets of 0.5 mm and 1.5 mm). The axial electric fields along the entire central axis have an RMS error of 0.43 MV/m and 0.56 MV/m and a maximum difference of 1.38 MV/m and 1.90 MV/m for the 0.5 mm and 1.5 mm offsets respectively, when compared with the rescaled fields from the model with 0.25 mm offset. The on-axis percent-difference errors are shown in fig. 3.2, and are small (< 3% of maximum axial field) compared to the field magnitudes, with a mean absolute error of 0.45% for both offsets. This small RMS and mean absolute error justifies, from a

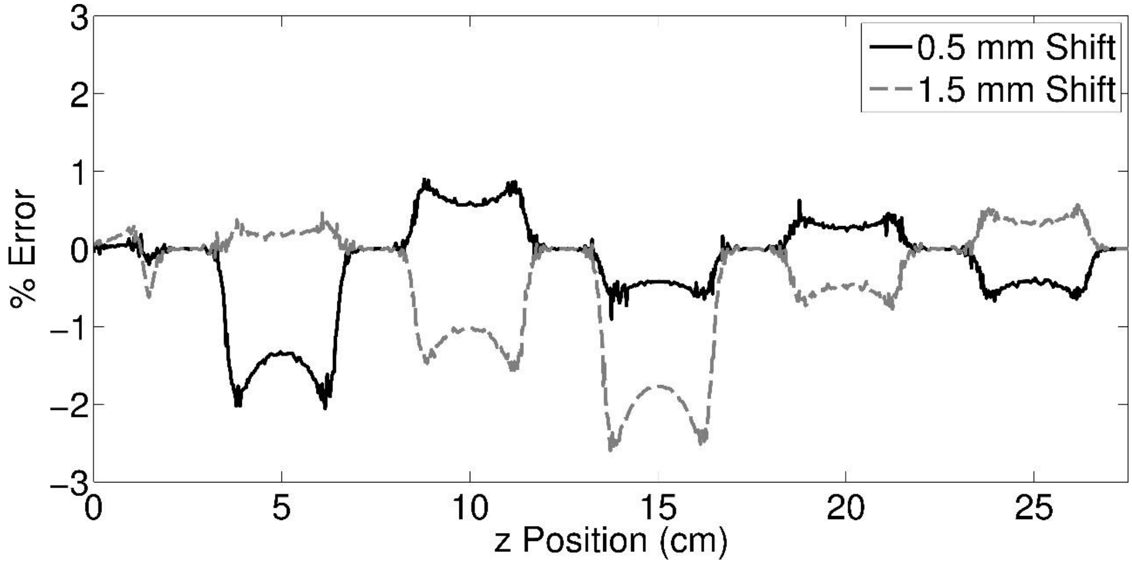

Figure 3.2: Error in the rescaled axial fields compared to the fields obtained by shifting the first coupling cavity, as a percentage of the maximum axial fields. The 0.5 mm coupling cavity shift is shown by the solid line, the 1.5 mm coupling cavity shift is shown by the dashed line.

feasibility stand-point, the field-scaling approach used in the study. As a point of reference, a 0.5 mm and 1.5 mm coupling cavity offset corresponds to a first cavity scaling factor of 0.88 and 0.62 respectively (determined by a least squares fit of the fields within the first half cavity).

All first cavity field scaling factors above 0.125 produce beam currents equal or higher than the magnetron powered waveguide (Fig 3.1b), with a beam current of 169.6 mA achieved with a scaling factor of 0.475. Because the higher energy electrons have a higher photon production efficiency (11), the photon energy fluence is expected increase by a factor of more than 5.

In previous simulations (4,5) the photon spectrum (in MV) corresponds approximately to the maximum electron energy (in MeV). Scaling the RF fields in the first half accelerating cavity does not significantly reduce the maximum electron energy (Fig 3.3a), and all scaling factors of 0.275 or greater produce maximum energies above 10 MeV. Therefore it is expect that these electron energy spectra are sufficient to produce

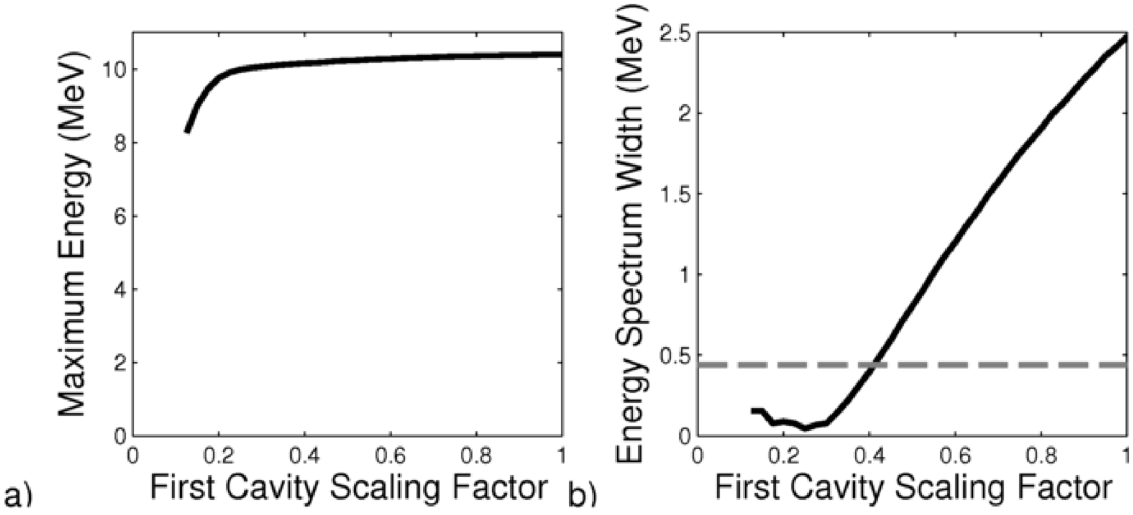

Figure 3.3: (a) The maximum electron energy as the first cavity fields are scaled. (b) The width of the electron energy spectrum (solid line), defined by the energies at which the relative intensity drops to 20% of the maximum, compared with the width of the energy spectrum produced by the magnetron powered (6 MV) waveguide (dashed line).

the target photon energy of 10 MV. The width of the electron energy spectrum, defined by the energies at which the relative electron intensity drops below 20% of the maximum, increases approximately linearly with scaling factor for scaling factors above 0.3 (Fig 3.3b). Without rescaling, the width of the spectrum increases by a factor of 5.5, from 0.44 MeV to 2.48 MeV when the input power is increased from 2.5 MW to 7.5 MW. This is because the first cavity RF fields have been optimized for electron capture with a 2.5 MW input power, and increasing the RF input power to 7.5 MW results in sub-optimal electron capture conditions. For scaling factors of 0.4 or below, the spectrum width is smaller than the original magnetron powered waveguide, and at a scaling factor of 0.475, the spectrum width is increased slightly from 0.44 MeV to 0.70 MeV (Fig. 3.4).

Without rescaling the first half-cavity, the FWHM of the electron beam has decreased from 0.07 mm in the x cross-section and 0.08 in the y cross section with the magnetron power source to 0.06 mm in both directions when a klystron is used, due to the stronger electric fields focusing the electron beam. The peak of the spatial distribution is not centered along the central axis of the waveguide. Using the magnetron power results in an offset of 0.25 mm and 0.10 mm in the x and y directions, respectively. The klystron power source gives a larger offset of 0.32 mm and 0.25 mm, without rescaling. When the first cavity fields are scaled by 0.475, the offsets are reduced to 0.18 mm and 0.01 mm, respectively. These offsets are not significant for treatment, as they can be accounted for by offsetting the waveguide with respect to the flattening filter, until symmetric dose distributions are produced (4). This is already done in the commissioning process for a linac.

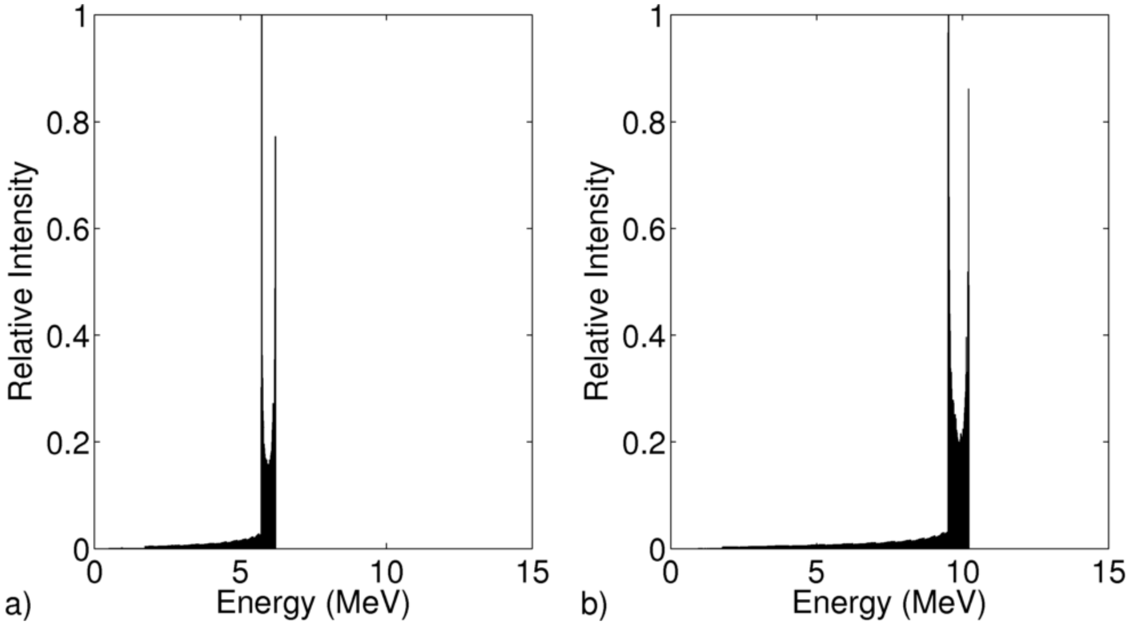

Figure 3.4: (a) The electron energy spectrum produced by the magnetron powered waveguide. (b) The electron energy spectrum produced by the klystron powered waveguide when the first cavity fields are scaled by 0.475. There isn't a generally accepted theory of why the bimodal peak distribution arises, one possibility is that the upper peak forms from particles which arrive at the second cavity at the optimum point for acceleration, and nearby particles tend to converge on that point as they traverse the cavities; while the lower peak forms from the highest-energy particles exiting the first half cavity (peaked because the sinusoidal variation in field strength means that the highest density will be when the fields are a maximum) which arrive at the second cavity at a suboptimal time for acceleration, resulting in the lower final energy.

Monte Carlo simulations of PDDs using the electron spectrum in Fig. 3.4b (for the 0.475 scaling factor), are very similar (Fig. 3.5) to the measured PDDs from a Varian 10 MV linear accelerator. The depth of maximum dose for the klystron powered model is 2.2, 2.1, and 2.0 cm at 4×4, 10×10 and 20×20 cm^2 field sizes respectively, compared to 2.45, 2.3, and 2.1 cm for the measured Varian 10 MV data. The dose at 10 cm depth is 69, 72, and 74% of dose maximum at 4×4, 10×10, and 20×20 cm^2 field sizes respectively, compared with 71, 74, and 75% for the measured Varian 10 MV data. These numbers suggest that the spectrum produced by the simulated waveguide is very close to, though slightly lower in energy than a 10 MV beam. The photon energy could be further

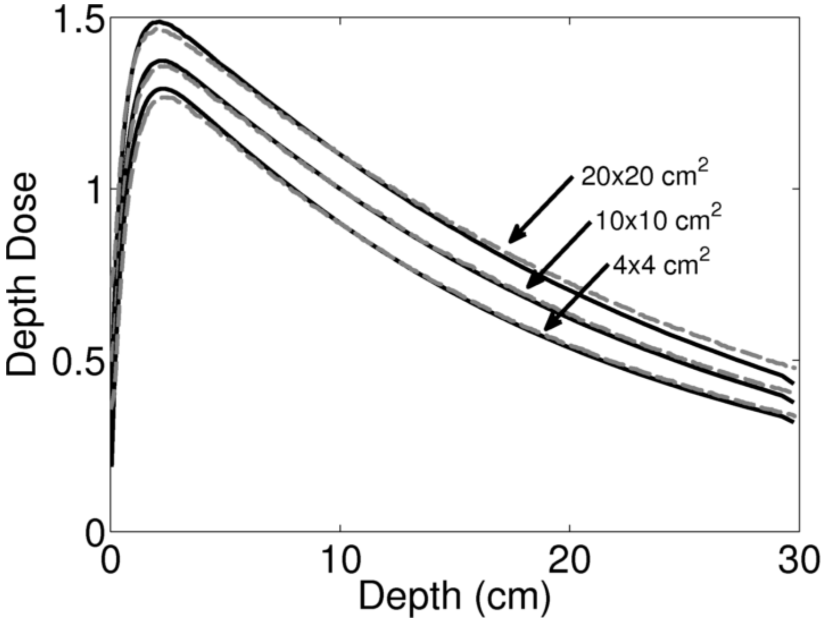

Figure 3.5: PDD produced by the simulated waveguide model with a first cavity scaling factor of 0.475 (solid line) and a PDD measured from a Varian 10 MV linac with a bend magnet (dashed line). Normalized to dose at 10 cm depth. Uncertainty in calculated dose is less than 1% at all depths, and 0.2% near d_{max}. Each PDD was independently scaled in this figure for visual clarity.

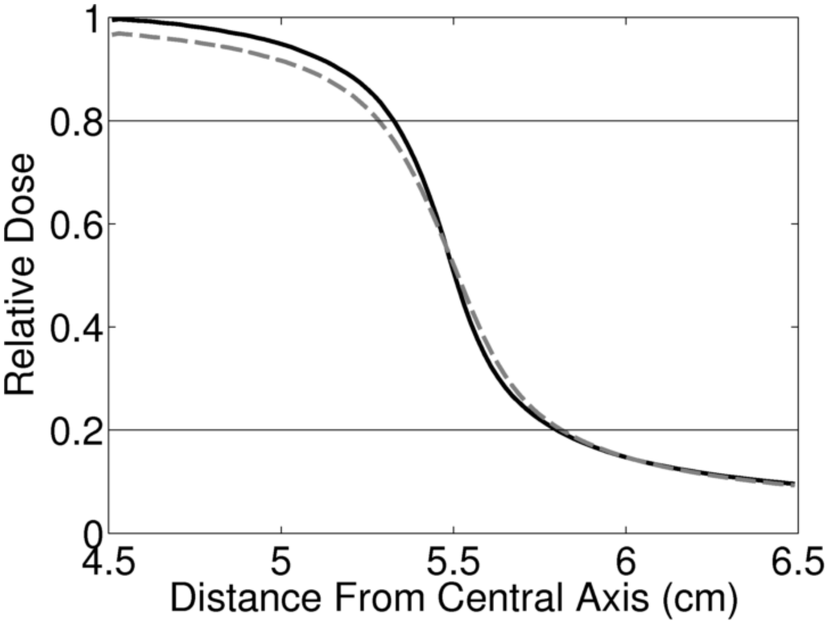

Figure 3.6: Penumbra of a 10x10 cm^2 field at 10 cm depth produced by the simulated waveguide model with a first cavity scaling factor of 0.475 (solid line) and produced by published Varian 10 MV linac electron beam parameters (dashed line) (9). Normalized to central axis dose at 10 cm depth. Uncertainty is less than 0.2% at all points.

increased by increasing the input RF power, or by redesigning the waveguide cavity geometry for improved acceleration. It should be noted that the 10 MV flattening filter used in these simulations would require re-optimization to deliver flat beam profiles, since the focal spot distribution and energy from the simulated linac model is different than a Varian 10 MV linac.

The penumbras of the two simulated 10×10 cm^2 fields at 10 cm depth are very similar (Fig. 3.6). The width of the penumbra (defined as the distance over which dose drops from 80% to 20% of the central axis dose) is 4.8 mm when using the electron beam from the simulated waveguide model with a 0.475 scaling factor, and 5.6 mm when using the electron beam parameters from Sheikh-Bagheri and Rogers (9). The electron focal spot FWHM of the simulated model is 0.05 mm, compared with 1.5 mm published for a Varian 10 MV linac, which would contribute to the sharper penumbra generated here.

3.4 Conclusions

Through simulations, the effect of replacing the magnetron power source on a simulated linear accelerator waveguide emulating a Varian 600C with a klystron power source has been investigated. The RF fields inside were compared against experimental breakdown limits for this operating frequency, and found to be 30% lower than published thresholds. The effects of increasing the power on the beam parameters were also calculated and an electron energy of 10 MeV is achieved. The electron beam current is increased, and electron focal spot FWHM is decreased. The only beam parameter negatively affected is the width of the energy spectrum, which is recoverable through minor modifications to the first coupling cavity. It has been shown that the photon beam produced by this waveguide is very close to that of a Varian 10 MV accelerator and therefore that it is feasible to produce a short, s-band high-energy linear accelerator.

3.5 References

1. El-Ashmawy M, Uesaka M, Iijima H, Imai T, Quyet NH. Overall Quality Comparison of C-Band and X-Band Medical Linacs. In: The 14th symposium on Accelerator Science and Technology, Tsukuba, Japan. 2003.

2. Wang JW. RF properties of periodic accelerating structures for linear colliders. SLAC-Report-339; 1989.

3. Wang JW, Loew GA. Field emission and rf breakdown in high-gradient room temperature linac structures. Stanford Univ., Stanford Linear Accelerator Center, CA (US); 1997.

4. St. Aubin J, Steciw S, Fallone BG. The design of a simulated in-line side-coupled 6 MV linear accelerator waveguide. Med Phys. 2010;37:466–76.

5. St. Aubin J, Steciw S, Kirkby C, Fallone BG. An integrated 6 MV linear accelerator model from electron gun to dose in a water tank. Med Phys. 2010;37:2279–88.

6. St. Aubin J, Steciw S, Fallone BG. Effect of transverse magnetic fields on a simulated in-line 6 MV linac. Phys Med Biol. 2010;55:4861–9.

7. Young LM BJH. Parmela. LA-UR-96-1835, Rev; 2005.

8. Rogers DWO, Faddegon BA, Ding GX, Ma CM, We J, Mackie TR. BEAM: A Monte Carlo code to simulate radiotherapy treatment units. Med Phys. 1995;22:503.

9. Sheikh-Bagheri D, Rogers DWO. Sensitivity of megavoltage photon beam Monte Carlo simulations to electron beam and other parameters. Med Phys. 2002;29:379.

10. Varian Medical Systems Monte Carlo Data Package. Available under non-disclosure-agreement from Varian Medical Systems;

11. Koch HW, Motz JW. Bremsstrahlung cross-section formulas and related data. Rev Mod Phys. 1959;31(4):920–955.

4. 10 MV Linac Design

A version of this chapter has been published. Devin Baillie, J. St. Aubin, B. G. Fallone, S. Steciw, "FEM design and simulation of a short, 10 MV, S-band Linac with Monte Carlo dose simulations," Medical Physics 42 (4) 2044 (2015)

4.1 Introduction

Having completed the feasibility assessment, the goal of the research presented in this chapter is to design a new 10 MV accelerator waveguide. The previous chapter showed that the fields required to produce a 10 MV x-ray beam are more than 30% below the breakdown threshold predicted by Eq. 2.68. However, as discussed in section 2.4, Eq. 2.68 does not account for the geometric dependence of the breakdown threshold. The feasibility study also used field scaling within the waveguide to approximate optimizations, rather than actually designing an optimized waveguide geometry. Therefore this chapter begins with the design of an individual accelerating cavity based on experimental breakdown thresholds published by Tanabe (1), to be used as the basis of a new 10 MV waveguide design. The new waveguide is to be the same length as the Varian 600C waveguide currently used in the linac-MR project at the Cross Cancer Institute but capable of producing energies up to 10 MV without exceeding the breakdown threshold determined by Tanabe.

4.2 Methods

4.2.1 Waveguide Design and RF Solution

The first stage of the waveguide design was to model an accelerating cavity based on the experiment published by Tanabe (1). The axial field at breakdown, $E_{0\mathrm{th}}$, for the three cavities investigated by Tanabe is 66.3 MV/m, 43.6 MV/m, and 30.5 MV/m, respectively. In order to produce a shorter, higher-energy accelerator, the highest possible axial field at breakdown, $E_{0\text{th}}$, is required as this is the field that accelerates electrons. The high accelerating field in the first cavity required for breakdown make it the most promising candidate for use as a higher energy accelerator. As Tanabe did not publish the cavity geometry, a single cavity was simulated using COMSOL Multiphysics using an axisymmetric geometry and the eigenfrequency solver to calculate the shunt-impedance, Q factor, and field ratio in order to match the published parameters (Table 4.1). A stochastic optimization was then run by varying the dimensions from Fig. 4.1. The dimensions from the existing linac model (2) were used as initial conditions, and new dimensions were chosen randomly within a window about the current "best solution" while the window width was reduced by 5% every 10 iterations. The "best solution" was the minimum of the summation of the absolute values of the percent errors in each of the three cavity metrics in table 4.1 (Q, ZT^2, and E_p/E_0). The termination condition was chosen to be 0.1% sum of the absolute values of the errors. This cavity was then used as the basis for the multi-cavity accelerating waveguide to ensure the applicability of the 239 MV/m breakdown threshold to the new accelerating waveguide.

Cavity	1	2	3
Q	18520	18411	16835
ZT^2	104	117.1	130.2
E_p/E_0	3.61	6.04	8.08
E_{th}	239.4	263.1	246.4
$E_{0\text{th}}$	66.3	43.6	30.5

Table 4.1: The cavity parameters published by Tanabe. Q is the quality factor, ZT^2 the shunt impedance, E_p/E_0 is the ratio between the peak fields within the waveguide and the average axial field, as defined in section 2.3.2, E_{th} is the peak fields within the waveguide when breakdown occurred and $E_{0\text{th}}$ is the average axial field at breakdown. This table previously appeared as table 2.1.

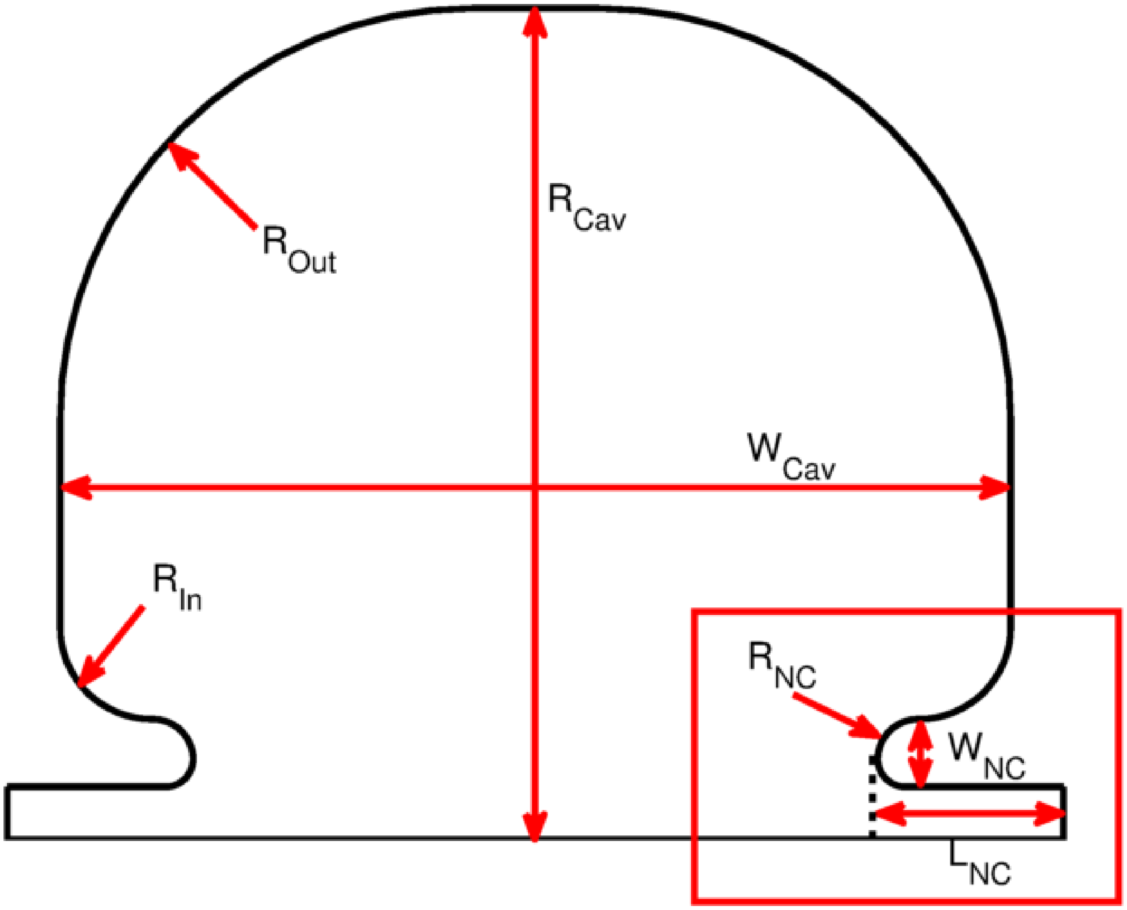

Figure 4.1: An axisymmetric cross-section of a single accelerator cavity. The dimensions varied to match the cavity parameters for cavity 1 in Table 4.1 are: The nose cone length, width, and outer radius of curvature; L_{NC}, W_{NC}, andR_{NC}, respectively. The cavity radius and width and the inner and outer radii of curvature;R_{Cav}, W_{Cav}, R_{In}, and R_{Out}, respectively. Because the electric fields are highest at the nose cones, this is where breakdown can occur, and the dimensions inside the red box are expected to determine breakdown thresholds. The beam hole radius was kept at 2.5 mm for consistency with the linac compared against.

A full waveguide was then designed by coupling six cavities together through side coupling cavities, where the first cavity was a half cavity for electron capture (3) (AC1 in Fig. 4.2). The length of each cavity must be one half the RF wavelength so that the electrons, which are travelling at ultra-relativistic speeds ($v \approx c$), traverse the cavity in one half RF period, arriving in the next cavity as the electric field becomes negative, allowing them to be accelerated through each of the cavities. The half cavity allows the electrons, which are not yet travelling at ultra-relativistic speeds, to traverse the cavity within one half RF period (3). The single cavity was designed to resonate at 2.997 GHz, however the irises between the side coupling cavities and the accelerating cavities decreased the cavity inductance and increased the resonant frequency (see section 2.3.1) (4). The port to couple power from the RF source was placed in the first full accelerating cavity (AC2 in Fig. 4.2) instead of the third as in the feasibility study (2). This change was made to allow the ability to vary the beam energy in the future, but was unnecessary and reversed in later work. The coupling port in the first full cavity was intended to allow the fields in the first half-cavity and the fields in the remaining cavities (AC1 and AC3 to AC6 in Fig. 4.2) to be independently varied using energy switches. The port dimensions were unchanged from the previous work, 17.1 mm × 23.5 mm with 3.4 mm radius of curvature on the corner (5,6). The input port again decreased the cavity inductance, increasing the resonant frequency. The resonant frequency of a particular cavity was determined by adding copper spheres to detune the other cavities. This process is analogous to the tuning of physical waveguides by adding metal spheres to detune certain cavities. For these simulations, spheres with a diameter of 90% of the gap size (distance between nose cones for the accelerating cavities, distance between the posts in the coupling cavities) with perfectly conducting boundary conditions were used. These are much larger than would be physically possible in an actual waveguide, where the sphere size is limited by the size of the openings. The use of larger spheres saved significant computational expense because the interior of the spheres was not meshed. COMSOL was then used to calculate the eigenfrequency of the sphere-filled waveguide. Because of the lack of symmetry due to the side coupling cavities and the

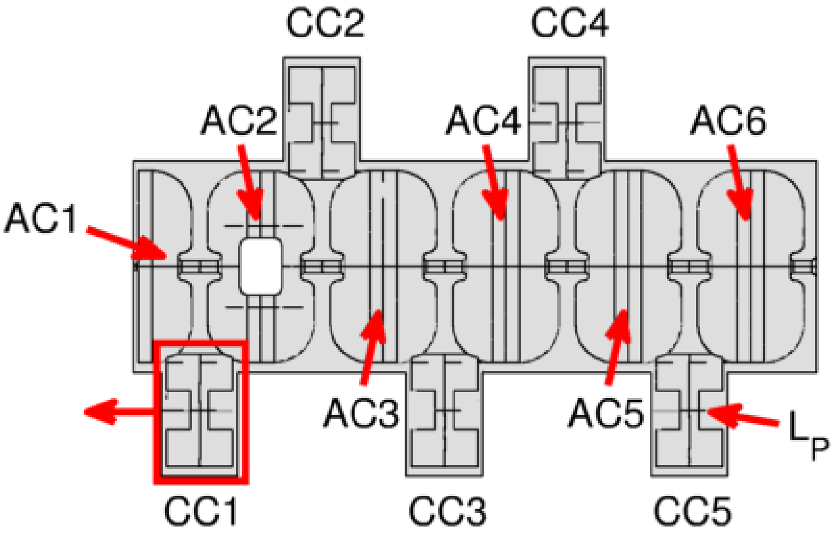

Figure 4.2: A full accelerator constructed by coupling multiple accelerating and side-coupling cavities together. The electrons enter from the electron gun into AC1, and are accelerated through AC1 to AC6. Power enters the waveguide through the port in AC2. The cavities are tuned by adjusting the diameter in the accelerating cavities (ACX), and the post length in the coupling cavities (CCX). The first coupling cavity (CC1) is offset by varying amounts to control RF power flow into AC1. The length of the posts (L_P) in each coupling cavity is adjusted to tune the resonant frequency.

input port, this required a full 3D model with between 90,000 and 120,000 3rd order isoparametric elements with cubic interpolation functions, a minimum element quality of approximately 0.09 and an element volume ratio of approximately 2.8×10^{-6}, and took approximately 1 hour on a computer with four 12 core 2.2 GHz AMD Opteron 6174 CPUs and 224 GB of RAM.

In order to restore the resonant frequency of the accelerating cavities after the addition of the coupling cavities and the input port, each cavity had to be individually tuned. In the previous work (2,6) to emulate the Varian 600C, this was done by adjusting the nose cone length (L_{NC} in Fig. 4.1) to increase or decrease the cavity capacitance in order to adjust the frequency. Because the nose cone is the source of electric breakdown, the dimensions of the nose cone were kept identical to resulting from matching the cavity parameters in the Tanabe breakdown study. Instead, the cavity radius was adjusted (R_{Cav}

in Fig. 4.1) to control the inductance, which allowed the frequency to be controlled. The coupling cavities were tuned by adjusting the length of the posts (L_P in Fig. 4.2) until each coupling cavity resonated at the same frequency as the accelerating cavities. The resonant frequency of a single cavity was calculated, the diameter adjusted, and the resonant frequency recalculated until the cavity resonated at 2997 ± 0.1 MHz. This process was repeated for each of the accelerating cavities.

After fully tuning each cavity of the waveguide, the RF fields within the waveguide were calculated using the COMSOL RF Module PARDISO solver to find the steady state (harmonic) solution when power is applied at the port. In the previous work (2,6), 2.3 MW excitation at the port accurately matched the output from the 2.5 MW magnetron. Tripling this gave 6.9 MW excitation at the port to simulate a 7.5 MW klystron power source. This model had approximately 470,000 3rd order isoparametric elements, solving with cubic interpolation functions, a minimum element quality of approximately 0.25, an element volume ratio of approximately 1.1×10^{-4}, and took approximately 2 hours on the same computer as the tuning operation. The peak surface fields calculated within the waveguide were then compared with E_{th} from Table 4.1, to determine whether electric breakdown would become an issue.

Previous work has shown that the field strength in the first half accelerating cavity (AC1 in Fig. 4.2), have a large effect on the resulting electron spectrum (6), and therefore need to be precisely optimized to improve the electron (and photon) beam properties. These fields were controlled by offsetting the first coupling cavity (CC1 in Fig. 4.2) towards the electron gun end of the waveguide, which shrinks the coupling iris and reduces the power coupled into the half cavity. Because the size of the coupling irises changed with this offset, the resonant frequencies of the first two accelerating cavities and the first coupling cavity also changed. These cavities therefore required retuning using the same method as the initial tuning for each coupling cavity shift. Retuning the second accelerating cavity (AC2 in Fig. 4.2) affected the resonant frequency of the second coupling cavity (CC2 in Fig. 4.2), so this cavity also required retuning. After retuning, the RF solution was recalculated. Reduced power in the first half cavity resulted in higher field strengths in the remaining cavities, so the peak fields within the waveguide were compared to the threshold for each shift investigated. The electron trajectories within the waveguide were then recalculated for each coupling cavity shift, producing one electron phase space incident on the x-ray target for each cavity shift.

4.2.2 Electron Dynamics

PARMELA was then used to calculate the electron trajectories as they are accelerated by the RF fields calculated in the waveguide. As in the previous chapter, the harmonic RF solution from COMSOL was interpolated onto a 25x25x1536 rectilinear grid (a 25x25x128 regular grid in each half cavity and the final portion of the electron gun) grid for use with PARMELA (7). The electron phase space injected into the waveguide was produced by the same Opera 3D/SCALA simulated electron gun as in the previous work by Dr. St. Aubin et al. (8). The PARMELA reference particle was started at a phase of -45°, to ensure it remained in the center of the travelling bunch, and RF phase was increment by 3.6° (3.3 ps) for each step. 3D space charge effects were calculated on a 32×32×256 grid. The injected electrons were uniformly spread over two RF periods, which produced leading and trailing half-bunches, which were discarded during post-processing. Spreading the input electrons over two full periods instead of one accounted for effects of leading and trailing bunches on the central bunch, removing simulation end effects. For each waveguide model, PARMELA was run until 45×10^6 were kept (ie. Not counting those discarded during processing).

In order to evaluate the electron energy spectrum produced by the new linac model, the energy and energy spectrum width of the resulting electron beam were compared with those of an electron energy spectrum emulating a Varian 10 MV linac, published by Sheik-Bagheri and Rogers (9). The full width at half maximum (FWHM) of the electron energy spectrum was compared with the value published by Sheik-Bagheri and Rogers to emulate a Varian 10 MV linac. Quantifying the energy of the beam was not entirely straightforward due to the differently shaped spectra. Spectrum produced by actual linear accelerators or full simulations (especially in the absence of bend magnets) tend to be bimodal (with 2 peak energies) with a low energy tail which does not contribute significantly to the eventual photon beam. Sheik-Bagheri and Rogers produced electron spectrums by using a Gaussian electron energy distribution to match photon output; because the low energy tail does not contribute to the photon beam, it is not accounted for in the emulated Varian 10 MV electron. Additionally, in high energy linacs using bend magnets, the low energy tail is removed using an energy selection window. Instead of the mean of all energies, the mean of the energies above 7 MeV was used, which was expected be more comparable to the Gaussian spectrum used in Sheik-Bagheri and Rogers. A cutoff of 7 MeV was chosen to remove the tail without removing any portion of the peak (relative intensity > 5%) for any of the spectra produced. The choice of cutoff energy can slightly change the specific mean energies computed, but values above 6 MeV produce very similar results. However, a cutoff above 7.8 MeV will remove a portion of the peak region, more significantly affecting the results for some of the spectra. While the FWHM and the mean energy do not fully characterize the bimodal distributions, as the FWHM approaches 0.5 MeV, the two peaks overlap and the FWHM and mean are expected to provide a reasonable comparison to the Gaussian distribution in this region.

4.2.3 Monte Carlo Dose Calculations

EGSnrc was then used to calculate dose distributions produced by the new waveguide models in a water phantom, for comparison with an existing 10 MV linac. A 10 MV linac head (target, primary collimator, flattening filter, monitor chamber, mirror, and jaws) was simulated in BEAMnrc following Varian specifications (10), and the electron phase spaces produced by PARMELA were converted to an input phase space and used as input (5). For each coupling cavity shift, three field sizes were simulated: 4 cm × 4 cm, 10 cm × 10 cm, and 20 cm × 20 cm, producing three phase spaces for input into DOSXYZnrc. DOSXYZnrc was then used to calculate depth dose curves and beam penumbras for each shift and field size. The depth dose curves were calculated with voxel sizes of 5 mm × 5 mm × 1 mm for the first 3.5 cm depth and 5 mm × 5 mm × 5 mm until 30 cm depth, with the phantom modeled to 40 cm depth to ensure accurate backscatter. As in the feasibility study (5), 100×10^6 histories were used for the BEAMnrc simulations and 15×10^9 for the DOSXYZnrc simulations. For comparison purposes, the BEAMnrc and DOSXYZnrc simulations were repeated using the Varian 10 MV electron beam properties from Sheik-Bagheri and Rogers (9). The depth of maximum dose, d_{max}, and the ratio of doses at 10 cm and 20 cm, $D_{10/20}$, were calculated for each field size, plotted against the cavity offset, and compared to the results for the

Varian 10 MV spectrum. These results were used to further adjust the coupling cavity offset for better agreement. The choice to match the spectrum of a Varian 10 MV linac was made based on the availability of data, however the linac designed here could be made to match any beam specification of a 10 MV linac desired with minor modification.

4.3 Results and Discussions

The stochastic optimization to match the cavity parameters from Tanabe resulted in the dimensions in Table 4.2. Running the stochastic optimization multiple times with different initial conditions consistently produced less than 1% variation in the nose cone dimensions, while variations up to 5% were produced in the remaining dimensions. The diameter of the accelerating cavities after retuning, as well as the post length in the coupling cavities, are shown with no coupling cavity shift and with a coupling cavity shift of 1.45 mm in Table 4.3.

The maximum electric field, E_p, within the simulated waveguide for each coupling cavity shift is between 12% and 15% below the breakdown threshold of 239 MV/m. Because the breakdown threshold of 239 MV/m is already conservative due to advances in RF processing and vacuum systems since the experiment was done, electric breakdown is not expected to be a problem for any of the simulated waveguide models.

L_{NC}	8.79 mm
W_{NC}	3.20 mm
R_{NC}	1.89 mm
W_{Cav}	43.63 mm
R_{Cav}	39.39 mm
R_{Out}	16.28 mm
R_{In}	4.35 mm

Table 4.2: Cavity dimensions to match the parameters published by Tanabe. All dimensions are in mm.

Cavity #	R_{Cav}	L_{P}	R_{Cav}^{*}	L_{P}^{*}
1	39.338	9.626	39.315	9.624
2	39.106	9.628	39.115	9.629
3	39.338	9.623	39.338	9.623
4	39.338	9.624	39.338	9.624
5	39.338	9.622	39.338	9.622
6	39.363	N/A	39.363	N/A

Table 4.3: Accelerating cavity radii (R_{Cav}) and coupling cavity post lengths (L_{P}) after tuning the unshifted and the 1.45 mm shifted (denoted by a *) accelerator models. All units are mm.

The electron energy spectrum is compared against the Varian 10 MV spectrum from Sheik-Bagheri and Rogers for the simulated waveguide with no coupling cavity shift (Fig. 4.3a) and with a shift of 1.45 mm (Fig. 4.3b). The FWHMs of the unshifted model, the 1.45 mm shift model and the Varian spectrum are 3.12 MeV, 0.347 MeV, and 0.315 MeV, respectively. The mean energy of the peak (defined as the mean energy of all particles with energies above 7 MeV) are 9.67 MeV, 10.53 MeV, and 10.5 MeV, for the the unshifted model, the 1.45 mm shift model and the Varian spectrum, respectively. The fraction of the electron beam with energy below 7 MeV is 0.12, for the unshifted model and 0.13 for the 1.45 mm shifted model. Figure 4.4 shows how the FWHM varies as the coupling cavity is shifted, and compares against the Varian spectrum, and Fig. 4.5 shows the mean energy of the peak region, again compared to the Varian spectrum. Taken together, the electron spectrum produced with a shift of 1.45 mm is very similar to the Varian spectrum. Figure 4.6 shows the electron beam current incident on the target, which is more than double is more than double that measured on a Varian 10 MV linac (40 mA) for shifts less than 0.25 mm, and more than triple for shifts greater than 0.25 mm. This was not a specific design goal, but a result of the electron gun used. The uncertainty in Figs. 4.4 - 4.6 is not statistical uncertainty in the particle simulations (the statistical uncertainty and uncertainty arising from the finite size of the energy 'bins' used

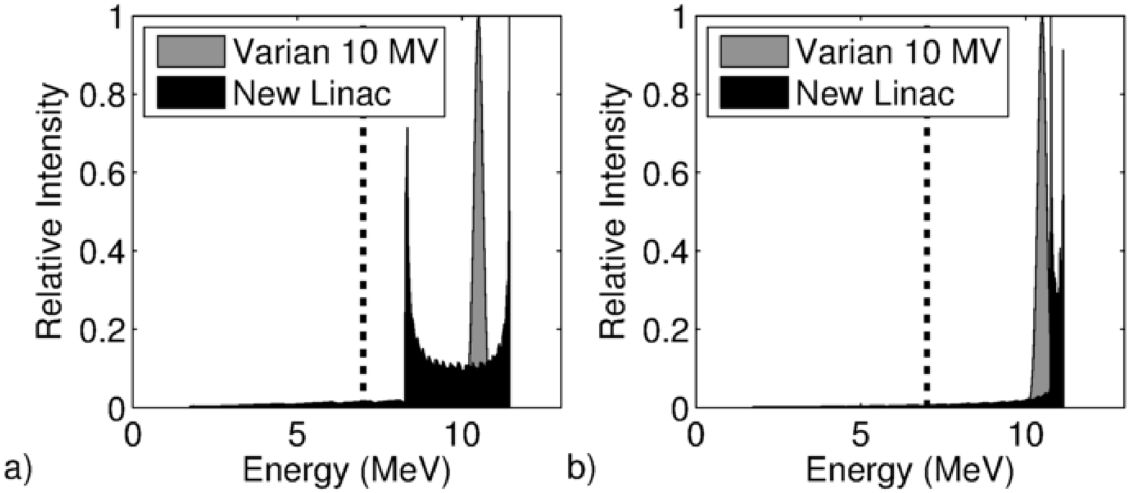

Figure 4.3: Electron energy spectrum produced by an emulated Varian 10 MV linac (grey) compared to the spectrum produced by the new waveguide design (black) for the unshifted model (a) and the 1.45 mm shift (b). The dashed line is the 7 MeV cutoff, below which electrons were not included in the beam energy or beam current calculations.

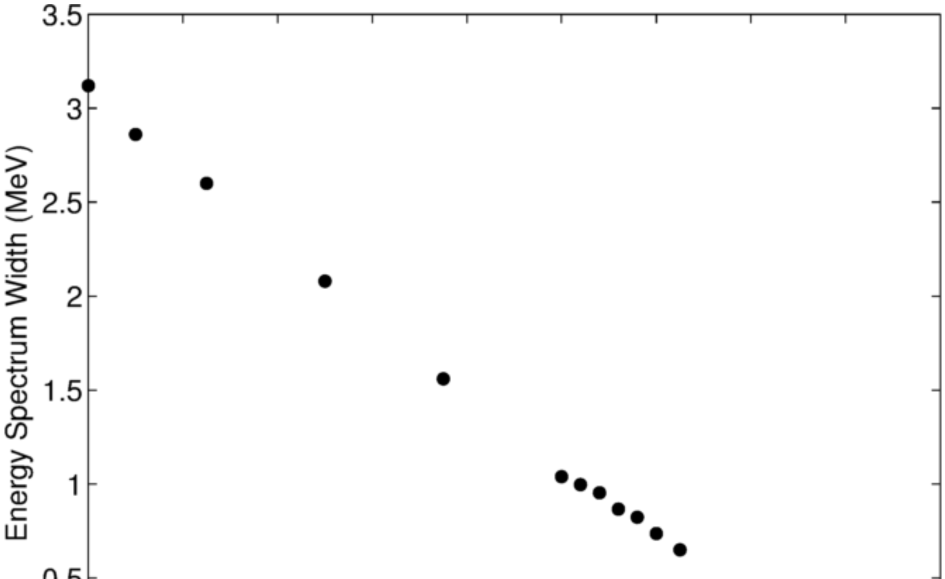

Figure 4.4: Electron beam FWHM as the coupling cavity is shifted (black points), compared with that of the spectrum of an emulated Varian 10 MV linac (dashed grey line). The error from statistical noise or the size of the bins used in the analysis is smaller than the markers on the graph.

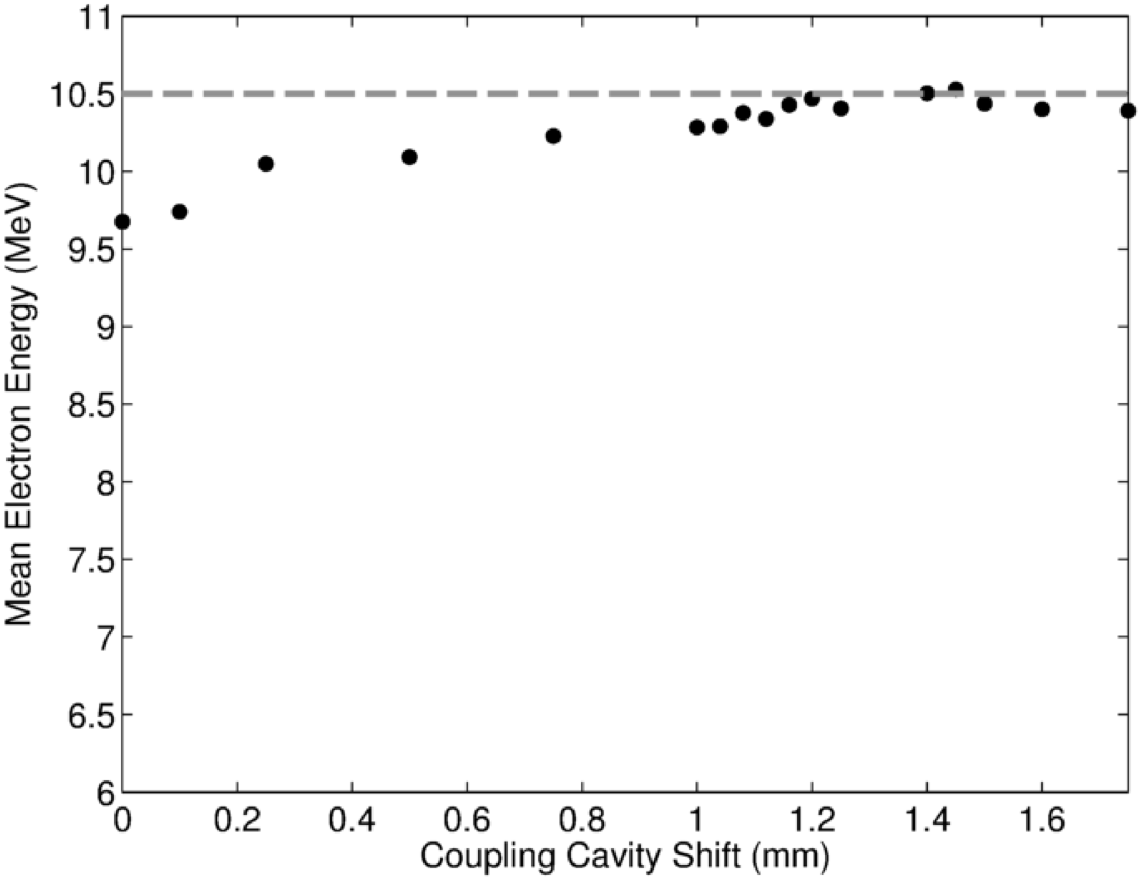

Figure 4.5: Electron beam energy as the coupling cavity is shifted (black points), compared with that of an emulated Varian 10 MV linac (dashed grey line). Electron beam energy is defined here as the mean energy of the electrons with energies greater than 7 MeV.

in the data processing is smaller than the point markers on the graphs), but rather a result of the imperfection of the tuning procedure.

The x and y transverse cross sections of the electron phase space are plotted in Fig. 4.7 for the waveguide with the 1.45 mm coupling cavity shift, and the electron focal spot on the target is shown in Fig. 4.8. The FWHM of the electron focal spot (Fig. 4.8) is 0.07 mm. The increased beam current and smaller focal spot will result in higher power per unit area in the target which will have an impact on target longevity. A detailed investigation into the effect of the higher power per unit area in the target, potential cooling techniques, target design and other mitigation strategies, such as defocusing the

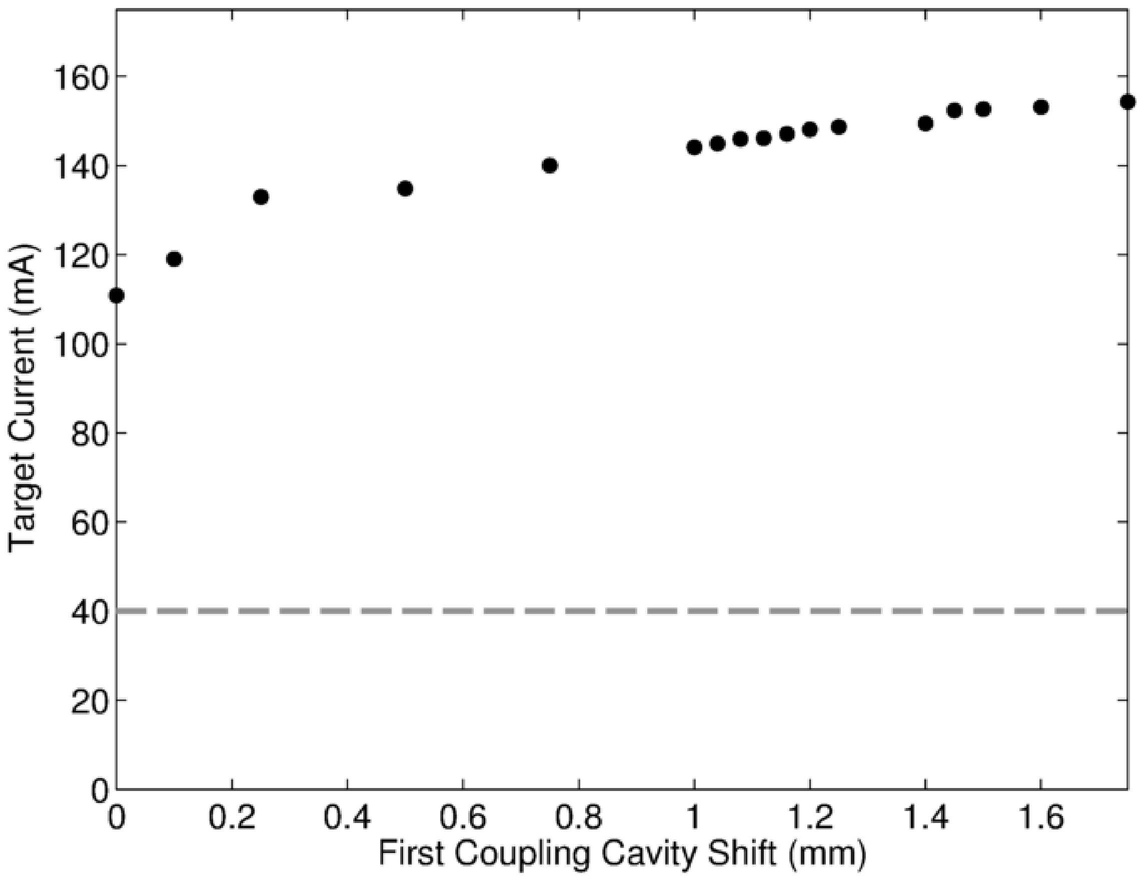

Figure 4.6: Waveguide target current as the coupling cavity is shifted (black points), compared against the target current measured on a Varian 10 MV linac (dashed grey line). The target current only includes those electrons with energies greater than 7 MeV.

electron beam using a magnet, will be investigated in the future, but is beyond the scope of this investigation. The relatively large asymmetry in the y direction (Fig. 4.7b and 4.8) is due to the input coupling port causing asymmetries in the RF fields (6) in the second accelerating cavity (AC2 in Fig. 4.2). Due to this asymmetry, the y direction RMS emittance, $\epsilon_{\mathrm{y,rms}}$, is much larger than the x direction, $\epsilon_{x,\mathrm{rms}}$. In the y direction, the RMS emittance is 0.397 π mm mrad, while in the x direction it is 0.122 π mm mrad.

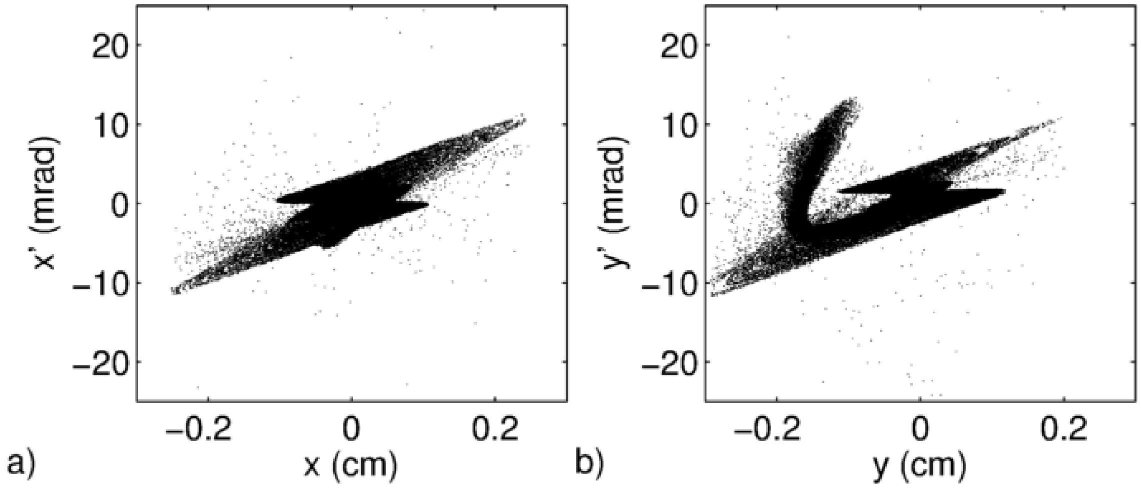

Figure 4.7: Transverse cross sections of the electron phase space incident on the x-ray target. The divergences ($x' = p_x/p$ and $y' = p_y/p$) are plotted along the ordinate axis while the displacement from the position of maximum intensity is on the abscissa axis.

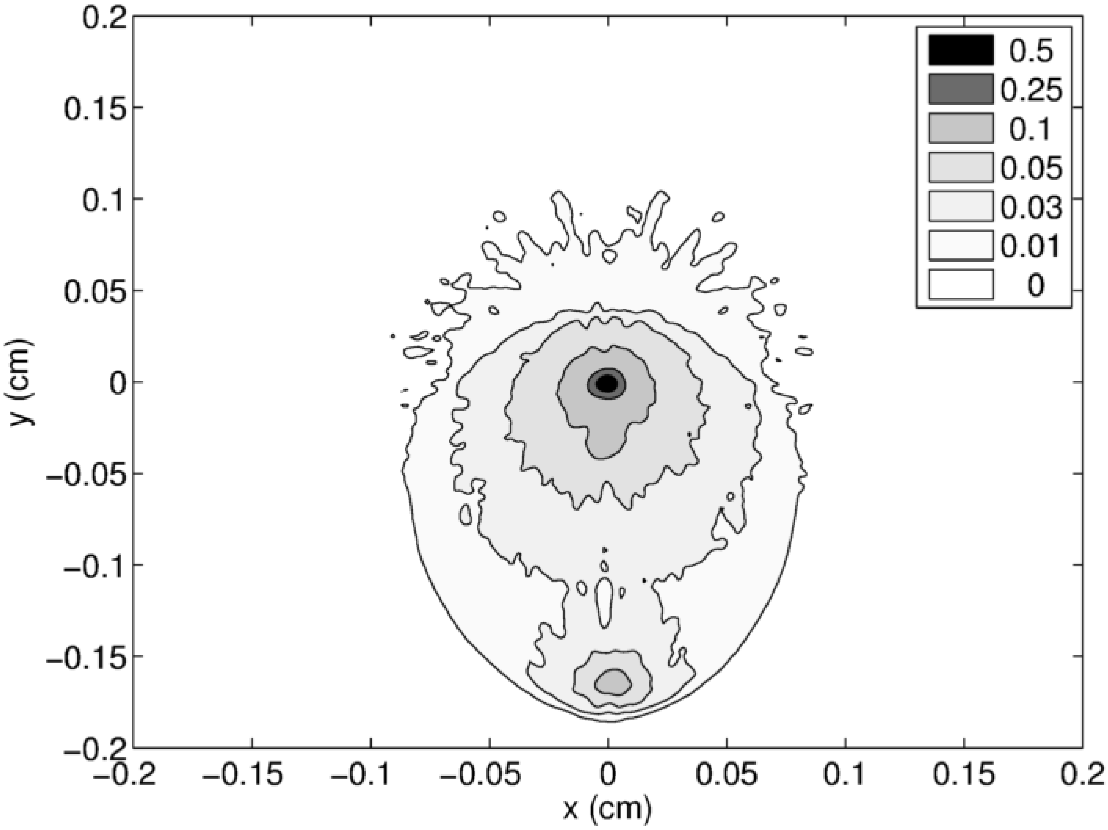

Figure 4.8: Electron focal spot distribution on the x-ray target, normalized to and centered on the maximum intensity. The darkest region shown corresponds to 50% of the maximum intensity, and has a diameter of approximately 0.07 mm. The smaller focal spot with 10% intensity at about $y = -0.15\ \mathrm{cm}$ corresponds to the similarly positioned asymmetric feature in the phase space plot Fig. 4.7b.

The depth dose profile is compared against one from an identical simulation with a Varian 10 MV spectrum, again for the waveguide model without any coupling cavity shift (Fig. 4.9a) and with a shift of 1.45 mm (Fig. 4.9b). The higher and narrower energy spectrum of the 1.45 mm shifted waveguide produces a depth dose profile that is within 1% of the Varian 10 MV profile for all points deeper than 1.5 cm, showing that the beam energy is equivalent to existing Varian 10 MV. Figure 4.10 shows the same comparisons for the beam penumbra, which are narrower than that of the Varian 10 MV.

The width of the penumbra (Fig. 4.10b) for the new linac design is smaller than that of the Varian 10 MV. If the penumbra width is defined as the distance over which the dose drops from 80% to 20% of the central axis dose, the new linac without coupling cavity shift (Fig. 4.10a) produces a penumbra width of 6.4 mm, which is 14% larger than the Varian penumbra width of 5.6 mm. However, with a coupling cavity shift of 1.45 mm, (Fig. 4.10b) the penumbra width is reduced by 22% to 5.0 mm, which is 11%

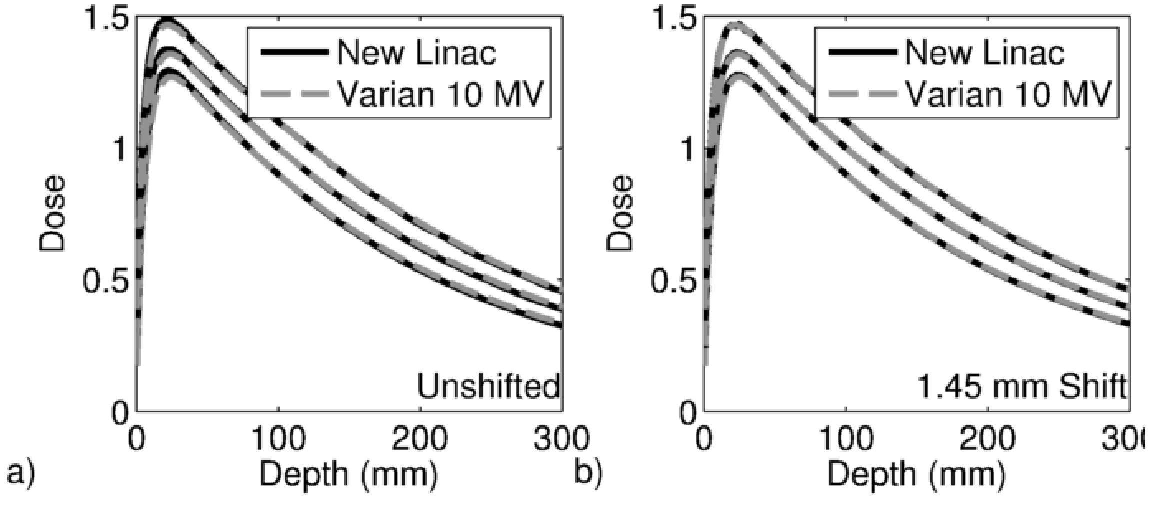

Figure 4.9: Depth dose profile from an emulated Varian 10 MV linac (dashed grey) compared to the profile produced by the new waveguide design (solid black) for the unshifted model (a) and the 1.45 mm shift (b). Each field size has been normalized at 10 cm depth, and then independently scaled for clarity (scaling factors of 0.9, 1.0, and 1.1 for field sizes of 4 × 4 cm^2, 10 × 10 cm^2 and 20 × 20 cm^2, respectively).

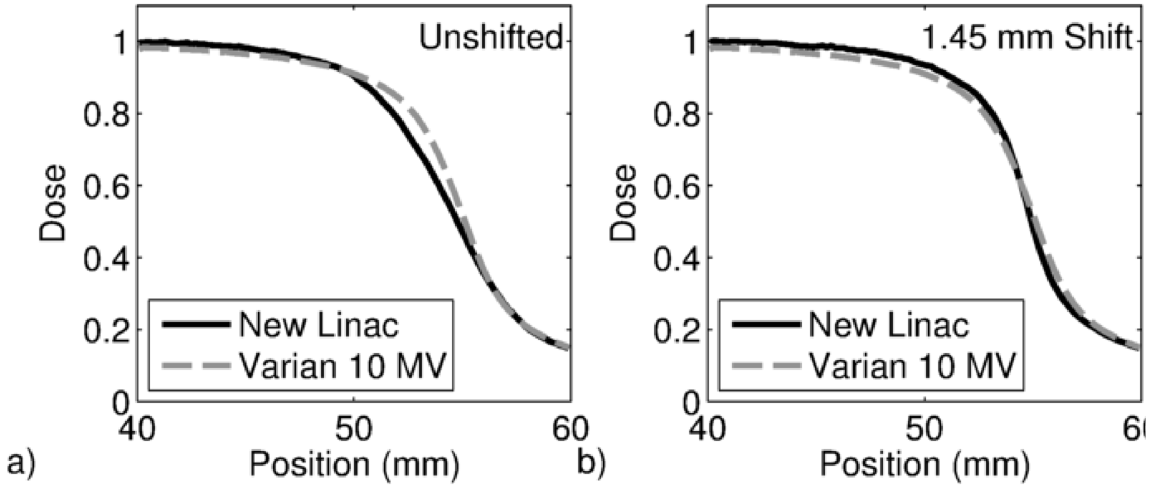

Figure 4.10: Beam penumbra from an emulated Varian 10 MV linac (dashed grey) compared to the penumbra produced by the new waveguide design (solid black) for the unshifted model (a) and the 1.45 mm shift (b). Each field is normalized to the central axis dose. Due to the y direction asymmetry of the beam shown in Figs. 4.7 and 4.8, these penumbrae are taken in the y direction to demonstrate the worst case scenario.

smaller than the Varian's. The FWHM of the focal spot with the 1.45 mm shifted model is 0.07 mm, while that published for the Varian 10 MV is 1.5 mm. While this FWHM is about 20 times smaller than the published value, it does not fully describe the size and shape of the focal spot (Fig. 4.8). If the FWHM of the Varian 10 MV focal spot is artificially reduced to 0.07 mm and the simulation repeated, the penumbra width is reduced to 5.3 mm, indicating that most of the difference between the 1.45 mm shifted model and the Varian 10 MV linac is due to the focal spot size. The remaining difference may be due to the shape of the electron distribution on the target or the differences between the energy spectra.

The depth of maximum dose, $d_{\max}$, for a 10 cm × 10 cm field varies with the coupling cavity shift between 22.3 cm and 23.4 cm. The ratio of dose at 10 cm and 20 cm depth, $D_{10/20}$, for a 10 cm × 10 cm field varies between 1.59 and 1.61. At a shift of 1.45 mm there is a $d_{\max}$ of 23.40 mm, within 0.5 mm of the 123.73 mm $d_{\max}$ for the

Varian 10 MV and a $D_{10/20}$ of 1.595, within 0.5% of the Varian 10 MV, at 1.589.

4.4 Conclusions

The research outlined in this chapter presents the design and simulation of a linear accelerator waveguide capable of producing a 10 MV photon beam, with the waveguide length of 27.5 cm (same as a 600C waveguide). The maximum electric field strengths inside the waveguide were computed to be more than 12% below the breakdown threshold specific to the cavity design used. It should be noted that the threshold is already conservative due to advances in vacuum and surface finishing since the publication of the breakdown threshold (11). With a first-coupling-cavity shift of 1.45 mm, the electron beam energy and spectrum FWHM are nearly identical to that of an emulated Varian 10 MV linac, while the electron beam current incident on the target is more than 3 times greater than that measured on a Varian 10 MV. The depth of maximum dose is within 0.5 mm of that produced by the Varian 10 MV linac, and the ratio of dose at 10 cm depth to the dose at 20 cm depth is within 0.5%. For all depths greater than 1.5 cm, the depth dose profiles produced by the new linac agree to within 1% to that of the Varian 10 MV linac. The penumbra of the beam produced by the new linac is 11% smaller than that produced by the Varian 10 MV linac, which is expected to result in improved dose distributions. All the results obtained here are substantially similar to those obtained in the previous feasibility study, with the addition of dimensions for a specific waveguide geometry. This suggests that the field scaling approach used in the feasibility study was an accurate approximation to the coupling cavity offset used in this chapter.

4.5 References

1. Tanabe E. Voltage Breakdown in S-Band Linear Accelerator Cavities. IEEE Trans Nucl Sci. 1983 Aug;30(4):3551–3.

2. St. Aubin J, Steciw S, Kirkby C, Fallone BG. An integrated 6 MV linear accelerator model from electron gun to dose in a water tank. Med Phys. 2010;37:2279–88.

3. Karzmark CJ. Medical Electron Accelerators. McGraw-Hill, Inc., Health Professions Division; 1993.

4. Nagle DE, Knapp EA, Knapp BC. Coupled Resonator Model for Standing Wave Accelerator Tanks. Rev Sci Instrum. 2004 Dec 29;38(11):1583–7.

5. Baillie D, Aubin JS, Fallone BG, Steciw S. Feasibility of producing a short, high energy s-band linear accelerator using a klystron power source. Med Phys. 2013;40(4):41713.

6. St. Aubin J, Steciw S, Fallone BG. The design of a simulated in-line side-coupled 6 MV linear accelerator waveguide. Med Phys. 2010;37:466–76.

7. Young LM BJH. Parmela. LA-UR-96-1835, Rev; 2005.

8. St. Aubin J, Steciw S, Fallone BG. Effect of transverse magnetic fields on a simulated in-line 6 MV linac. Phys Med Biol. 2010;55:4861–9.

9. Sheikh-Bagheri D, Rogers DWO. Sensitivity of megavoltage photon beam Monte Carlo simulations to electron beam and other parameters. Med Phys. 2002;29:379.

10. Varian Medical Systems Monte Carlo Data Package. Available under non-disclosure-agreement from Varian Medical Systems;

11. Wang J, Loew G. Field emission and rf breakdown in high-gradient room-temperature linac structures. SLAC-PUB-7684; 1997.

5. Tunable Linac Design

A version of this chapter has been submitted for publication to Medical Physics. Devin Baillie, B. G. Fallone, S. Steciw, “Design and simulation of a short, variable-energy 4 to 10 MV linear accelerator waveguide”.

5.1 Introduction

In this chapter, the 10 MV linac, as presented in chapter 4, is modified to produce x-ray energies of 4, 6, and 8 MV in addition to the 10 MV x-rays produced in the previous study. The 10 MV linac is a 7.5 MW Klystron driven S-band linear accelerator that was designed to be a drop-in replacement for the Varian 600C currently used in the Alberta linac-MR. The redesign presented in this chapter will allow the Alberta linac-MR to deliver optimal treatments to patients, regardless of tumor location or patient size. Additionally, this linac offers the potential to produce a multi-energy linac that is simpler and less expensive than current conventional high energy linacs, making higher energies affordable for the developing world that may not currently have access to those capabilities

5.2 Methods

In order to design a variable energy linear accelerator, the research presented in this chapter was based on the 10 MV linear accelerator design outlined in chapter 4, with some minor modifications to enable lower energies. The previous accelerator was designed by matching the cavity parameters from a published breakdown study (1), and using the resulting accelerating cavity as the basis for designing a full waveguide. This provided confidence that the published breakdown threshold would be applicable to the waveguide, since a theoretical determination of a breakdown threshold was not possible. The nose cone dimensions are the relevant dimensions for breakdown, so these were kept fixed for the work in this chapter. Compared to the earlier work, the port has now been moved from the second accelerating cavity (AC2 in Fig. 5.1) to the fourth accelerating cavity (AC4 in Fig. 5.1) to reduce electron beam asymmetry, and to make the waveguide an exact drop-in replacement for the 600C used in the Alberta linac-MR system. In addition, the first coupling cavity (CC1 in Fig. 5.1) shift has been removed to maximize the RF field strength in the first accelerating cavity (AC1 in Fig. 5.1) relative to the field strength in the rest of the cavities to ensure electron capture at the lowest possible power level. The electron gun used in chapters 3 and 4 was a phenomenological model emulating the Varian 600C accelerator. For the work presented in this chapter the actual dimensions of a Varian VTC6364 (2,3) electron gun were used and simulated in COMSOL Multiphysics.

Each cavity was individually tuned to resonate at the operating frequency of 2.997 GHz after which the entire waveguide resonates at that frequency. As explained in

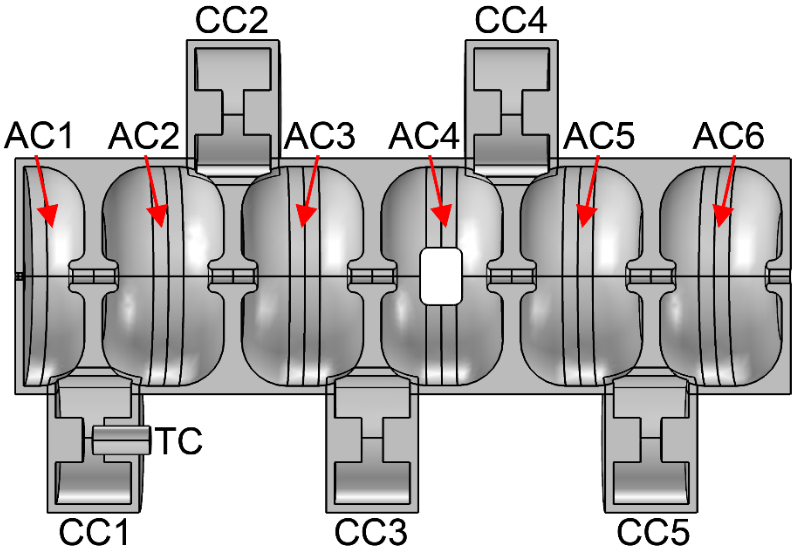

Figure 5.1: A cutaway view of the linear accelerator waveguide. The labeled components are: accelerating cavities (AC1 to AC6), coupling cavities (CC1 to CC6), and tuning cylinder (TC). The electron gun and x-ray target are not shown, and would be located to the left of AC1 and to the right of AC6, respectively.

section 2.3.1, an individual cavity behaves as an RLC (resistor, inductor, and capacitor) circuit (4), where the resistance is determined by the conductivity of the cavity wall, the inductance by the outer radius and the capacitance by the accelerating cavity nose cone or coupling cavity post dimensions. The resonant frequency of an RLC circuit is given by $1/\sqrt{LC}$, so the resonant frequency of any cavity can be increased by reducing the cavity diameter or reducing the nose cone or post length or size, or decreased by increasing the cavity diameter or increasing the nose cone or post length or size. Each accelerating cavity (AC1 to AC6 in Fig. 5.1) was individually tuned by adjusting the cavity diameter, and each coupling cavity (CC1 to CC6 in Fig. 5.1) by adjusting the post length, to resonate at the operating frequency of 2.997 GHz. It should be noted that adjusting the diameter of an accelerating cavity affects the size of the iris between the accelerating and adjacent coupling cavities, which affects their resonant frequency, therefore the accelerating cavities were tuned first, followed by the coupling cavities.

The RF power reflected at the port must be minimized in order to maximize the RF field strength within the waveguide. This was done by scaling the port size (keeping the aspect ratio fixed), after which retuning AC4, CC3 and CC4 was required. The power reflected at the port was calculated for each port size, and the port size which minimized the reflections was used for the remaining simulations.

Reducing the x-ray energy from 10 MV was accomplished by controlling the input RF power to reduce the field strength in the accelerating cavities, which results in decreased electron beam energy. However, previous work has shown that the RF field strength in AC1 must be precisely controlled to ensure optimal electron capture conditions (5–7). Therefore, as the RF input power in the waveguide was varied to adjust the electron energy, the field strength of the first cavity had to be optimized for each power level. If the RF fields in the first accelerating cavity are too small, no electrons are captured and the target beam current drops to zero (6). Alternatively, if the fields are too large, the electron energy spectrum exiting the waveguide incident on the target is very broad, which results in increased low energy photon production (6,7). The lack of first coupling cavity offset, necessary for electron capture in the low energy cases, was expected to cause sub-optimal electron energy distributions for the higher energy cases. In order to control the first cavity fields independently, a 10 mm diameter tuning cylinder of high conductivity, oxygen free copper (TC in Fig. 5.1) of variable depth was added to CC1, along the axis of the cavity. Tuning cylinders perpendicular to the axis of the cavity were attempted first, followed by a 5 mm diameter tuning cylinder along the axis, but these were more sensitive to the depth of the cylinder, and required an extremely fine mesh to resolve to sufficient accuracy, the requirements of which exceeded available RAM. This allowed control of the electron capture conditions for any input power above the minimum allowed by the capture threshold.

For the work in this chapter, COMSOL Multiphysics version 5.1 (Burlington, Massachusetts, USA) was used for the waveguide optimization and RF field calculations. The mesh density was increased from the work presented in chapters 3 and 4 (6,7) in order to reduce the imperfections in the tuning which were evident in the results (7). Each full model consisted of approximately 700,000 3rd order isoparametric tetrahedral mesh elements (compared to ~100,000 in previous work) using cubic interpolation functions. The elements had an element volume ratio of 6.3×10^{-5} and a minimum element quality of 0.1. Each RF solution took approximately 1.5 hours on a computer with four 12 core 2.2 GHz AMD Opteron 6174 CPUs and 224 GB of RAM.

The electron trajectories through each RF field solution were computed for each waveguide RF field solution. The COMSOL RF solution in the central beam tube was first interpolated onto a rectilinear grid and then used in PARMELA, (Los Alamos National Laboratory, NM) to compute the electron beam phase space exiting the waveguide incident on the x-ray target. The PARMELA phase increment of 3.6° per step was unchanged from the previous studies (6,7), but the reference particle was started at a phase of 95°. This is necessary because of the lower electron beam energy of the Varian VTC6364 (2,3), 9.5 kV (compared with 30.8 kV in the earlier simulations). The electron gun phase space was used to generate 4×10^6 particles uniformly distributed over two RF periods which were injected into the waveguide. The electrons were then propagated through the RF fields using PARMELA in order to compute the electron phase space incident on the target. The leading and trailing electron half-bunches were discarded during post-processing to eliminate simulation end effects, and the results are used for comparison and for input into Monte Carlo simulations. The leading and trailing bunches serve to focus the central bunch longitudinally in the waveguide, and failing to model them can result in inaccurate mean energies and spectrum widths. Because the leading and trailing half bunches are not longitudinally focused by additional bunches ahead or behind, failure to discard them can result in similar inaccuracies.

Achieving a particular x-ray energy involved simultaneously optimizing the RF input power to the waveguide and the first accelerating cavity field strength. Beginning with a 7.5 MW input power, the tuning cylinder depth was increased until an electron energy FWHM of 3% of the electron beam mean energy was obtained, consistent with what is currently used clinically (8). Once the optimal cylinder depth with 7.5 MW input power was achieved, the input power was progressively reduced in increments of 5%. For each reduction, the tuning cylinder was progressively withdrawn until the electron energy FWHM rose above 3% of the electron beam mean energy, after which the input power was again reduced. This removed the need to simulate all cylinder depths for each power level. Interpolation based on the electron beam energy was then used to obtain the RF input power required for each of the desired energies: 4, 6, 8, and 10 MV. A nominal energy of 4, 6, or 10 MV corresponds to a mean electron energy of 4.3, 5.7, and 10.5 MeV, respectively (8). No similar comparison was available for an 8 MV photon beam, so a mean energy of 8 MeV was used. Once the cylinder depths and input power levels were determined for the desired energies, the PARMELA simulations were repeated until 4.5×10^7 particles exiting the waveguide were obtained for Monte Carlo.

Monte Carlo simulations were then performed to calculate dose distributions in a water phantom for each beam energy. A 10 MV linac head, without flattening filter, was simulated according to Varian specifications (9), including target, primary collimator, monitor chamber, mirror, and jaws. The Monte Carlo simulations are performed flattening-filter-free, as this is the intended mode of operation of the linac-MR system. For each of the lower energies, the 10 MV x-ray target was replaced with a 4, 6, or 8 MV target. The x-ray targets as defined in the Varian specifications are not thick enough to fully stop the electron beam. Instead, the remaining electron stops inside the flattening filter. Because the linac head was simulated flattening-filter-free, the targets were based on Varian specifications, with the thickness increased to the full CSDA range of the maximum electron energy present in the beam. For each energy, BEAMnrc was used with 1×10^8 input electrons for each field size of 5×5, 10×10, 20×20, and 40×40 cm^2. The results of the BEAMnrc simulations were then used to create 1.5×10^{10} particles for input into DOSXYZnrc simulations to calculate depth dose curves for 5×5, 10×10, and 20×20 cm^2 field sizes, and x and y beam profiles were calculated at 10 cm depth for the 40×40 cm^2 field sizes. The depth dose curves were computed using 5×5×1 mm ($x \times y \times z$) voxels until 3.5 cm depth, and 5×5×5 mm voxels after; while the beam profiles were computed using 3.5×3.5×5 mm voxels across the beam. The BEAMnrc and DOSXYZnrc simulations used directional bremsstrahlung splitting with NBRSPL set to 100 to improve accuracy and computational time. The BEAMnrc and DOSXYZnrc PDD simulations were repeated using electron distributions emulating Varian linacs, as published by Sheik-Bagheri and Rogers (8) for the 4, 6, and 10 MV cases for comparison. No electron distribution is available for comparison for the 8 MV case.

5.3 Results and Discussion

The presence of an input port affected the resonant frequency of the accelerating cavity, which had to be accounted for during tuning. With the port in the fourth accelerating cavity, the cavity dimensions after retuning the affected cavities are shown in table 5.1. Figure 5.2 shows how S_{11} (the fraction of power reflected) changed as the port size was adjusted. Without adjusting the port size, S_{11} was -4.883 dB, while the reflected power was a minimum when a linear decrease of 10% of the original port dimensions of 17.12 by 23.54 mm with a 3.4 mm radius of curvature at the corners is used, which resulted in an S_{11} of -7.062 dB. This was lower than the S_{11} from previous work of -5.11 dB, so the resulting energies are expected to be similar to or slightly higher

Cavity number	AC radius	CC post length
1	39.34*	9.647
2	39.34	9.647
3	39.34*	9.650 (9.649)
4	39.10 (39.17)	9.650 (9.649)
5	39.34*	9.622*
6	39.36*	N/A

Table 5.1: Accelerating cavity radii and coupling cavity post lengths after waveguide tuning with the port in AC4. Dimensions with a * were unaffected by retuning. Dimensions in brackets were the result of retuning after the port size optimization. The AC radii are measured from the central axis to the outside of the cavity.

than in the previous work. The retuned waveguide dimensions after optimizing the port size are shown in brackets in table 5.1.

The first half cavity fields determined the electron spectrum width and were controlled by inserting a tuning cylinder. Without inserting the tuning cylinder, the waveguide model produced an electron beam with mean energy of 10.58 MeV and an energy FWHM of 2.43 MeV, or 23% of the mean. Clinically used accelerators typically use an electron beam with an energy FWHM of 3% of the mean energy (8). Moving the tuning cylinder in Fig. 5.3 to a depth of 6.94 mm resulted in a FWHM that is 2.9% of the mean energy of 10.52 MeV. This is closely matched to linacs currently used clinically, which operate with a mean electron energy of 10.5 MeV and an energy FWHM of 3% (8).

The electron beam energy was controlled by reducing the RF input power to the waveguide. Reducing the RF input power with the tuning cylinder inserted resulted in a decrease in the mean electron energy (Fig. 5.4), but also a loss of beam current (Fig. 5.5). When the tuning cylinder is progressively retracted and the input power decreased any desired energy level could be achieved, while maintaining both the 3% FWHM and an acceptable beam current. Table 5.2 shows the input power and cylinder depths required

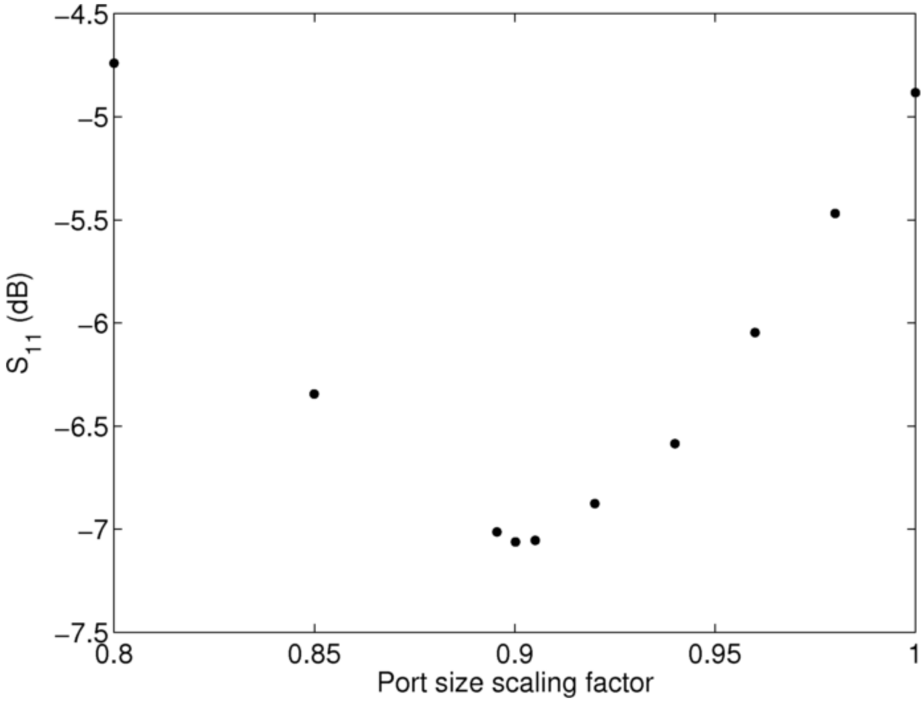

Figure 5.2: The fraction of power reflected at the waveguide input port as the size of the port was varied. The initial port dimensions (scaling factor = 1) were 17.12 mm by 23.54 mm with a 3.4 mm radius of curvature at the corners.

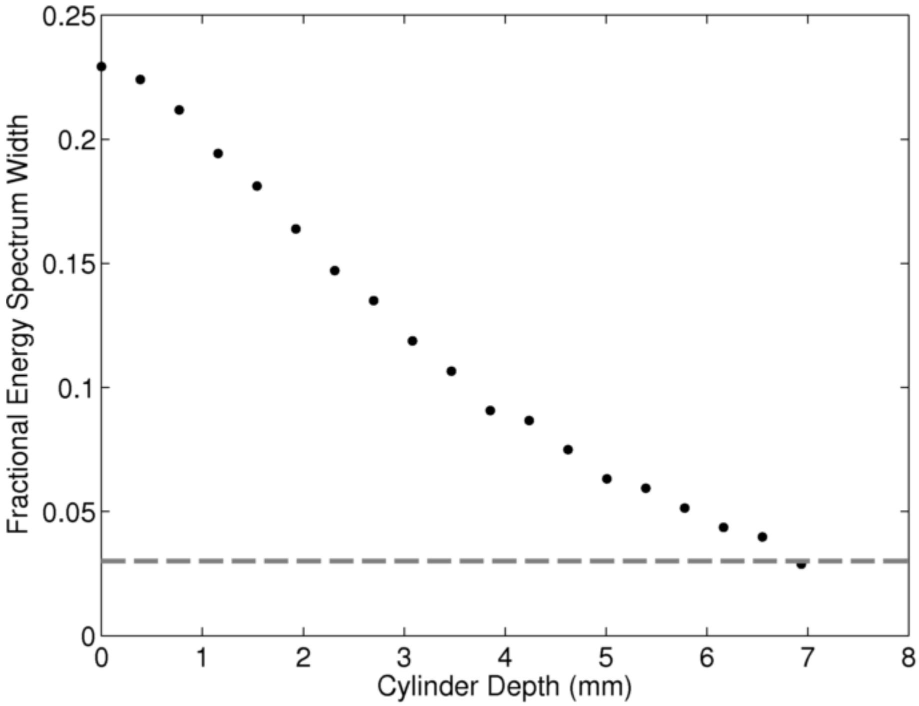

Figure 5.3: The electron energy FWHM as a fraction of the mean electron energy as the tuning cylinder (TC in Fig. 5.1) was inserted into CC1. The red dashed line represents the 3% FWHM that is currently used clinically.

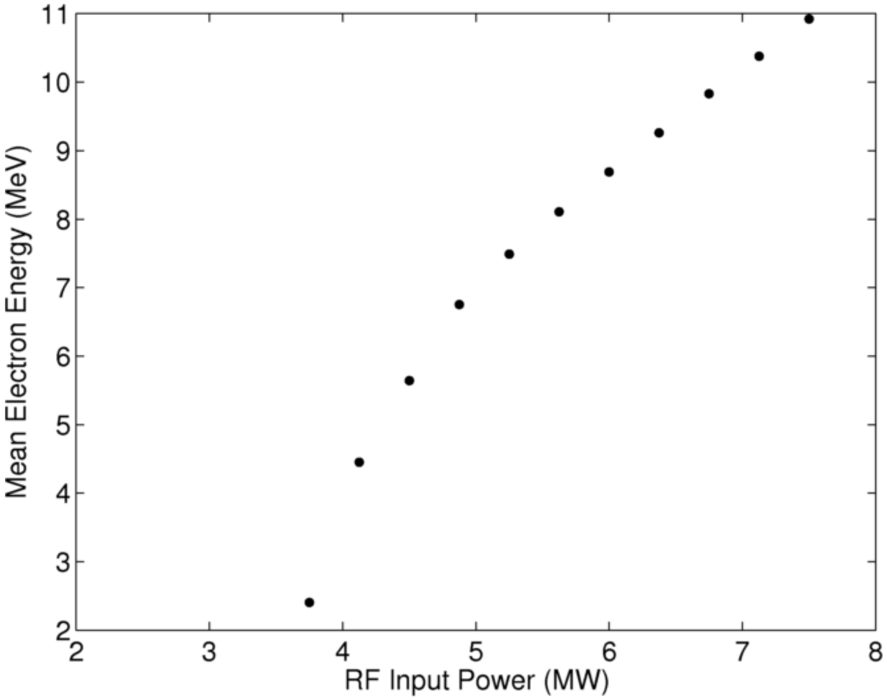

Figure 5.4: The mean electron energy as the RF input power was reduced while the tuning cylinder position was fixed at a depth of 6.9 mm. For input power less than 3.7 MW, no electrons were captured (see Fig. 5.5).

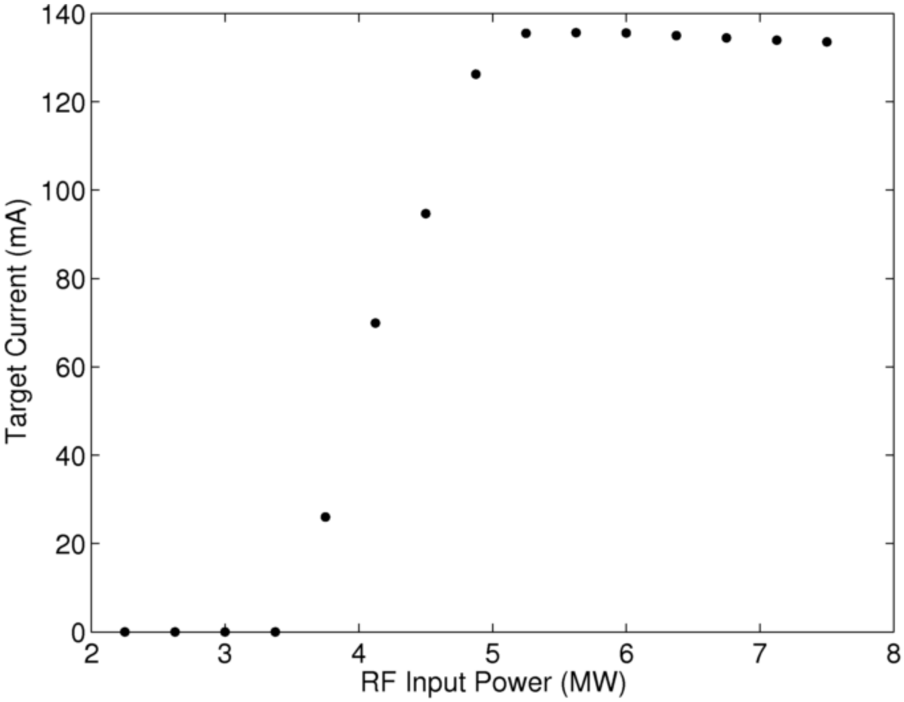

Figure 5.5: The target current as the RF input power was reduced while the tuning cylinder position was fixed at a depth of 6.9 mm.

to achieve the target energies, along with the resulting beam currents. The 10 MV beam current, 133.7 mA was higher than that measured on an existing clinical Varian linacs, 40 mA, while the 6 MV beam current, 118.9 mA, was slightly lower than that measured on an existing Varian clinical linac, 134 mA. The optimized axial field magnitudes in AC1 are included in table 5.2 for interest and completeness. For clarity, only the results corresponding to the desired energies are presented in table 5.2, though any intermediate energy is also easily obtainable. The decision to produce 4, 6, 8, and 10 MV beams was somewhat arbitrary, however these energies illustrate that the production of any energies in this range is achievable by varying the cylinder depth and input power.

Figure 5.6 shows the depth dose curves for 5, 10, and 20 cm square fields compared (for 4, 6, 8, and 10 MV) against those produced by an identical simulation using the electron beam parameters published by Sheik Bagheri and Rogers (8) (for 4, 6, and 10 MV). In all cases with a comparison, the calculated depth of maximum dose agreed within 1.5 mm and the ratio of doses at 10 and 20 cm depth agreed in each case within 1%. Figure 5.7 shows the beam profiles for a 40 cm square field for each energy. As these simulations were flattening-filter-free, the dose near the edges is expected to be reduced, and that is what was observed.

Nominal energy (MV)	Input power (MW)	Tuning cylinder depth (mm)	Mean electron energy (MeV)	FWHM (% of mean)	Beam current (mA)	AC1 axial field strength (MV/m)
10	7.50	6.9	10.52	2.88	133.7	22.32
8	5.37	3.7	7.99	2.17	131.8	22.89
6	3.70	0.6	5.73	2.27	118.9	24.85
4	2.53	0	4.32	2.32	115.4	17.68

Table 5.2: Input powers and tuning cylinder depths required to produce each nominal x-ray energy, along with resulting mean energies, FWHMs, x-ray target beam currents, and AC1 mean axial field strengths.

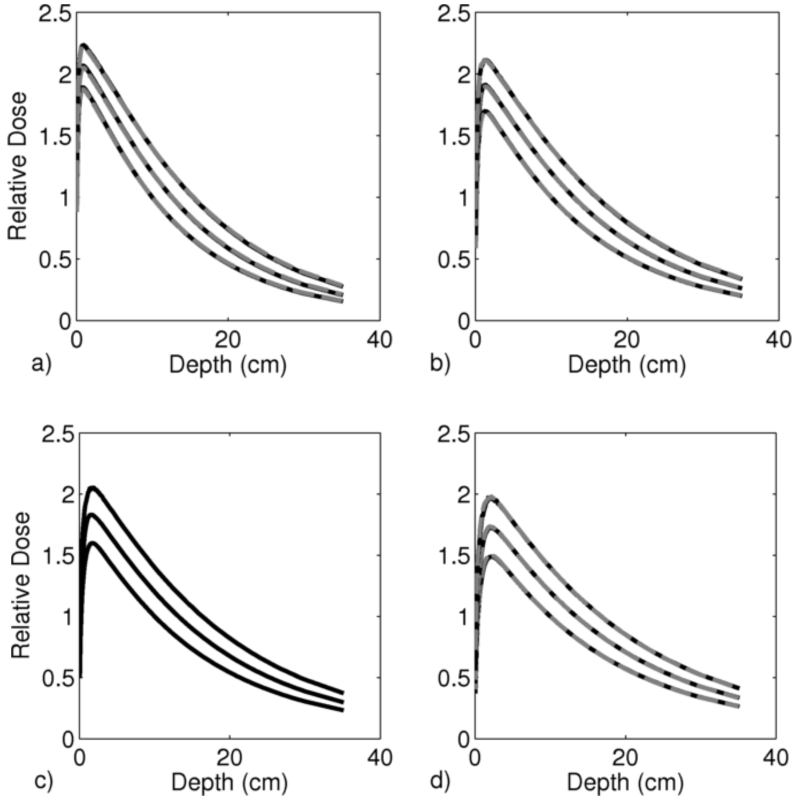

Figure 5.6: Depth dose curves for (a) 4 MV, (b) 6 MV, (c) 8 MV, and (d) 10 MV for 5, 10, and 20 cm square fields. Each field size was normalized at 10 cm depth and then independently scaled for clarity (20 cm on top, followed by 10 cm, and 5 cm on the bottom). Solid black is the new linac design, dashed grey (for energies other than 8 MV) are that produced using published electron energy spectra.

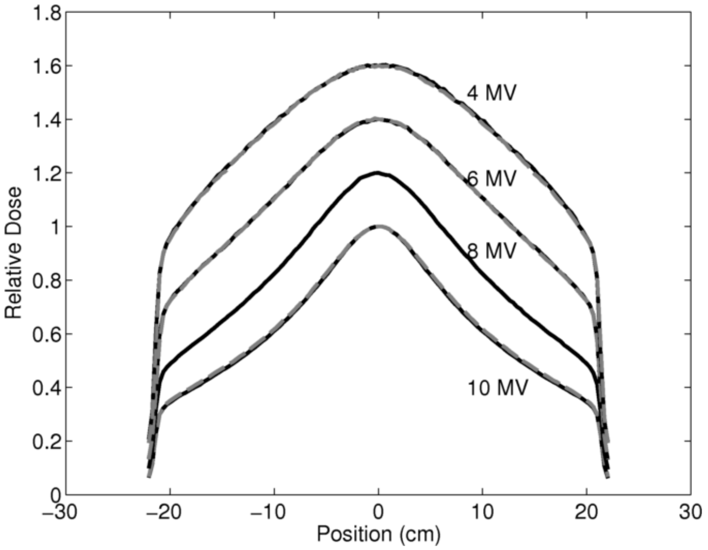

Figure 5.7: Beam profiles for 40 cm square fields for each energy. Each energy was normalized to the central axis dose and then independently scaled for clarity.

5.4 Conclusions

The goal of the research, to design and simulate a linear accelerator waveguide capable of producing any photon energy between 4 and 10 MV, has been achieved. This waveguide is 27.5 cm in length, the same length as the Varian 600C currently used in the linac-MR at the Cross Cancer Institute. A variable-depth tuning cylinder added to the first coupling cavity allows the RF field strength in the first accelerating cavity to be precisely controlled, allowing a clinically useful energy spectrum and beam current to be obtained at each energy. To demonstrate the ability to produce specific energies, the photon depth dose curves for published electron spectra for 4, 6, and 10 MV have been matched.

This newly designed, variable-energy linac will enable linac-MR systems to treat with any energy from 4 to 10 MV. This will further improve treatments delivered using linac-MR systems by allowing the selection of the optimal energy for each particular patient and treatment site, leading to better patient outcomes.

5.5 References

1. Tanabe E. Voltage Breakdown in S-Band Linear Accelerator Cavities. IEEE Trans Nucl Sci. 1983 Aug;30(4):3551–3.

2. Vaughan JRM. Synthesis of the Pierce gun. IEEE Trans Electron Devices. 1981 Jan;28(1):37–41.

3. Constantin DE, Fahrig R, Keall PJ. A study of the effect of in-line and perpendicular magnetic fields on beam characteristics of electron guns in medical linear accelerators. Med Phys. 2011 Jul 1;38(7):4174–85.

4. Nagle DE, Knapp EA, Knapp BC. Coupled Resonator Model for Standing Wave Accelerator Tanks. Rev Sci Instrum. 2004 Dec 29;38(11):1583–7.

5. St. Aubin J, Steciw S, Kirkby C, Fallone BG. An integrated 6 MV linear accelerator model from electron gun to dose in a water tank. Med Phys. 2010;37:2279–88.

6. Baillie D, Aubin JS, Fallone BG, Steciw S. Feasibility of producing a short, high energy s-band linear accelerator using a klystron power source. Med Phys. 2013;40(4):41713.

7. Baillie D, Aubin JS, Fallone BG, Steciw S. FEM design and simulation of a short, 10 MV, S-band Linac with Monte Carlo dose simulations. Med Phys. 2015 Apr 1;42(4):2044–53.

8. Sheikh-Bagheri D, Rogers DWO. Sensitivity of megavoltage photon beam Monte Carlo simulations to electron beam and other parameters. Med Phys. 2002;29:379.

9. Varian Medical Systems Monte Carlo Data Package. Available under non-disclosure-agreement from Varian Medical Systems;

6. Summary and Conclusions

Linac-MR devices being developed around the world (1–5) offer the potential to revolutionize image-guided external-beam radiation therapy through the use of MRI to provide real-time, 3D imaging during radiation therapy treatments. The excellent soft-tissue contrast offered by MRI (6) enables linac-MR systems to treat tumors which are not treatable with x-ray based methods of IGRT (7). MR based imaging allows the tumor to be directly imaged, rather than tracking a surrogate for the tumor, as is the case with fiducials. Its imaging doesn’t involve ionizing radiation (which x-ray based imaging does), or require invasive implantation of internal fiducial markers.

Current linac-MR systems are designed using either single-, low-energy linacs which produce 6 (1,2,5) or 8 (3) MV x-rays or cobalt-60(4) as the radiation source. While these energies are suitable for many radiation therapy treatments, there is room for improvement. Many patients can benefit from either higher (8,9) or lower (10) energies, depending on the treatment site. Integrating current multi-energy linacs with linac-MR devices is challenging due the additional complexity and orientation of the waveguide with respect to the imaging magnetic field. The research presented in this thesis aims to design a tunable linac capable of producing x-ray energies from 4 to 10 MV with the long term goal of enabling linac-MR systems to deliver more optimal treatments for a greater number of patients.

This research began with an investigation of the feasibility of producing a 10 MV photon beam using a linac waveguide the same length as that currently used to produce 6 MV (11). A previously designed FEM model emulating the existing waveguide (12) was used for this purpose. The RF input power to the simulated waveguide, and the field strength required to accelerate electrons to 10 MeV was calculated. There was a 30% safety margin between the calculated RF fields and the field strengths which are likely result in breakdown (13). Monte Carlo simulations showed that the photon beam energy was very similar to that produced by clinically used 10 MV linacs.

The next stage of the project, once feasibility had been established, was to design the 10 MV waveguide itself (14). This stage began with the design of a single accelerating cavity based on a published breakdown study (15); this allowed the published breakdown threshold to be directly applicable to the new cavity. The new cavity was used as the basis of a full accelerator model, which was then tuned and optimized until it produced an x-ray beam equivalent to clinically used 10 MV linacs. The RF field strength in the waveguide was more than 12% below the threshold. Advances in vacuum technology and waveguide surface processing since the publication of the breakdown study suggest that the published threshold is extremely conservative.

The final stage of the project involved modifying the newly designed 10 MV waveguide to produce a variety of x-ray energies from 4 to 10 MV. This was accomplished by reducing the RF power supplied to the waveguide. In order to maintain optimal electron capture conditions, a tuning cylinder was added to allow the RF fields in the first accelerating cavity to be independently controlled. Though only x-ray energies of 4, 6, 8, and 10 MV were presented in this thesis, by optimizing the RF input power and the cylinder position, any x-ray energy in this range can be produced.

6.1 Next Steps

While the accelerator design has been completed and described in this thesis, there are still engineering aspects to be investigated before the new linac can be constructed and put into service.

6.1.1 Magnetic field effects

The effect of magnetic fields on the linac have been studied for the currently used Varian 600C linac (16–18). While the effects and shielding requirements are not expected to differ significantly for the newly designed linac, a similar study is required to verify that the linac will operate as expected within the magnetic field. The fringe magnetic fields from the MRI could be added to the electron gun and waveguide simulations to determine the shielding requirements for the new linac when used with the linac-MR.

6.1.2 Geometric tolerances

The shape of the linac waveguide determines how well it can function as an accelerator. Manufacturing tolerances can result in slight variations in the dimensions which could affect the operation of the waveguide. An FEM study could be conducted by adding random variation to the waveguide dimensions in order to determine geometric tolerances, and the effect of imperfections on the x-ray beams produced.

6.1.3 Waveguide heating/cooling

Increasing the RF power to the waveguide will result in increased resistive heating in the waveguide walls. If the heat is not dissipated sufficiently, thermal expansion of the copper could detune the waveguide. Energy deposition in the waveguide walls is easily determined from the current FEM waveguide solutions. Heat dissipation and thermal expansion in the walls would require a new FEM simulation modelling the exterior copper structure of the waveguide to determine how much cooling is required in order that thermal expansion does not exceed the geometric tolerances.

6.1.4 Target cooling

The higher beam current and smaller electron focal spot produced by the new linac, particularly at 10 MV, could present challenges to target design due to greatly increased heating. A Monte Carlo study could be used to calculate heat deposition in the x-ray target, followed by an FEM study to model heat dissipation and cooling. If target heating is found to be problematic, one of several approaches could be taken: 1. A redesign of the x-ray target with increased cooling, 2. reducing the duty cycle of the linac, to allow more time for heat to dissipate between pulses, 3. reducing electron beam current to reduce heat deposition, or 4. developing a method to de-focus the electron beam, spreading out the focal spot and increasing the area over which heat is deposited.

6.1.5 Breakdown verification

While the best efforts were made to produce a cavity with a known breakdown threshold, a physical breakdown study should be performed to be certain. This would involve constructing a single cavity based on the published dimensions and increasing the RF power until arcing occurs. The measured breakdown threshold could then be compared against the simulated RF field strength required to produce 10 MV x-rays.

6.1.6 Construction

The final step is to construct a waveguide based on the optimized dimensions in order to compare the electron beam and x-ray output to the simulation results.

Modifications could then be made to account for any differences between simulation and measurement, and a final waveguide geometry produced.

Once constructed, the new variable-energy linac will enable linac-MR systems to treat with the optimal energy for any patient or tumor site, which will further improve treatments delivered using linac-MR systems. This will result in less radiation dose to healthy tissue without compromising dose to the tumor, which is expected reduce healthy tissue complications and lead to better patient outcomes.

6.2 References

1. Fallone BG. The Rotating Biplanar Linac–Magnetic Resonance Imaging System. Semin Radiat Oncol. 2014 Jul;24(3):200–2.

2. Keall PJ, Barton M, Crozier S. The Australian Magnetic Resonance Imaging–Linac Program. Semin Radiat Oncol. 2014 Jul;24(3):203–6.

3. Crijns S, Raaymakers B. From static to dynamic 1.5 T MRI-linac prototype: impact of gantry position related magnetic field variation on image fidelity. Phys Med Biol. 2014;59(13):3241.

4. Mutic S, Dempsey JF. The ViewRay System: Magnetic Resonance–Guided and Controlled Radiotherapy. Semin Radiat Oncol. 2014 Jul;24(3):196–9.

5. Heid O, Kleemann M, Heller J. Integrated MRI-LINAC Radiotherapy Machine. Proc Int Soc Mag Reson Med. 2015;23:3068.

6. Aisen A, Martel W, Braunstein E, McMillin K, Phillips W, Kling T. MRI and CT evaluation of primary bone and soft-tissue tumors. Am J Roentgenol. 1986 Apr 1;146(4):749–56.

7. Lagendijk JJW, van Vulpen M, Raaymakers BW. The development of the MRI linac system for online MRI-guided radiotherapy: a clinical update. J Intern Med. 2016 May 1;n/a-n/a.

8. Pirzkall A, Carol MP, Pickett B, Xia P, Roach III M, Verhey LJ. The effect of beam energy and number of fields on photon-based IMRT for deep-seated targets. Int J Radiat Oncol. 2002 Jun 1;53(2):434–42.

9. Pasler M, Georg D, Wirtz H, Lutterbach J. Effect of Photon-Beam Energy on VMAT and IMRT Treatment Plan Quality and Dosimetric Accuracy for Advanced Prostate Cancer. Strahlenther Onkol. 2011 Nov 29;187(12):792–8.

10. Ekstrand KE, Barnes WH. Pitfalls in the use of high energy X rays to treat tumors in the lung. Int J Radiat Oncol Biol Phys. 1990 Jan;18(1):249–52.

11. Baillie D, Aubin JS, Fallone BG, Steciw S. Feasibility of producing a short, high energy s-band linear accelerator using a klystron power source. Med Phys. 2013;40(4):41713.

12. St. Aubin J, Steciw S, Kirkby C, Fallone BG. An integrated 6 MV linear accelerator model from electron gun to dose in a water tank. Med Phys. 2010;37:2279–88.

13. Wang JW, Loew GA. Field emission and rf breakdown in high-gradient room temperature linac structures. Stanford Univ., Stanford Linear Accelerator Center, CA (US); 1997.

14. Baillie D, Aubin JS, Fallone BG, Steciw S. FEM design and simulation of a short, 10 MV, S-band Linac with Monte Carlo dose simulations. Med Phys. 2015 Apr 1;42(4):2044–53.

15. Tanabe E. Voltage Breakdown in S-Band Linear Accelerator Cavities. IEEE Trans Nucl Sci. 1983 Aug;30(4):3551–3.

16. St. Aubin J, Santos D, Steciw S, Fallone BG. Effect of longitudinal magnetic fields on a simulated in-line 6 MV linac. Med Phys. 2010;37:4916–23.

17. St. Aubin J, Steciw S, Fallone BG. Effect of transverse magnetic fields on a simulated in-line 6 MV linac. Phys Med Biol. 2010;55:4861–9.

18. Santos DM, Aubin JS, Fallone BG, Steciw S. Magnetic shielding investigation for a 6 MV in-line linac within the parallel configuration of a linac-MR system. Med Phys. 2012;39(2):788–797.

Bibliography

Pasler M, Georg D, Wirtz H, Lutterbach J. Effect of Photon-Beam Energy on VMAT and IMRT Treatment Plan Quality and Dosimetric Accuracy for Advanced Prostate Cancer. Strahlenther Onkol. 2011 Nov 29;187(12):792–8.

Followill DS, Nüsslin F, Orton CG. IMRT should not be administered at photon energies greater than 10 MV. Med Phys. 2007;34(6):1877.

Crookes W. The Bakerian Lecture: On the Illumination of Lines of Molecular Pressure, and the Trajectory of Molecules. Philos Trans R Soc Lond. 1879 Jan 1;170:135–64.

On a New Kind of Rays. Nature. 1896 Jan 23;53(1369):274–6.

Grubbé EH. Priority in the Therapeutic Use of X-rays. Radiology. 1933 Aug 1;21(2):156–62.

Kerst DW. Acceleration of Electrons by Magnetic Induction. Phys Rev. 1940 Nov 1;58(9):841–841.

Ekstrand KE, Barnes WH. Pitfalls in the use of high energy X rays to treat tumors in the lung. Int J Radiat Oncol Biol Phys. 1990 Jan;18(1):249–52.

Jones D. ICRU report 50: prescribing, recording and reporting photon beam therapy. ICRU Bethesda USA. 1994;

Wambersie A, Landgerg T. ICRU report 62: prescribing, recording and reporting photon beam therapy (supplement to ICRU Report 50). ICRU Bethesday USA. 1999;

Mackie TR, Holmes T, Swerdloff S, Reckwerdt P, Deasy JO, Yang J, et al. Tomotherapy: a new concept for the delivery of dynamic conformal radiotherapy. Med Phys. 1993;20(6):1709–1719.

Yu CX. Intensity-modulated arc therapy with dynamic multileaf collimation: an alternative to tomotherapy. Phys Med Biol. 1995;40(9):1435.

Otto K. Volumetric modulated arc therapy: IMRT in a single gantry arc. Med Phys. 2008 Jan 1;35(1):310–7.

Walter C, Boda-Heggemann J, Wertz H, Loeb I, Rahn A, Lohr F, et al. Phantom and in-vivo measurements of dose exposure by image-guided radiotherapy (IGRT): MV portal images vs. kV portal images vs. cone-beam CT. Radiother Oncol. 2007 Dec;85(3):418–23.

Morin O, Gillis A, Chen J, Aubin M, Bucci MK, Roach III M, et al. Megavoltage cone-beam CT: System description and clinical applications. Med Dosim. 2006;31(1):51–61.

Ruchala KJ, Olivera GH, Schloesser EA, Mackie TR. Megavoltage CT on a tomotherapy system. Phys Med Biol. 1999;44(10):2597.

Herman MG. Clinical Use of Electronic Portal Imaging. Semin Radiat Oncol. 2005 Jul;15(3):157–67.

Balter JM, Cao Y. Advanced Technologies in Image-Guided Radiation Therapy. Semin Radiat Oncol. 2007 Oct;17(4):293–7.

Kataria T, Sharma K, Pareek P, Abhishek A, Bisht S, Govardhan H, et al. Frame-based radiosurgery: Is it relevant in the era of IGRT? Neurol India. 2013;61(3):277.

Shirato H, Shimizu S, Kitamura K, Nishioka T, Kagei K, Hashimoto S, et al. Four-dimensional treatment planning and fluoroscopic real-time tumor tracking radiotherapy for moving tumor. Int J Radiat Oncol. 2000 Sep;48(2):435–42.

Ford EC, Mageras GS, Yorke E, Rosenzweig KE, Wagman R, Ling CC. Evaluation of respiratory movement during gated radiotherapy using film and electronic portal imaging. Int J Radiat Oncol. 2002 Feb 1;52(2):522–31.

Litzenberg D, Dawson LA, Sandler H, Sanda MG, McShan DL, Ten Haken RK, et al. Daily prostate targeting using implanted radiopaque markers. Int J Radiat Oncol. 2002 Mar 1;52(3):699–703.

Willoughby TR, Kupelian PA, Pouliot J, Shinohara K, Aubin M, Roach M, et al. Target localization and real-time tracking using the Calypso 4D localization system in patients with localized prostate cancer. Int J Radiat Oncol Biol Phys. 2006;65(2):528–534.

Langenhuijsen JF, van Lin ENJT, Kiemeney LA, van der Vight LP, McColl GM, Visser AG, et al. Ultrasound-guided transrectal implantation of gold markers for prostate localization during external beam radiotherapy: complication rate and risk factors. Int J Radiat Oncol Biol Phys. 2007 Nov 1;69(3):671–6.

Kim JH, Hong SS, Kim JH, Park HJ, Chang Y-W, Chang AR, et al. Safety and Efficacy of Ultrasound-Guided Fiducial Marker Implantation for CyberKnife Radiation Therapy. Korean J Radiol. 2012;13(3):307–13.

Bhagat N, Fidelman N, Durack JC, Collins J, Gordon RL, LaBerge JM, et al. Complications Associated with the Percutaneous Insertion of Fiducial Markers in the Thorax. Cardiovasc Intervent Radiol. 2010 Dec;33(6):1186–91.

Hennessey H, Valenti D, Cabrera T, Panet-Raymond V, Roberge D. Cardiac embolization of an implanted fiducial marker for hepatic stereotactic body radiotherapy: a case report. J Med Case Reports. 2009;3:140.

Gierga DP, Brewer J, Sharp GC, Betke M, Willett CG, Chen GTY. The correlation between internal and external markers for abdominal tumors: Implications for respiratory gating. Int J Radiat Oncol. 2005 Apr 1;61(5):1551–8.

Poggi MM, Gant DA, Sewchand W, Warlick WB. Marker seed migration in prostate localization. Int J Radiat Oncol. 2003 Aug 1;56(5):1248–51.

Aisen A, Martel W, Braunstein E, McMillin K, Phillips W, Kling T. MRI and CT evaluation of primary bone and soft-tissue tumors. Am J Roentgenol. 1986 Apr 1;146(4):749–56.

Totty WG, Murphy WA, Lee JK. Soft-tissue tumors: MR imaging. Radiology. 1986 Jul 1;160(1):135–41.

Yun J, Mackenzie M, Rathee S, Robinson D, Fallone BG. An artificial neural network (ANN)-based lung-tumor motion predictor for intrafractional MR tumor tracking. Med Phys. 2012 Jul 1;39(7):4423–33.

Yun J, Wachowicz K, Mackenzie M, Rathee S, Robinson D, Fallone BG. First demonstration of intrafractional tumor-tracked irradiation using 2D phantom MR images on a prototype linac-MR. Med Phys. 2013;40(5):51718.

Brix L, Ringgaard S, Sørensen TS, Poulsen PR. Three-dimensional liver motion tracking using real-time two-dimensional MRI. Med Phys. 2014 Apr 1;41(4):42302.

Crijns SPM, Kok JGM, Lagendijk JJW, Raaymakers BW. Towards MRI-guided linear accelerator control: gating on an MRI accelerator. Phys Med Biol. 2011;56(15):4815.

Santanam L, Noel C, Wan H, Kashani R, Rankine LJ, Mazur TR, et al. Adequacy of Gating Margins for Abdominal Tumors of Patients Treated With Real-Time MR Guided Radiation Therapy. Int J Radiat Oncol • Biol • Phys. 2015 Nov 1;93(3):S216–7.

Lamey M, Burke B, Blosser E, Rathee S, De Zanche N, Fallone BG. Radio frequency shielding for a linac-MRI system. Phys Med Biol. 2010;55(4):995.

Lamey M, Yun J, Burke B, Rathee S, Fallone BG. Radio frequency noise from an MLC: a feasibility study of the use of an MLC for linac-MR systems. Phys Med Biol. 2010;55(4):981.

Constantin DE, Fahrig R, Keall PJ. A study of the effect of in-line and perpendicular magnetic fields on beam characteristics of electron guns in medical linear accelerators. Med Phys. 2011 Jul 1;38(7):4174–85.

St. Aubin J, Steciw S, Fallone BG. Effect of transverse magnetic fields on a simulated in-line 6 MV linac. Phys Med Biol. 2010;55:4861–9.

Santos DM, Aubin JS, Fallone BG, Steciw S. Magnetic shielding investigation for a 6 MV in-line linac within the parallel configuration of a linac-MR system. Med Phys. 2012;39(2):788–797.

Fallone BG, Murray B, Rathee S, Stanescu T, Steciw S, Vidakovic S, et al. First MR images obtained during megavoltage photon irradiation from a prototype integrated linac-MR system. Med Phys. 2009;36(6):2084–8.

Fallone BG. The Rotating Biplanar Linac–Magnetic Resonance Imaging System. Semin Radiat Oncol. 2014 Jul;24(3):200–2.

Keall PJ, Barton M, Crozier S. The Australian Magnetic Resonance Imaging–Linac Program. Semin Radiat Oncol. 2014 Jul;24(3):203–6.

Lagendijk JJW, van Vulpen M, Raaymakers BW. The development of the MRI linac system for online MRI-guided radiotherapy: a clinical update. J Intern Med. 2016 May 1;

Crijns S, Raaymakers B. From static to dynamic 1.5 T MRI-linac prototype: impact of gantry position related magnetic field variation on image fidelity. Phys Med Biol. 2014;59(13):3241.

Heid O, Kleemann M, Heller J. Integrated MRI-LINAC Radiotherapy Machine. Proc Int Soc Mag Reson Med. 2015;23:3068.

Mutic S, Dempsey JF. The ViewRay System: Magnetic Resonance–Guided and Controlled Radiotherapy. Semin Radiat Oncol. 2014 Jul;24(3):196–9.

Page BR, Hudson AD, Brown DW, Shulman AC, Abdel-Wahab M, Fisher BJ, et al. Cobalt, Linac, or Other: What Is the Best Solution for Radiation Therapy in Developing Countries? Int J Radiat Oncol. 2014 Jul 1;89(3):476–80.

ViewRay unveils plans for MRIdian Linac - MedicalPhysicsWeb [Internet]. Available from: http://medicalphysicsweb.org/cws/article/research/64322

Tanabe E. Voltage Breakdown in S-Band Linear Accelerator Cavities. IEEE Trans Nucl Sci. 1983 Aug;30(4):3551–3.

Griffiths DJ. Introduction to Electrodynamics. Prentice Hall; 1999.

Hoppe DJ. Impedance Boundary Conditions In Electromagnetics. 1st ed. CRC Press; 1995. 262 p.

Wangler TP. Rf Linear Accelerators. Wiley-VCH; 2008. 476 p.

Nagle DE, Knapp EA, Knapp BC. Coupled Resonator Model for Standing Wave Accelerator Tanks. Rev Sci Instrum. 2004 Dec 29;38(11):1583–7.

Agarwal A, Lang J. Foundations of Analog and Digital Electronic Circuits. 1 edition. Amsterdam ; Boston: Morgan Kaufmann; 2005. 1008 p.

Wang JW. RF properties of periodic accelerating structures for linear colliders. SLAC-Report-339; 1989.

Wang J, Loew G. Field emission and rf breakdown in high-gradient room-temperature linac structures. SLAC-PUB-7684; 1997.

Tanabe E, Wang J, Loew G. Voltage Breakdown at X-band and C-band Frequencies. In: Linear Accelerator Conference Proceedings. 1986. p. 458–460.

Kilpatrick WD. Criterion for Vacuum Sparking Designed to Include Both rf and dc. Rev Sci Instrum. 1957 Oct;28(10):824–6.

Baillie D, Aubin JS, Fallone BG, Steciw S. Feasibility of producing a short, high energy s-band linear accelerator using a klystron power source. Med Phys. 2013;40(4):41713.

Loew GA, Wang JW. Field emission and rf breakdown in copper linac structures. Part Accel. 1989;30(SLAC-PUB-5059):225–230.

Dolgashev V, Tantawi S, Higashi Y, Spataro B. Geometric dependence of radio-frequency breakdown in normal conducting accelerating structures. Appl Phys Lett. 2010;97:171501.

Jin J. The Finite Element Method in Electromagnetics. Wiley; 1993.

Boris N. Delaunay,(1934)“Sur la Sphere” Vide. Izv Akad Nauk SSSR. :793–800.

Schenk O, Gärtner K. Solving unsymmetric sparse systems of linear equations with PARDISO. Future Gener Comput Syst. 2004 Apr 1;20(3):475–87.

Hand LN, Finch JD. Analytical Mechanics. 1 edition. Cambridge ; New York: Cambridge University Press; 1998. 592 p.

Jackson JD. Classical Electrodynamics. Wiley; 1999.

Young LM BJH. Parmela. LA-UR-96-1835, Rev; 2005.

Kawrakow I, Rogers DWO. The EGSnrc code system. NRC Rep PIRS-701 NRC Ott. 2000;

Nelson WR, Hirayama H, Rogers DW. EGS4 code system. Stanford Linear Accelerator Center, Menlo Park, CA (USA); 1985.

Lewis HW. Multiple scattering in an infinite medium. Phys Rev. 1950;78(5):526.

Kawrakow I. Accurate condensed history Monte Carlo simulation of electron transport. I. EGSnrc, the new EGS4 version. Med Phys. 2000;27(3):485–498.

Bielajew AF, Rogers DWO. Variance-Reduction Techniques. In: Jenkins TM, Nelson WR, Rindi A, editors. Monte Carlo Transport of Electrons and Photons. Springer US; 1988. p. 407–19. (Ettore Majorana International Science Series).

El-Ashmawy M, Uesaka M, Iijima H, Imai T, Quyet NH. Overall Quality Comparison of C-Band and X-Band Medical Linacs. In: The 14th symposium on Accelerator Science and Technology, Tsukuba, Japan. 2003.

Wang JW, Loew GA. Field emission and rf breakdown in high-gradient room temperature linac structures. Stanford Univ., Stanford Linear Accelerator Center, CA (US); 1997.

St. Aubin J, Steciw S, Fallone BG. The design of a simulated in-line side-coupled 6 MV linear accelerator waveguide. Med Phys. 2010;37:466–76.

St. Aubin J, Steciw S, Kirkby C, Fallone BG. An integrated 6 MV linear accelerator model from electron gun to dose in a water tank. Med Phys. 2010;37:2279–88.

Rogers DWO, Faddegon BA, Ding GX, Ma CM, We J, Mackie TR. BEAM: A Monte Carlo code to simulate radiotherapy treatment units. Med Phys. 1995;22:503.

Sheikh-Bagheri D, Rogers DWO. Sensitivity of megavoltage photon beam Monte Carlo simulations to electron beam and other parameters. Med Phys. 2002;29:379.

Varian Medical Systems Monte Carlo Data Package. Available under non-disclosure-agreement from Varian Medical Systems;

Koch HW, Motz JW. Bremsstrahlung cross-section formulas and related data. Rev Mod Phys. 1959;31(4):920–955.

Karzmark CJ. Medical Electron Accelerators. McGraw-Hill, Inc., Health Professions Division; 1993.

Vaughan JRM. Synthesis of the Pierce gun. IEEE Trans Electron Devices. 1981 Jan;28(1):37–41.

Baillie D, Aubin JS, Fallone BG, Steciw S. FEM design and simulation of a short, 10 MV, S-band Linac with Monte Carlo dose simulations. Med Phys. 2015 Apr 1;42(4):2044–53.

Pirzkall A, Carol MP, Pickett B, Xia P, Roach III M, Verhey LJ. The effect of beam energy and number of fields on photon-based IMRT for deep-seated targets. Int J Radiat Oncol. 2002 Jun 1;53(2):434–42.

St. Aubin J, Santos D, Steciw S, Fallone BG. Effect of longitudinal magnetic fields on a simulated in-line 6 MV linac. Med Phys. 2010;37:4916–23.